2015

Modeling and Computations of Cellular Dynamics Using Complex-fluid Models

Jia Zhao
University of South Carolina

Recommended Citation

Zhao, J.(2015). *Modeling and Computations of Cellular Dynamics Using Complex-fluid Models.* (Doctoral dissertation). Retrieved from https://scholarcommons.sc.edu/etd/3588

MODELING AND COMPUTATIONS OF CELLULAR DYNAMICS USING COMPLEX-FLUID MODELS

by

Jia Zhao

Bachelor of Sciences
Nankai University 2010

Submitted in Partial Fulfillment of the Requirements

For the Degree of Doctor of Philosophy in

Mathematics

College of Arts and Sciences

University of South Carolina

2015

Accepted by:

Qi Wang, Major Professor

Hong Wang, Committee Member

Lili Ju, Committee Member

Xiaofeng Yang, Committee Member

Qian Wang, Committee Member

Lacy Ford, Senior Vice Provost and Dean of Graduate Studies

DEDICATION

To my parents (Liandui Zhao and Jinchai Wang) and my loving wife Yuan Li.

Acknowledgments

I would like to gratefully and sincerely thank my advisor Dr. Qi Wang for his guidance through my graduate study, as well as life-long impact on my academic career.

I wish to thank my committee members: Dr. Hong Wang, Dr. Lili Ju, Dr. Xiaofeng Yang and Dr. Qian Wang, who have taken their valuable time to attend my dissertation defense, read my thesis and provide valuable comments.

Specially thank goes to Dr. Xiaogang Yang, who is my colleague and good friend. The inspiring discussions with him highly facilitate my research progress.

I would acknowledge all my friends in Columbia, South Carolina. The joy with you makes my life smoother in USA.

Last but not the least, I would offer sincere thanks to my loving wife Yuan Li, who has unshakable faith in me and takes care of my life, when I don't have time to do so.

Abstract

Cells are fundamental units in all living organisms as all living organisms are made up of cells of different varieties. The study of cells is therefore an essential part of research in life science. Cells can be classified into two basic types: prokaryotic cells and eukaryotic cells. One typical organisms of prokaryotes is bacterium. And eukaryotes mainly consist of animal cells. In this thesis, we focus on developing predictive models mathematically to study bacteria colonies and animal cell mitotic dynamics.

Instead of living alone, bacteria usually survive in a biofilm, which is a microorganism where bacteria stick together by extracellular matrix primarily made up of extracellular polymeric substances (EPS) that the bacteria excrete. By treating the biofilm and solvent as a fluid mixture, we have developed a mathematical modeling framework and computational tool to investigate the mechanisms of biofilm formation and function. The bacteria in biofilms can be categorized into various types either by their persistence to antimicrobial treatments or by their reactions to quorum sensing molecules. We have studied dynamics of 3D heterogeneous biofilm formation under hydrodynamic stress, investigated the pros and cons of quorum sensing mechanism in an aqueous environment subject to hydrodynamic impact, explored the mechanism of antimicrobial persistence, looked into optimal dosing strategies, and examined the impact of cell motility on the development of biofilm morphology. As an integral part of the study, we have also validated our model of biofilm persistence to antimicrobial treatment against the experimental results obtained in our collaborators' laboratory. Using the validated model, we then have probed the scenario of biofilm relapse after the antimicrobial treatment. These studies have demonstrated that our model and computational package can be an effective tool for analyzing the mechanism of biofilm formation and function.

During an eukaryotic cell cycle, mitosis is a process in which a mother cell divides into two genetically identical daughter cells. In the initial stage of mitosis, the mother cell, spreaded on a substrate, undergoes a dramatic shape change by detaching from the substance and forming a spherical shape. During the late stage of mitosis, a contractile ring forms on the cell division plane, splitting the mother cell into two identical daughter cells. This late stage of mitotic process is also known as cytokinesis for eukaryotic cells. We have developed a modeling framework for simulating the space-time evolution of cell morphology, cell motility and mitotic dynamics of eukaryotic cells by a multiphase field complex fluids approach. In order to solve the complex cellular dynamics models, we have developed a series of efficient, energy law preserving, stable schemes and implemented them on GPU clusters for high-performance computing. The models have shown qualitative agreement with experiments on cell rounding, movement, wrinkling, blebbing, and dividing processes.

TABLE OF CONTENTS

DEDICATION iii

ACKNOWLEDGMENTS iv

ABSTRACT v

LIST OF TABLES ix

LIST OF FIGURES x

CHAPTER 1 INTRODUCTION 1

1.1 Research background 1

1.2 A brief overview of the thesis 4

CHAPTER 2 A GENERAL FRAMEWORK FOR MODELING HYDRODYNAMIC SYSTEMS 5

2.1 A general hydrodynamic model for passive fluid mixture 5

2.2 Several special cases for the general hydrodynamic model 11

2.3 Hydrodynamic models for active fluid mixture 15

CHAPTER 3 ENERGY STABLE SEMI-DISCRETE SCHEMES FOR THE GENERAL HYDRODYNAMIC MODELS 17

3.1 An overview of existing works 17

3.2 A decoupled energy stable scheme for a hydrodynamic phase field model for cell membrane 18

3.3 A decoupled energy stable scheme for a hydrodynamic phase-field model of mixtures of nematic liquid crystals and viscous fluids 28

CHAPTER 4 MATHEMATICAL MODELING AND SIMULATIONS OF BIOFILMS DYNAMICS 43

4.1 Background of biofilms research 43

4.2 A 3D numerical study of antimicrobial persistence in heterogeneous multi-species biofilms 49

CHAPTER 5 MATHEMATICAL MODELING AND SIMULATIONS OF EUKARYOTIC CELL MORPHOLOGY AND MITOTIC DYNAMICS 77

5.1 Background on cell morphology and mitotic dynamics 77

5.2 Modeling the excess cell membrane stored in a complex morphology of bleb-like protrusions 82

5.3 A hydrodynamic model for cytokinesis of eukaryotic cells 89

CHAPTER 6 CONCLUSION 112

BIBLIOGRAPHY 114

LIST OF TABLES

Table 4.1 Values of dimentional parameters. 69

Table 5.1 Dimensional and dimensionless parameters. 89

Table 5.2 Dimensional parameters. 97

LIST OF FIGURES

Figure 1.1 Tools and Methodology of this research 3

Figure 4.1 Biofilm of Pseudomonas at different scales 44

Figure 4.2 Biofilm development. 45

Figure 4.3 A schematic portrait of effective components in the biofilm system studied 51

Figure 4.4 Model prediction and comparison with experiments. 70

Figure 4.5 Model prediction of biofilm recovery after antimicrobial treatment. 71

Figure 4.6 Reconstructing biofilm morphology through CLSM images. . . . 72

Figure 4.7 Biofilm recovery after 10-minute treatment with CHX-Plus. . . . 72

Figure 4.8 Heterogeneous growth in a biofilm. 73

Figure 4.9 Various stages of antimicrobial treatment of a three-week old biofilm. 74

Figure 4.10 Biofilm recovery after antimicrobial treatment. 75

Figure 4.11 Antimicrobial treatment of biofilms at different ages. 76

Figure 5.1 Mitotic cell rounding 78

Figure 5.2 A time line for a cell cycle. 78

Figure 5.3 Animal cell cytokinesis 80

Figure 5.4 Arrangment of F-actin in the contractile ring 81

Figure 5.5 Cell bleb-like protrusion 81

Figure 5.6 Schematic for the cell-buffer phase field formulation. 83

Figure 5.7 Simulation of cell wrinkling targeted at a 3D Cell provided by Alex. 90

Figure 5.8 Simulation of cell blebbing. 102

Figure 5.9 Arrangement of filaments in cortex for the steady state cell morphology. 103

Figure 5.10 Three invariants for stress tensor τ^e. 104

Figure 5.11 Three invariants for stress tensor τ^r. 105

Figure 5.12 A schematic cartoon for the phase-field cell model 106

Figure 5.13 Cell growth and cytokinesis 107

Figure 5.14 Hydrodynamic variables of cell cytokinesis at $t = 8.5$. 108

Figure 5.15 Visualization of the proxy force and the surface tension force . . . 109

Figure 5.16 Asymmetric cell division due to the asymmetric positioning of cleavage plane 110

Figure 5.17 Asymmetric cleavage furrow formation due to inhomogeneous actomyosin distribution 111

CHAPTER 1

INTRODUCTION

1.1 RESEARCH BACKGROUND

Cell Biology and Microbiology

A cell is the fundamental unit in all living organisms since animals and plants are all made up of cells in a wide range of varieties. Given its unique role played in living organisms, cell study has been the focus of biological research for centuries. With the advancement of experimental technologies today, such as the transmission electron microscopy(TEM), more cell functions and micro-structural details have been uncovered, revealing an amazingly complex, microscopic universe of a cell.

Cells can be categorized into two types: prokaryotes, which does not contain a membrane-bound nucleus and eukaryotes, which contain a nucleus that is bounded by a membrane. For most of the prokaryotes, they are single-celled organisms, while eukaryotes can be either of a single cell or of multicellular organisms. In this thesis, we specifically focus on bacteria (which is one type of prokaryotes), and animal cells (which is a main type of eukaryotic cells).

One of the main reason for conducting the research in this thesis goes to our long-term collaborations with cell biologist Dr. Kenneth Jacobson from Department of Cell Biology and Pharmacy, University of North Carolina at Chapel Hill, investigating cell plasma membrane-cortex coupling and morphological dynamics, and microbiologist Dr. Ya Shen from division of Endodonitics, Department of Dentistry, The University of British Columbia, studying dental biofilm formation and their treatment (biofilms are microorganisms, where bacteria are attached to either biotic or abiotic surfaces and embedded in self-secreted glue-like exopolysaccharides). This provides us access to valuable first-hand experiment data, and motivations for conducting researches shown in this thesis.

Many related works, experimentally and theoretically (both analytically and numerically) have been published in the literature. We will give a thorough review for previous and current relevant works on biofilms and mitotic cell dynamics in Chapter 3 and 4, respectively.

Complex fluid models

Complex fluids are fluids whose micro-structure can impact on the fluid macroscopic properties, which include complex fluid mixtures of different types. Usually they may appear to be homogeneous in the macroscopic scale, but contain inhomogeneity at a mesoscopic scale [33]. In this sense, the material properties of the complex fluid mixtures can be quite different when compared with each individual fluid component. Notice the fact that cells are usually immersed in a viscoelastic fluid matrix, where cell itself can also be treated as a viscoelastic fluid either in mesoscopic (where we study a single cell) or macroscopic scale (where we study cell aggregates). We, thus, formulate the models in a hydrodynamic setting, using complex fluid approaches.

There are plenty of works in the literature for modeling complex fluid mixtures. Mainly we can category them into two approaches: (i) treating the fluid mixture as a multiple-fluid mixture, i.e. the hydrodynamic quantities of each individual fluid are tracked [47]; (ii) regarding the fluid mixture as one fluid with multiple components [130, 131], i.e. volume-averaged hydrodynamic quantities are tracked, where the effective hydrodynamic quantities for an individual fluid component can be calculated through a pre-proposed formula. In this thesis, we stick to the second approach.

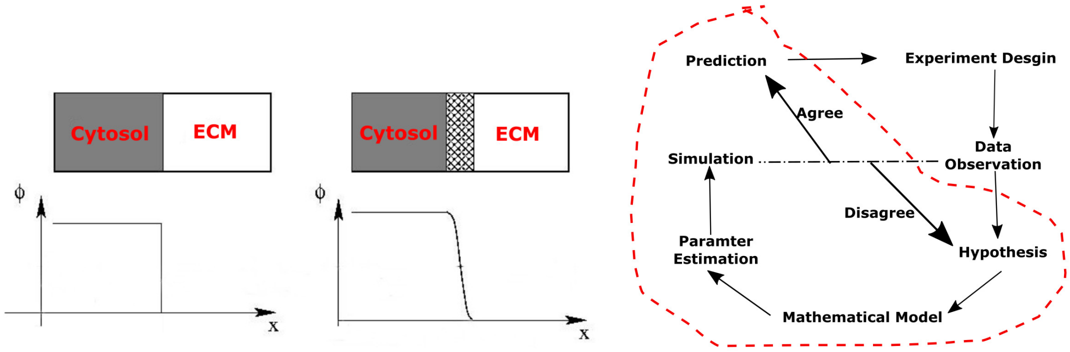

(a) idea of the phase field model (b) methodology

Figure 1.1: Tools and Methodology of this research on modeling cellular dynamics.

When modeling immiscible fluid mixtures, there exists an interface, which separates the different fluid components. Numerically this interface is difficult to resolve, as it normally requires extremely high resolution of the mesh size at the interface. There are a couple of broadly used strategies to tracking this interface, namely, the immersed boundary method [82], the sharp interface method[106], the front tracking method , the level set method [132] and the phase field method [109]. In this thesis, we use the phase field approach. The basic idea of phase field method lies in existence an artificial transition layer between the two immersible fluids, shown in Figure 1.1(A) (for instance, the interface between cytosol and extra cellular matrix). As a strength, we don't need to track the interface explicitly, instead, the method resolves the interface automatically.

To explain it succinctly, we show our methodology in conducting this research in Figure 1.1(B). Mainly, we want to explore the available experimental data using which to build predictive mathematical models to study the experimental system better.

1.2 A BRIEF OVERVIEW OF THE THESIS

The rest of this thesis is organized as below. In chapter 2, we propose a general framework for deriving governing equations for hydrodynamic systems of complex fluid mixture, following a generalized Onsager's principle. Then in chapter 3, we show linearly decoupled energy-stable semi-discrete schemes to solve several special cases of the general hydrodynamic model. In particular, the hydrodynamic vesicle model and the hydrodynamic nematic liquid crystal model are specifically discussed and the rigorous proof are provided. In Chapter 4, we propose a general framework for modeling biofilm formation and its treatment by antimicrobial agents, where quantitative agreements are obtained. In Chapter 5, we introduce a general multi-phase hydrodynamic modeling framework and numerical tool to study mitotic cell dynamics. Finally, in Chapter 6, we draw a conclusion for the work conducted in the thesis.

Chapter 2

A General Framework for Modeling Hydrodynamic Systems

In the well-known paper [79], Onsager extended Rayleigh's principle of the least energy dissipation to general irreversible processes. Doi gives a review of its applications in soft matter physics in [22],. Onsager's principle provides a general guideline on deriving phenomenological governing equations for dissipative thermodynamic systems, which has been widely used in modeling ion channel [120, 25], liquid crystal [125], biofilm [137], moving contact line [85] and so on. In this chapter, we develop a framework on deriving continnum hydrodynamic equations for thermodynamic systems, by generalizing Onsager's principle. And we will show many widely used models are actually specical cases (limits) of our general model.

2.1 A general hydrodynamic model for passive fluid mixture

In [41], the authors have shown an approach to derive the hydrodynamic equations, given the action functional and dissipation functional, based on least action principle and maximum dissipation principle. Here the action functional controls the reversible dynamics, and dissipation functional determines the irreversible dynamics, which contributes to the entropy product. However, in reality, these functionals are not known beforehand. Thus, this so-called variational approach is not so effective.

In this section, following the idea of Onsager [79, 80], we will present a general framework, where the hydrodynamic equations could be derived systematically by proposing relations between the general fluxes and general forces. This approach works for both single fluid and multiple fluid mixture with quite different rheology properties. In the following, we will mainly focus on deriving general models of a binary fluid mixture for simplicity, as the general hydrodynamic models for multiple fluid mixture could be derived in a similar manner.

Thermodynamic background

Following the notations in [120], for a closed thermodynamic system, we denote K as the kinetic energy, U as the internal energy, W as work done by the system, Q as heat generated by the system, Δ as energy dissipation, and E as total energy of the system. By the first law of thermodynamics, we have

$$\frac{d(K+U)}{dt} = \frac{dW}{dt} + \frac{dQ}{dt}. \tag{2.1.1}$$

By the second law of thermodynamics in isothermal case, we have

$$T\frac{dS}{dt} = \frac{dQ}{dt} + \Delta. \tag{2.1.2}$$

If we add (2.1.1) and (2.1.2), we obtain,

$$\frac{dE}{dt} = \frac{d(K+U-TS)}{dt} = \frac{dW}{dt} - \Delta. \tag{2.1.3}$$

In case of no external force, (2.1.3) is reduced into

$$\frac{dE}{dt} = -\Delta. \tag{2.1.4}$$

For passive system, we have $\Delta > 0$ at any time.

Derivation of the general hydrodynamic model

Given a fluid mixture with one viscoelastic fluid A (due to micro-structure in mesoscopic scale) immersed in a viscous fluid matrix B. Denote $\mathcal{S}^2$ the unit sphere,

$\mathbf{d} \in \mathcal{S}^2$, and $\mu_0(\mathbf{d})$ the volume fraction distribution functional of molecules with orientation $\mathbf{d}$ for fluid A. Then we obtain the following three quantities:

$$\phi = \int_{\mathcal{S}^2} d\mu_0(\mathbf{d}), \quad \mathbf{p} = \int_{\mathcal{S}^2} \mathbf{d} d\mu_0(\mathbf{d}), \quad \mathbf{Q} = \int_{\mathcal{S}^2} \Big(\mathbf{d} \otimes \mathbf{d} - \frac{1}{3}\mathbf{I}\Big) d\mu_0(\mathbf{d}). \tag{2.1.5}$$

Here ϕ is the volume fraction of fluid A, i.e.,

$$\phi = \begin{cases} 1, & \text{fluid A,} \\ (0,1), & \text{fluid mixture,} \\ 0, & \text{fluid B,} \end{cases} \tag{2.1.6}$$

$\mathbf{p}$ is the macroscopic polar (nematic) orientation of fluid A, and $\mathbf{Q}$ is a quantity representing the macroscopic apolar structure of fluid A.

With the thermodynamic system in domain Ω, the total energy E consists two components: (1)kinetic energy E_{kin}; (2) free energy F, i.e.

$$\begin{aligned} E &= E_{kin} + F \\ &= \textstyle\int_\Omega \frac{1}{2}\rho \mathbf{v}^2 d\mathbf{x} + \int_\Omega f(\phi, \nabla\phi, \mathbf{p}, \nabla\mathbf{p}, \mathbf{Q}, \nabla\mathbf{Q}) d\mathbf{x}, \end{aligned} \tag{2.1.7}$$

where $\mathbf{v}$ is the volume-averaged velocity, ρ is the volume-averaged density, f is the free energy density functional. In case of nonlocal interaction, we can propose

$$f = \int_\Omega K(\mathbf{x} - \mathbf{y}) g(\phi(\mathbf{y}, t), \mathbf{p}(\mathbf{y}, t), \mathbf{Q}(\mathbf{y}, t)) d\mathbf{y}, \tag{2.1.8}$$

with K a kernel function and g a functional. To make the framework general, in the following discussion, we don't restrict to any specific energy functional.

Given the free energy F, we can define the chemical potential μ and molecular fields $\mathbf{h}, \mathbf{H}$ as

$$\mu = \frac{\delta F}{\delta \phi}, \quad \mathbf{h} = -\frac{\delta F}{\delta \mathbf{p}}, \quad \mathbf{H} = -\frac{\delta F}{\delta \mathbf{Q}} + \frac{1}{3} tr(\frac{\delta F}{\delta \mathbf{Q}})\mathbf{I}. \tag{2.1.9}$$

Then phenomenologically we have the governing equations as

$$\left\{\begin{array}{rcl} \rho(\mathbf{v}_t + \mathbf{v}\cdot\nabla\mathbf{v}) &=& -\nabla p + \nabla\cdot\sigma + \mathbf{F}_e, \\ \nabla\cdot\mathbf{v} &=& 0, \\ \phi_t + \nabla\cdot(\mathbf{v}\phi) &=& M_1, \\ \mathbf{p}_t + \mathbf{v}\cdot\nabla\mathbf{p} - S_1(\nabla\mathbf{v},\mathbf{p}) &=& M_2, \\ \mathbf{Q}_t + \mathbf{v}\cdot\nabla\mathbf{Q} - S_2(\nabla\mathbf{v},\mathbf{Q}) &=& M_3, \end{array}\right. \tag{2.1.10}$$

with σ the viscoelastic stress, $\mathbf{F}_e$ is elastic force, $\mathbf{D}_{\alpha\beta} = \frac{1}{2}(\mathbf{v}_{\alpha,\beta} + \mathbf{v}_{\beta,\alpha})$ the rate of strain tensor , $\mathbf{W} = \frac{1}{2}(\mathbf{v}_{\alpha,\beta} - \mathbf{v}_{\beta,\alpha})$ the vorticity tensor, and

$$\begin{array}{rcl} S_1(\nabla\mathbf{v},\mathbf{p}) &=& \mathbf{W}\cdot\mathbf{p} + \nu\mathbf{D}\cdot\mathbf{p}, \\ S_2(\nabla\mathbf{v},\mathbf{Q}) &=& \mathbf{W}\cdot\mathbf{Q} - \mathbf{Q}\cdot\mathbf{W} \\ && +a(\mathbf{Q}\cdot\mathbf{D} + \mathbf{D}\cdot\mathbf{Q}) + \frac{2a}{3}\mathbf{D} - 2a(\mathbf{D}:\mathbf{Q})(\mathbf{Q} + \frac{1}{3}\mathbf{I}), \end{array} \tag{2.1.11}$$

with ν and a the tumbling parameters. We consider non-slip boundary condition for $\mathbf{v}$ and non-flux boundary condition for ϕ, $\mathbf{p}$, $\mathbf{Q}$, i.e.

$$\begin{array}{l} \mathbf{v} = 0, \quad \text{on} \quad \partial\Omega, \\ \frac{\partial F}{\partial\nabla\phi}\cdot\mathbf{n} = 0, \quad \frac{\partial F}{\partial\nabla\mathbf{p}}\cdot\mathbf{n} = 0, \quad \frac{\partial F}{\partial\nabla\mathbf{Q}}\cdot\mathbf{n} = 0, \quad \text{on} \quad \partial\Omega. \end{array} \tag{2.1.12}$$

Then the time rate change of the total energy could be calculated

$$\begin{array}{rcl} \frac{dE}{dt} &=& \int_\Omega \frac{1}{2}\rho_t\mathbf{v}^2 + \rho\mathbf{v}\mathbf{v}_t + \frac{\partial F}{\partial\phi}\frac{\partial\phi}{\partial t} + \frac{\partial F}{\partial\nabla\phi}(\nabla\phi)_t \\ && +\frac{\partial F}{\partial\mathbf{p}}\mathbf{p}_t + \frac{\partial F}{\partial\nabla\mathbf{p}}(\nabla\mathbf{p})_t + \frac{\partial F}{\partial\mathbf{Q}}\mathbf{Q}_t + \frac{\partial F}{\partial\nabla\mathbf{Q}}(\nabla\mathbf{Q})_t d\mathbf{x} \\ &=& \int_\Omega -\frac{1}{2}\rho_t\mathbf{v}^2 + \mathbf{v}(\rho\mathbf{v})_t + \frac{\delta F}{\delta\phi}\frac{\partial\phi}{\partial t} + \frac{\delta F}{\delta\mathbf{p}}\frac{\partial\mathbf{p}}{\partial t} + \frac{\delta F}{\delta\mathbf{Q}}\frac{\partial\mathbf{Q}}{\partial t}d\mathbf{x} \\ && + \int_{\partial\Omega}\frac{\partial F}{\partial\nabla\phi}\cdot\mathbf{n}\phi_t + \frac{\partial F}{\partial\nabla\mathbf{p}}\cdot\mathbf{n}\mathbf{p}_t + \frac{\partial F}{\partial\nabla\mathbf{Q}}\cdot\mathbf{n}\mathbf{Q}_t ds. \end{array} \tag{2.1.13}$$

Noticing the fact

$$\begin{array}{rl} & \int_\Omega -\frac{1}{2}\rho_t\mathbf{v}^2 + \mathbf{v}(\rho\mathbf{v})_t d\mathbf{x} \\ = & \int_\Omega \frac{1}{2}\nabla\cdot(\rho\mathbf{v})\mathbf{v}^2 - \mathbf{v}\nabla\cdot(\rho\mathbf{v}\mathbf{v}) + \mathbf{v}\cdot(\nabla\cdot\tau + \mathbf{F}_e)d\mathbf{x} \\ = & \int_\Omega \frac{1}{2}\nabla\cdot(\rho\mathbf{v})\mathbf{v}^2 - \nabla\cdot(\rho\mathbf{v})\mathbf{v}^2 - \rho\mathbf{v}\nabla(\frac{1}{2}\mathbf{v}^2) + \mathbf{v}\cdot(\nabla\cdot\tau + \mathbf{F}_e)d\mathbf{x} \\ = & \int_\Omega -\frac{1}{2}\nabla\cdot(\rho\mathbf{v}\frac{\mathbf{v}^2}{2}) + \mathbf{v}\cdot(\nabla\cdot\tau + \mathbf{F}_e)d\mathbf{x}, \end{array} \tag{2.1.14}$$

we have

$$
\begin{aligned}
&\tfrac{dE}{dt}\\
= \quad & \textstyle\int_\Omega -\nabla\mathbf{v}:\tau+\mathbf{v}\cdot\mathbf{F}_e+\frac{\delta F}{\delta\phi}\phi_t+\frac{\delta F}{\delta\mathbf{p}}\mathbf{p}_t+\frac{\delta F}{\delta\mathbf{Q}}\mathbf{Q}_t d\mathbf{x} \qquad (2.1.15)\\
& \textstyle+\int_{\partial\Omega}\mathbf{v}\cdot\tau\cdot\mathbf{n}-\frac{1}{2}\rho|\mathbf{v}|^2\mathbf{v}\cdot\mathbf{n}+\frac{\partial F}{\partial\nabla\phi}\cdot\mathbf{n}\phi_t+\frac{\partial F}{\partial\nabla\mathbf{p}}\cdot\mathbf{n}\mathbf{p}_t+\frac{\partial F}{\partial\nabla\mathbf{Q}}\cdot\mathbf{n}\mathbf{Q}_t ds.
\end{aligned}
$$

By substituting

$$
\begin{aligned}
\phi_t &= M_1-\nabla\cdot(\mathbf{v}\phi),\\
\mathbf{p}_t &= M_2-\mathbf{v}\cdot\nabla\mathbf{p}+S_1(\nabla\mathbf{v},\mathbf{p}), \qquad (2.1.16)\\
\mathbf{Q}_t &= M_3-\mathbf{v}\cdot\nabla\mathbf{Q}+S_2(\nabla\mathbf{v},\mathbf{Q}),
\end{aligned}
$$

due to (2.1.10), we further have

$$
\begin{aligned}
\tfrac{dE}{dt} &= \textstyle\int_\Omega -\nabla\mathbf{v}:\tau+\mathbf{v}\cdot\mathbf{F}_e+\frac{\delta F}{\delta\phi}(-\nabla\cdot(\mathbf{v}\phi)+M_1)\\
&\quad \textstyle+\frac{\delta F}{\delta\mathbf{p}}\Big(-\nabla\cdot(\mathbf{v}\mathbf{p})+S_1(\nabla\mathbf{v},\mathbf{p})+M_2\Big)\\
&\quad \textstyle+\frac{\delta F}{\delta\mathbf{Q}}\Big(-\nabla\cdot(\mathbf{v}\mathbf{Q})+S_2(\nabla\mathbf{v},\mathbf{Q})+M_3\Big)d\mathbf{x}\\
&= \textstyle\int_\Omega -\nabla\mathbf{v}:\tau+\mathbf{v}\cdot\mathbf{F}_e-\phi\frac{\delta F}{\delta\phi}\nabla\cdot\mathbf{v}-\frac{\delta F}{\delta\phi}\nabla\phi\cdot\mathbf{v} \qquad (2.1.17)\\
&\quad \textstyle-\frac{\delta F}{\delta\mathbf{p}}\cdot\mathbf{p}\nabla\cdot\mathbf{v}-\frac{\delta F}{\delta\mathbf{p}}\nabla\mathbf{p}\cdot\mathbf{v}-\frac{\delta F}{\delta\mathbf{Q}}\cdot\mathbf{Q}\nabla\cdot\mathbf{v}-\frac{\delta F}{\delta\mathbf{Q}}\nabla\mathbf{Q}\cdot\mathbf{v}\\
&\quad \textstyle+\frac{\delta F}{\delta\mathbf{p}}S_1(\nabla\mathbf{v},\mathbf{p})+\frac{\delta F}{\delta\mathbf{Q}}S_2(\nabla\mathbf{v},\mathbf{Q})+\frac{\delta F}{\delta\phi}M_1+\frac{\delta F}{\delta\mathbf{p}}M_2+\frac{\delta F}{\delta\mathbf{Q}}M_3 d\mathbf{x}\\
&= \textstyle\int_\Omega \mathbf{v}\cdot(\mathbf{F}_e-\frac{\delta F}{\delta\phi}-\frac{\delta F}{\delta\mathbf{p}}\nabla\mathbf{p}-\frac{\delta F}{\delta\mathbf{Q}}\nabla\mathbf{Q})+\frac{\delta F}{\delta\phi}M_1+\frac{\delta F}{\delta\mathbf{p}}M_2+\frac{\delta F}{\delta\mathbf{Q}}M_3\\
&\quad \textstyle+\nabla\mathbf{v}:(-\tau-\phi\frac{\delta F}{\delta\phi}\mathbf{I}-\mathbf{p}\cdot\frac{\delta F}{\delta\mathbf{p}}\mathbf{I}-\mathbf{Q}\cdot\frac{\delta F}{\delta\mathbf{Q}}\mathbf{I}+T_1(\mathbf{h},\mathbf{p}))+T_2(\mathbf{H},\mathbf{Q}))d\mathbf{x}.
\end{aligned}
$$

with

$$
\begin{aligned}
T_1(\mathbf{h},\mathbf{p}) &= \tfrac{1}{2}(\mathbf{p}\mathbf{h}-\mathbf{h}\mathbf{p})-\tfrac{\nu}{2}(\mathbf{p}\mathbf{h}+\mathbf{h}\mathbf{p})\\
T_2(\mathbf{H},\mathbf{Q}) &= (\mathbf{Q}\cdot\mathbf{H}-\mathbf{H}\cdot\mathbf{Q})-a(\mathbf{H}\cdot\mathbf{Q}+\mathbf{Q}\cdot\mathbf{H}) \qquad (2.1.18)\\
&\quad -\tfrac{2a}{3}\mathbf{H}+2a(\mathbf{Q}:\mathbf{H})(\mathbf{Q}+\tfrac{1}{3}\mathbf{I}).
\end{aligned}
$$

Here if we further assume

$$
\begin{aligned}
&\mathbf{F}_e-\tfrac{\delta F}{\delta\phi}\nabla\phi-\tfrac{\delta F}{\delta\mathbf{p}}\nabla\mathbf{p}-\tfrac{\delta F}{\delta\mathbf{Q}}\nabla\mathbf{Q}=0, \qquad (2.1.19)\\
&-\tau-\phi\tfrac{\delta F}{\delta\phi}\delta-\mathbf{p}\cdot\tfrac{\delta F}{\delta\mathbf{p}}\delta-\mathbf{Q}\cdot\tfrac{\delta F}{\delta\mathbf{Q}}\delta+T_1(\mathbf{h},\mathbf{p})+T_2(\mathbf{H},\mathbf{Q})=\tau_r,
\end{aligned}
$$

the energy dissipation rate could be expressed as

$$
\frac{dE}{dt}=-\int_\Omega(\nabla\mathbf{v},-\frac{\delta F}{\delta\phi},-\frac{\delta F}{\delta\mathbf{p}},-\frac{\delta F}{\delta\mathbf{Q}})\cdot(\tau_r,M_1,M_2,M_3)d\mathbf{x}. \qquad (2.1.20)
$$

Here (τ_r, M_1, M_2, M_3) are the general fluxes, and $(\nabla\mathbf{v}, -\frac{\delta F}{\delta\phi}, -\frac{\delta F}{\delta\mathbf{p}}, -\frac{\delta F}{\delta\mathbf{Q}})$ are the general conjugate forces. We can assume the fluxes are linear combinations of forces, i.e.

$$\begin{pmatrix} \tau_r \\ M_1 \\ M_2 \\ M_3 \end{pmatrix} = A_1 \begin{pmatrix} \nabla\mathbf{v} \\ -\frac{\delta F}{\delta\phi} \\ -\frac{\delta F}{\delta\mathbf{p}} \\ -\frac{\delta F}{\delta\mathbf{Q}} \end{pmatrix}, \tag{2.1.21}$$

where

$$A_1 = A_1(\phi, \nabla\phi, \mathbf{p}, \nabla\mathbf{p}, \mathbf{Q}, \nabla\mathbf{Q}). \tag{2.1.22}$$

Theorem 2.1.1 (Onsager's Principle)**.** *The general model* (2.1.10) *is energy dissipative, given that*

$$A_1 = A_1^+ + A_1^-, \tag{2.1.23}$$

with A_1^- anti-symmetric and A_1^+ is symmetric and positive definite.

Proof. This is trivial. Actually, from (2.1.20), if we denote

$$N = (\nabla\mathbf{v}, -\frac{\delta F}{\delta\phi}, -\frac{\delta F}{\delta\mathbf{p}}, -\frac{\delta F}{\delta\mathbf{Q}}), \tag{2.1.24}$$

we have

$$\begin{aligned} \frac{dE}{dt} &= -\int_\Omega N \cdot A_1 \cdot N^T d\mathbf{x} \\ &= -\int_\Omega N \cdot A_1^+ \cdot N^T d\mathbf{x} \\ &\leq 0, \end{aligned} \tag{2.1.25}$$

given A_1^+ is positive and definite. □

Remark 2.1.1. This is the so-called Onsager' principle [79]. Here A_1^+ controls the dissipative (irreversible) dynamics; A_1^- controls the reactive (reversible) dynamics.

There are many freedom on proposing A_1^+ and A_1^- as long as A_1^+ symmetric, positive definite and A_1^- anti-symmetric. Therefore, we can generate a class of models with proper choices of A_1^+ and A_1^-.

Given higher restrictions on the boundary conditions,

$$\begin{aligned}
&\mathbf{v} = 0, \quad \text{on} \quad \partial\Omega, \\
&\tfrac{\partial F}{\partial \nabla \phi} \cdot \mathbf{n} = 0, \quad \tfrac{\partial F}{\partial \nabla \mathbf{p}} \cdot \mathbf{n} = 0, \quad \tfrac{\partial F}{\partial \nabla \mathbf{Q}} \cdot \mathbf{n} = 0, \quad \text{on} \quad \partial\Omega, \\
&\nabla \tfrac{\delta F}{\delta \phi} \cdot \mathbf{n} = 0, \quad \nabla \tfrac{\delta F}{\delta \mathbf{p}} \cdot \mathbf{n} = 0, \quad \nabla \tfrac{\delta F}{\delta \mathbf{Q}} \cdot \mathbf{n} = 0, \quad \text{on} \quad \partial\Omega.
\end{aligned} \tag{2.1.26}$$

we can make (2.1.10) more general by proposing the general fluxes are linear combinations of general forces and their high-order derivatives, i.e.

$$\begin{pmatrix} \tau_r \\ M_1 \\ M_2 \\ M_3 \end{pmatrix} = A_1 \begin{pmatrix} \nabla \mathbf{v} \\ -\frac{\delta F}{\delta \phi} \\ -\frac{\delta F}{\delta \mathbf{p}} \\ -\frac{\delta F}{\delta \mathbf{Q}} \end{pmatrix} + A_2 \begin{pmatrix} -\Delta \nabla \mathbf{v} \\ \Delta \frac{\delta F}{\delta \phi} \\ \Delta \frac{\delta F}{\delta \mathbf{p}} \\ \Delta \frac{\delta F}{\delta \mathbf{Q}}, \end{pmatrix}, \tag{2.1.27}$$

with

$$A_1 = A_1(\phi, \nabla\phi, \mathbf{p}, \nabla\mathbf{p}, \mathbf{Q}, \nabla\mathbf{Q}), \quad A_2 = A_2(\phi, \nabla\phi, \mathbf{p}, \nabla\mathbf{p}, \mathbf{Q}, \nabla\mathbf{Q}). \tag{2.1.28}$$

Theorem 2.1.2. *The general model* (2.1.10) *is energy dissipative, given that*

$$A_1 = A_1^+ + A_1^-, \quad A_2 = A_2^+ + A_2^-, \tag{2.1.29}$$

with A_1^-, A_2^{-1} *anti-symmetric and* A_1^+, A_2^+ *are symmetric and positive definite.*

Proof. This proof is similar. □

2.2 SEVERAL SPECIAL CASES FOR THE GENERAL HYDRODYNAMIC MODEL

In this section, we will show some of the well-known models could be treated as special cases (limits) of the general model (2.1.10). Here, we mainly category three types: (i) viscous fluid mixture; (ii) fluid mixture with polar micro-structure; (iii) fluid mixture with apolar micro-structure.

Viscous fluid mixture

If fluid A is viscous, i.e.,

$$\mathbf{p} = \int_{\mathbb{S}^2} \mathbf{d} d\mu(\mathbf{d}) = 0, \quad \mathbf{Q} = \int_{\mathbb{S}^2} \Big(\mathbf{d} \otimes \mathbf{d} - \frac{1}{3}\mathbf{I}\Big) d\mu_0(\mathbf{d}) = 0, \tag{2.2.30}$$

the general model (2.1.10) is reduced into

$$\begin{cases} \rho\Big(\mathbf{v}_t + \mathbf{v}\cdot\nabla\mathbf{v}\Big) &= -\nabla p + \nabla\cdot\tau^r - \phi\nabla\mu, \\ \nabla\cdot\mathbf{v} &= 0, \\ \phi_t + \nabla\cdot(\mathbf{v}\phi) &= M_1, \end{cases} \tag{2.2.31}$$

with

$$\begin{pmatrix} \tau_r \\ M_1 \end{pmatrix} = A_1 \begin{pmatrix} \nabla\mathbf{v} \\ -\mu \end{pmatrix} + A_2 \begin{pmatrix} -\Delta\nabla\mathbf{v} \\ \Delta\mu \end{pmatrix}. \tag{2.2.32}$$

Here are several cases, by assuming different matrix elements for A_1 and A_2.

Example 2.2.1 (Allen-Cahn hydrodynamic model). *The model* (2.2.31) *is reduced into the Allen-Cahn hydrodynamic model*

$$\begin{cases} \rho\Big(\mathbf{v}_t + \mathbf{v}\cdot\nabla\mathbf{v}\Big) &= -\nabla p + \nabla\cdot(2\eta\mathbf{D}) - \phi\nabla\mu, \\ \nabla\cdot\mathbf{v} &= 0, \\ \phi_t + \nabla\cdot(\mathbf{v}\phi) &= -\lambda_1\mu, \end{cases} \tag{2.2.33}$$

if we assume

$$A_1 = \begin{pmatrix} \eta & 0 \\ 0 & \lambda_1 \end{pmatrix}, \quad A_2 = 0. \tag{2.2.34}$$

This model describes the evolution dynamics of an unconserved field. It has been widely used to study phase separation of iron alloys.

Example 2.2.2 (Cahn-Hilliard hydrodynamic model). *The model* (2.2.31) *is reduced into Cahn-Hilliard hydrodynamic model*

$$\begin{cases} \rho\Big(\mathbf{v}_t + \mathbf{v}\cdot\nabla\mathbf{v}\Big) &= -\nabla p + \nabla\cdot(2\eta\mathbf{D}) - \phi\nabla\mu, \\ \nabla\cdot\mathbf{v} &= 0, \\ \phi_t + \nabla\cdot(\mathbf{v}\phi) &= \lambda_1\nabla^2\mu, \end{cases} \tag{2.2.35}$$

if we propose

$$A_1 = \begin{pmatrix} \eta & 0 \\ 0 & 0 \end{pmatrix}, \quad A_2 = \begin{pmatrix} 0 & 0 \\ 0 & \lambda_1 \end{pmatrix}. \tag{2.2.36}$$

This model shows the evolution of a conserved quantity, which is initially brought out by [14, 13]. Given the Ginzburg-Landau free energy, this model have been broadly used to simulate phase separations [27]. Give the modified Flory Huggins free energy, this model have been used to study biofilm dynamics [130, 131]. Given the Herfrich bending energy, this model has been broadly used to study cell shapes [24, 115].

Fluid mixture with polar micro-structure

If fluid A is viscoelastic with polar micro-structure in mesoscopic scale, i.e.

$$\mathbf{p} = \int_{\mathbb{S}^2} \mathbf{d} d\mu_0(\mathbf{d}) \neq 0. \tag{2.2.37}$$

We can model this system with a simplified version of (2.1.10), i.e.

$$\left\{ \begin{array}{rcl} \rho\Big(\mathbf{v}_t + \mathbf{v}\cdot\nabla\mathbf{v}\Big) & = & -\nabla p + \nabla\cdot\tau^r + T_1(\mathbf{h},\mathbf{p}) - \phi\nabla\mu - \mathbf{h}\nabla\mathbf{p}, \\ \nabla\cdot\mathbf{v} & = & 0, \\ \phi_t + \nabla\cdot(\mathbf{v}\phi) & = & M_1, \\ \mathbf{p}_t + \mathbf{v}\cdot\nabla\mathbf{p} - S_1(\nabla\mathbf{v},\mathbf{p}) & = & M_2, \end{array} \right. \tag{2.2.38}$$

with

$$T_1(\mathbf{h},\mathbf{p}) = \frac{1}{2}(\mathbf{ph} - \mathbf{hp}) - \frac{\nu}{2}(\mathbf{ph} + \mathbf{hp}). \tag{2.2.39}$$

Example 2.2.3. *The model* (2.2.38) *is reduced into nematic hydrodynamic model*

$$\left\{ \begin{array}{rcl} \rho\Big(\mathbf{v}_t + \mathbf{v}\cdot\nabla\mathbf{v}\Big) & = & -\nabla p + \nabla\cdot(2\eta\mathbf{D}) + T_1(\mathbf{h},\mathbf{p}) - \phi\nabla\mu - \mathbf{h}\nabla\mathbf{p}, \\ \nabla\cdot\mathbf{v} & = & 0, \\ \phi_t + \nabla\cdot(\mathbf{v}\phi) & = & \lambda_1\nabla^2\mu, \\ \mathbf{p}_t + \mathbf{v}\cdot\nabla\mathbf{p} - S_1(\nabla\mathbf{v},\mathbf{p}) & = & \lambda_2\mathbf{h}, \end{array} \right. \tag{2.2.40}$$

given that

$$A_1 = \begin{pmatrix} \eta & 0 & 0 \\ 0 & 0 & 0 \\ 0 & 0 & \lambda_2 \end{pmatrix}, \quad A_2 = \begin{pmatrix} 0 & 0 & 0 \\ 0 & \lambda_1 & 0 \\ 0 & 0 & 0 \end{pmatrix}. \tag{2.2.41}$$

This model has been broadly used to study nematic liquid crystals [122, 124].

Fluid mixture with apolar micro-structure

If fluid A is viscoelastic, but with apolar micro-structure in mesoscopic scale, i.e.,

$$\mathbf{p} = \int_{\mathbb{S}^2} \mathbf{d} d\mu(\mathbf{d}) = 0, \quad \mathbf{Q} = \int_{\mathbb{S}^2} \Big(\mathbf{d} \otimes \mathbf{d} - \frac{1}{3}\mathbf{I}\Big) d\mu_0(\mathbf{d}) \neq 0, \tag{2.2.42}$$

the general model (2.1.10) is reduced into

$$\left\{ \begin{array}{rcl} \rho\Big(\mathbf{v}_t + \mathbf{v} \cdot \nabla \mathbf{v}\Big) & = & -\nabla p + \nabla \cdot \tau^r + T_2(\mathbf{H}, \mathbf{Q}) - \phi \nabla \mu - \mathbf{H} \nabla \mathbf{Q}, \\ \nabla \cdot \mathbf{v} & = & 0, \\ \phi_t + \nabla \cdot (\mathbf{v}\phi) & = & M_1, \\ \mathbf{Q}_t + \mathbf{v} \cdot \nabla \mathbf{Q} - S_2(\nabla \mathbf{v}, \mathbf{Q}) & = & M_3, \end{array} \right. \tag{2.2.43}$$

with

$$T_2(\mathbf{H}, \mathbf{Q}) = (\mathbf{Q} \cdot \mathbf{H} - \mathbf{H} \cdot \mathbf{Q}) - a(\mathbf{H} \cdot \mathbf{Q} + \mathbf{Q} \cdot \mathbf{H}) - \frac{2a}{3}\mathbf{H} + 2a(\mathbf{Q} : \mathbf{H})(\mathbf{Q} + \frac{1}{3}\mathbf{I}). \tag{2.2.44}$$

Example 2.2.4. *The model* (2.2.43) *is reduced into*

$$\left\{ \begin{array}{rcl} \rho\Big(\mathbf{v}_t + \mathbf{v} \cdot \nabla \mathbf{v}\Big) & = & -\nabla p + \nabla \cdot (2\eta \mathbf{D}) + T_2(\mathbf{H}, \mathbf{Q}) - \phi \nabla \mu - \mathbf{H} \nabla \mathbf{Q}, \\ \nabla \cdot \mathbf{v} & = & 0, \\ \phi_t + \nabla \cdot (\mathbf{v}\phi) & = & \lambda_1 \nabla^2 \mu, \\ \mathbf{Q}_t + \mathbf{v} \cdot \nabla \mathbf{Q} - S_2(\nabla \mathbf{v}, \mathbf{Q}) & = & \lambda_2 \mathbf{H}, \end{array} \right. \tag{2.2.45}$$

given that

$$A_1 = \begin{pmatrix} \eta & 0 & 0 \\ 0 & 0 & 0 \\ 0 & 0 & \lambda_3 \end{pmatrix}, \quad A_2 = \begin{pmatrix} 0 & 0 & 0 \\ 0 & \lambda_1 & 0 \\ 0 & 0 & 0 \end{pmatrix}. \tag{2.2.46}$$

This model has been recently used to study active liquid crystals by adding extra active stress [8].

Miscellaneous cases

This general model formulation also works for single-fluid case, i.e.

$$\phi = \int_{\mathbb{S}^2} d\mu_0(\mathbf{d}) = 1. \tag{2.2.47}$$

Example 2.2.5. *The general model* (2.1.10) *is reduced into*

$$\left\{\begin{array}{rcl} \rho\Big(\mathbf{v}_t + \mathbf{v}\cdot\nabla\mathbf{v}\Big) & = & -\nabla p + \nabla\cdot(2\eta\mathbf{D}) + T_1(\mathbf{h},\mathbf{p}) - \mathbf{h}\nabla\mathbf{p}, \\ \nabla\cdot\mathbf{v} & = & 0, \\ \mathbf{p}_t + \mathbf{v}\cdot\nabla\mathbf{p} - S_1(\nabla\mathbf{v},\mathbf{p}) & = & \lambda_2\mathbf{h}, \end{array}\right. \tag{2.2.48}$$

given that

$$A_1 = \begin{pmatrix} \eta & 0 & 0 & 0 \\ 0 & 0 & 0 & 0 \\ 0 & 0 & \lambda_2 & 0 \\ 0 & 0 & 0 & 0 \end{pmatrix}, \quad A_2 = 0. \tag{2.2.49}$$

This is the modified Ericksen-Leslie model and has been widely used to study nematic liquid crystals [63, 146, 145].

2.3 HYDRODYNAMIC MODELS FOR ACTIVE FLUID MIXTURE

In many biological systems, saying fish school, bacteria colonies, they consist of self-driven units, i.e. each unit or particle will consume chemical-biological energy that affecting the internal or external free energy. The system is not energy dissipative any more (we need to treat a bigger system in order to make it closed). However, we can formulate the governing equation in an effect-splitting approach, i.e. we first formulate the governing equation for the passive system. Then we plug in the extra active terms into the governing system, which reflects the activities generated by the self-driven kinetics. This approach turns out effective and have been widely used in the society of biophysics.

For instance,if we take into account of the activity, we can rewrite the model (2.2.40) into

$$\begin{cases} \rho(\partial_t \mathbf{v} + \mathbf{v}\cdot\nabla\mathbf{v}) = -\nabla p + \nabla\cdot(\sigma + \sigma_a), \\ \nabla\cdot\mathbf{v} = 0, \\ \partial_t\phi + \nabla\cdot((\mathbf{v}+\omega_1\mathbf{p})\phi) = M_1\nabla^2\mu, \\ \partial_t\mathbf{p} + (\mathbf{v}+\omega_2\mathbf{p})\cdot\nabla\mathbf{p} - S_1(\nabla\mathbf{v},\mathbf{p}) = M_2\mathbf{h}, \end{cases} \tag{2.3.50}$$

where σ_a represents the active stress, ω_1, ω_2 are self-propelled motion. One broadly used version for the active stress is [125, 126]

$$\sigma_a = \beta(\nabla\mathbf{p} + \nabla\mathbf{p}^T) + \zeta\mathbf{pp}, \tag{2.3.51}$$

with β the active viscosity and ζ the parameter for active motion. The active motion could be intuitively seen as a force dipole along the long-axis [37].

Chapter 3

Energy Stable Semi-discrete Schemes for the general hydrodynamic models

For the thermodynamically consistent models proposed in previous chapter, as they are too complicated for analysis, numerical solutions are desired. Notice the models obey the energy dissipation law, i.e. the total energy is dissipative in time. This provides a guideline, for developing numerical schemes, which satisfy the discrete energy law. In this chapter, we summarize our work on developing linearly decoupled semi-discrete energy stable numerical schemes for cracking several special cases of the general model proposed in previous chapter.

3.1 An overview of existing works

In terms of the several special cases we mentioned in previous chapter, the numerical schemes for Allen-Cahn hydrodynamic model (2.2.33) and the Cahn-Hilliard hydrodynamic model (2.2.35) have been widely studied. Shen and Yang are known for introducing the stabilizers [123, 95, 97]. Wise and Wang are known for proposing the convex splitting strategies [96, 118, 119]. In [74], the author has proposed a decoupled energy-stable numerical scheme for a ternary phase hydrodynamic model. The idea follows directly from operator-splitting, the velocity field is calculated by a two-step manner.

For the **p** vector-based liquid crystal (LC) hydrodynamic models (2.2.45), a few numerical schemes have been proposed. However, we would point out most are not proper, as they are dealing with a reduced version (which, too some extend, is not correct physically). For the **Q** tensor-based liquid crystal (LC) hydrodynamic models (2.2.40), there are few literatures available, as far as we are aware, though it has been broadly used in physically world for simulations.

During our research, we have proposed several energy-stable numerical schemes for some special cases of the general hydrodynamic models (2.1.10). Here we summarize two of them below.

3.2 A DECOUPLED ENERGY STABLE SCHEME FOR A HYDRODYNAMIC PHASE FIELD MODEL FOR CELL MEMBRANE

Mathematical model formulation

Here we use F to denote the thermodynamic free energy, which consists of three components:

$$F = F_s + F_b + F_{vol}, \tag{3.2.1}$$

where F_s is the inter-facial (surface tension) energy, given by the Ginzburg-Landau double-well potential,

$$F_s = \int_\Omega \gamma_1 \Big(\frac{1}{2} |\nabla \phi|^2 + f_s(\phi) \Big) d\mathbf{x}, \quad f_s(\phi) = \frac{1}{\varepsilon^2} \phi^2 (1-\phi)^2, \tag{3.2.2}$$

and F_b is the Helrfrich bending energy, with the form

$$F_b = \int_\Omega \frac{\gamma_2}{2} \Big(\nabla^2 \phi - f_b(\phi) \Big)^2 d\mathbf{x}, \quad f_b(\phi) = \frac{2}{\varepsilon^2} \phi(\phi - 1)(2\phi - 1). \tag{3.2.3}$$

Here F_{vol} is the constraint for total volume, proposed as

$$F_{vol} = \frac{\lambda_A}{2} (V(t) - V_0)^2, \quad V(t) = \int_\Omega \phi(\mathbf{x}, t) d\mathbf{x}, \quad V_0 = \int_\Omega \phi(\mathbf{x}, 0) d\mathbf{x}. \tag{3.2.4}$$

The detailed derivation of these free energy from a sharp-interface approach is omitted due to space limitation [133, 109]. Here we use μ to represent the chemical potential, which can be calculated by

$$\mu = \frac{\delta F}{\delta \phi} = \gamma_1(-\nabla^2\phi + f_s'(\phi)) + \gamma_2(\nabla^2 - f_b(\phi))(\nabla^2\phi - f_b'(\phi)) + \lambda_A(V(t) - V_0). \quad (3.2.5)$$

We further assume the two components in the fluid mixture have same density and viscosity, as the case with different density and viscosity could be dealt with similar manner. The non-dimensionalized Cahn-Hilliard vesicle model is proposed by

$$\left\{\begin{array}{rcl} \partial_t \mathbf{v} + \mathbf{v}\nabla\cdot\mathbf{v} & = & -\nabla p + \eta\nabla^2\mathbf{v} + \mu\nabla\phi, \\ \nabla\cdot\mathbf{v} & = & 0, \\ \partial_t\phi + \mathbf{v}\cdot\nabla\phi & = & M_1\nabla^2\mu, \end{array}\right. \quad (3.2.6)$$

with M_1 the motility parameter and η the volume-averaged viscosity.

Correspondingly, the non-dimensionalized Allen-Cahn vesicle model with volume conservation is proposed as

$$\left\{\begin{array}{rcl} \partial_t \mathbf{v} + \mathbf{v}\nabla\cdot\mathbf{v} & = & -\nabla p + \eta\nabla^2\mathbf{v} + \mu\nabla\phi, \\ \nabla\cdot\mathbf{v} & = & 0, \\ \partial_t\phi + \mathbf{v}\cdot\nabla\phi & = & -M_1\mu. \end{array}\right. \quad (3.2.7)$$

Numerical schemes

Here we have proposed two decoupled energy stable numerical schemes for the Alan-Cahn dynamics and Cahn-Hilliard dynamics. Here numerical schemes are summarized in this section. The proves are given in details in next section.

Numerical scheme for Allen-Cahn model

Given the initial condition ϕ^0, $\mathbf{u}^0$ and $p^0 = 0$, and having computed $(\phi^n, \mathbf{u}^n, p^n)$, we can calculate $(\phi^{n+1}, \mathbf{u}^{n+1}, p^{n+1})$ by the following two steps:

1. Step 1: Update ϕ^{n+1}:

$$\begin{cases} C_1(\phi^{n+1}-\phi^n)+\frac{1}{M_1}\dot{\phi}^{n+1}=-\mu^{n+1} \\ \mu^{n+1}=\gamma_1(-\nabla^2\phi^{n+1}+f_s'(\phi^n))+\gamma_2(\nabla^2-f_b'(\phi^n))(\nabla^2\phi^{n+1}-f_b(\phi^n)) \\ +\lambda_A(A^n-A_0), \\ \nabla\phi^{n+1}\cdot\mathbf{n}=0, \quad \nabla\nabla^2\phi^{n+1}\cdot\mathbf{n}=0. \end{cases} \tag{3.2.8}$$

with

$$\begin{array}{rcl} \dot{\phi}^{n+1} & = & \frac{\phi^{n+1}-\phi^n}{\delta t}+(\mathbf{u}_\star^n\cdot\nabla)\phi^n, \\ \mathbf{u}_\star^n & = & \mathbf{u}^n-\delta t\frac{\dot{\phi}^{n+1}}{M_1}\nabla\phi^n, \\ A^n & = & \int_\Omega\phi^n d\mathbf{x}. \end{array} \tag{3.2.9}$$

2. Step2: Update $(\mathbf{u}^{n+1},p^{n+1})$: calculate the following two equations sequentially

$$\begin{cases} \frac{\tilde{\mathbf{u}}^{n+1}-\mathbf{u}_\star^n}{\delta t}+(\mathbf{u}^n\cdot\nabla)\tilde{\mathbf{u}}^{n+1}=\nu\nabla^2\tilde{\mathbf{u}}^{n+1}-\nabla p^n, \\ \tilde{\mathbf{u}}^{n+1}|_{\partial\Omega}=0. \end{cases} \tag{3.2.10}$$

$$\begin{cases} \frac{\mathbf{u}^{n+1}-\tilde{\mathbf{u}}^{n+1}}{\delta t}=-\nabla(p^{n+1}-p^n), \\ \nabla\cdot\mathbf{u}^{n+1}=0, \\ \mathbf{u}^{n+1}\cdot\mathbf{n}|_{\partial\Omega}=0. \end{cases} \tag{3.2.11}$$

Numerical scheme for Cahn-Hilliad model

Given the initial condition ϕ^0, $\mathbf{u}^0$ and $p^0=0$, and having computed $(\phi^n,\mathbf{u}^n,p^n)$, we can calculate $(\phi^{n+1},\mathbf{u}^{n+1},p^{n+1})$ by the following two steps:

1. Update ϕ^{n+1}:

$$\begin{cases} \frac{1}{M_1}\dot{\phi}^{n+1}=\nabla^2\mu^{n+1}, \\ \mu^{n+1}=C_1(\phi^{n+1}-\phi^n)+C_2(\nabla^2\phi^{n+1}-\nabla^2\phi^n)+\gamma_1(-\nabla^2\phi^{n+1}+f_s'(\phi^n)) \\ +\nabla^2\nabla^2\phi^{n+1}-f_b'(\phi^n)\nabla^2\phi^n-\nabla^2 f_b(\phi^n)+f_b'(\phi^n)f_b(\phi^n), \\ \nabla\phi^{n+1}\cdot\mathbf{n}=0, \quad \nabla\nabla^2\phi^{n+1}\cdot\mathbf{n}=0, \quad \nabla\nabla^4\phi^{n+1}\cdot\mathbf{n}=0, \end{cases} \tag{3.2.12}$$

with

$$\dot{\phi}^{n+1} = \frac{\phi^{n+1}-\phi^{n}}{\delta t} + \nabla\cdot(\mathbf{u}_{\star}^{n}\phi^{n}), \quad \mathbf{u}_{\star}^{n} = \mathbf{u}^{n} - \delta t\phi^{n}\nabla\mu^{n+1}. \tag{3.2.13}$$

2. Update $(\mathbf{u}^{n+1}, p^{n+1})$:

$$\begin{cases} \frac{\tilde{\mathbf{u}}^{n+1}-\mathbf{u}^{n}}{\delta t} + (\mathbf{u}^{n}\cdot\nabla)\tilde{\mathbf{u}}^{n+1} = \nu\nabla^{2}\tilde{\mathbf{u}}^{n+1} - \nabla p^{n} - \phi^{n}\nabla\mu^{n+1}, \\ \tilde{\mathbf{u}}^{n+1}|_{\partial\Omega} = 0. \end{cases} \tag{3.2.14}$$

$$\begin{cases} \frac{\mathbf{u}^{n+1}-\tilde{\mathbf{u}}^{n+1}}{\delta t} = -\nabla(p^{n+1}-p^{n}), \\ \nabla\cdot\mathbf{u}^{n+1} = 0, \quad \mathbf{u}^{n+1}\cdot\mathbf{n}|_{\partial\Omega} = 0. \end{cases} \tag{3.2.15}$$

Semi-discrete energy dissipation law

Before showing our theorems, we provide a lemma here, which is essential for the proof later. Besides, the conditions in the lemma could be optimized if we use nonlinear schemes saying convex splittings.

In this context, we use $(\cdot,\cdot)$ to represent the inner-product in domain Ω. Define the discretized free energy F^n as

$$F^{n} = \gamma_{1}\Big(\frac{1}{2}|\nabla\phi^{n}|^{2} + f_{s}(\phi^{n}), 1\Big) + \frac{\gamma_{2}}{2}\Big(|\nabla^{2}\phi^{n} - f_{b}(\phi^{n})|^{2}, 1\Big) + \frac{1}{2}\lambda_{A}(A^{n}-A_{0})^{2}. \tag{3.2.16}$$

In this whole draft, we assume the following inequalities are always true,

$$\max_{x\in\mathbb{R}}|f_{s}''(x)| < L_{3}, \quad \max_{x\in\mathbb{R}}|(f_{b}(x)^{2})''| < L_{1}, \quad \max_{x\in\mathbb{R}}|f_{b}'(x)| < L_{4}, \quad \max_{x\in\mathbb{R}}|f_{b}''(x)| < L_{2}. \tag{3.2.17}$$

One may argue this condition is not satisfied. However, notice the truth $f_b(\phi) = f_s'(\phi)$. The assumption (3.2.17) on the existence of L_1, L_2, L_3, L_4 above is equivalent with

$$\max_{x\in\mathbb{R}}|f_{s}^{(i)}(x)| < L < \infty, \quad \forall i = 1, 2, 3. \tag{3.2.18}$$

We can truncate $f_s(\phi)$ to quadratic growth outside of an interval $[0, 1]$ without affecting the solutions, if the maximum norm of the initial condition ϕ_0 is bounded by

1. For instance, we can truncate $f_s(\phi)$ as

$$\tilde{f}_s(\phi) = \begin{cases} \frac{1}{\varepsilon^2}(\phi-1)^2, & \phi > 1, \\ \frac{1}{\varepsilon^2}\phi^2(1-\phi)^2, & \phi \in [0,1] \\ \frac{1}{\varepsilon^2}\phi^2, & \phi < 0. \end{cases} \tag{3.2.19}$$

One can notice, (3.2.17) or (3.2.18) could be satisfied by $\tilde{f}_s(\phi)$.

Lemma 3.2.1. *Define the discrete chemical potential as*

$$\begin{aligned} \mu^{n+1} &= \gamma_1\Big(-\nabla^2\phi^{n+1} + f_s'(\phi^n)\Big) - \gamma_2(\nabla^2 - f_b'(\phi^n))(\nabla^2\phi^{n+1} - f_b(\phi^n)) \\ &\quad +\lambda_A(A^n - A_0). \end{aligned} \tag{3.2.20}$$

the inequality holds

$$C_1\|\phi^{n+1}-\phi^n\|^2 + (\phi^{n+1}-\phi^n, \mu^{n+1}) > F^{n+1} - F^n, \tag{3.2.21}$$

given

$$C_1 > \gamma_1 L_3 + \gamma_2\Big(L_1 + +8L_4^2 + L_2 \max\|\nabla^2\phi^n\|\Big) + \frac{1}{2}\lambda_A|\Omega|, \tag{3.2.22}$$

with F^{n+1} *and* F^n *defined in* (3.2.16), *and* L_i, $i = 1,2,3,4$ *defined in* (3.2.17).

Proof. Taking the inner product of μ^{n+1} with $\phi^{n+1}-\phi^n$, we have

$$\begin{aligned} (\phi^{n+1}-\phi^n, \mu^{n+1}) &= \Big(\phi^{n+1}-\phi^n, \gamma_1(-\nabla\phi^{n+1} + f_s'(\phi^n))\Big) \\ &\quad +\Big(\phi^{n+1}-\phi^n, \gamma_2(\nabla^2 - f_b'(\phi^n))(\nabla^2\phi^{n+1} - f_b(\phi^n))\Big) \\ &\quad +\Big(\phi^{n+1}-\phi^n, \lambda_A(A^n - A_0)\Big). \end{aligned} \tag{3.2.23}$$

Here we denote

$$\begin{aligned} S &= (\phi^{n+1}-\phi^n, \mu^{n+1}), \\ S_1 &= \Big(\phi^{n+1}-\phi^n, \gamma_1(-\nabla^2\phi^{n+1} + f_s'(\phi^n))\Big), \\ S_2 &= \Big(\phi^{n+1}-\phi^n, \gamma_2(\nabla^2 - f_b'(\phi^n))(\nabla^2\phi^{n+1} - f_b(\phi^n))\Big), \\ S_3 &= \Big(\phi^{n+1}-\phi^n, \lambda_A(A^n - A_0)\Big). \end{aligned} \tag{3.2.24}$$

For the first term S_1, it holds,

$$\begin{aligned}&\tfrac{1}{\gamma_1}S_1 \geq \tfrac{1}{2}\left(\|\nabla\phi^{n+1}\|^2 - \|\nabla\phi^n\|^2 + \|\nabla\phi^{n+1} - \nabla\phi^n\|^2\right)\\ &+(f(\phi^{n+1}) - f(\phi^n), 1) - L_3\|\phi^{n+1} - \phi^n\|^2.\end{aligned} \tag{3.2.25}$$

For the second term S_2, we have the following identify

$$\begin{aligned}\tfrac{1}{\gamma_2}S_2 &= \left(\left(\nabla^2 - f_b'(\phi^n)\right)(\phi^{n+1} - \phi^n), \nabla^2\phi^{n+1} - f_b(\phi^n)\right)\\ &= (\nabla^2(\phi^{n+1} - \phi^n), \nabla^2\phi^{n+1}) - (f_b'(\phi^n)(\phi^{n+1} - \phi^n), \nabla^2\phi^{n+1})\\ &\quad -\left(\nabla^2(\phi^{n+1} - \phi^n), f_b(\phi^n)\right) + (f_b'(\phi^n)f_b(\phi^n), \phi^{n+1} - \phi^n).\end{aligned} \tag{3.2.26}$$

To better demonstrate the idea, let's set up several notations,

$$\begin{aligned}T_1 &= (\nabla^2(\phi^{n+1} - \phi^n), \nabla^2\phi^{n+1}),\\ T_2 &= -(f_b'(\phi^n)(\phi^{n+1} - \phi^n), \nabla^2\phi^{n+1}) + \left(\nabla^2(\phi^{n+1} - \phi^n), f_b(\phi^n)\right),\\ T_3 &= (f_b'(\phi^n)f_b(\phi^n), \phi^{n+1} - \phi^n).\end{aligned} \tag{3.2.27}$$

$$T_1 = \frac{1}{2}\left(\|\nabla^2\phi^{n+1}\|^2 - \|\nabla^2\phi^n\|^2 + \|\nabla^2\phi^{n+1} - \nabla^2\phi^n\|^2\right). \tag{3.2.28}$$

$$\begin{aligned}T_2 &= (\nabla^2\phi^{n+1}, f_b(\phi^n) + f_b'(\phi^n)(\phi^{n+1} - \phi^n)) + (\nabla^2\phi^n, f_b(\phi^n))\\ &= -\left(f_b(\phi^{n+1})\nabla^2\phi^{n+1} - f_b(\phi^n)\nabla^2\phi^n, 1\right)\\ &\quad -(\nabla^2\phi^{n+1}, f_b(\phi^{n+1}) - f_b(\phi^n) - f_b'(\phi^n)(\phi^{n+1} - \phi^n)),\end{aligned} \tag{3.2.29}$$

where the last term could be better approximated as

$$\begin{aligned}&-\left(\nabla^2\phi^{n+1}, f_b(\phi^{n+1}) - f_b(\phi^n) - f_b'(\phi^n)(\phi^{n+1} - \phi^n)\right)\\ =\ &-\left(\nabla^2\phi^{n+1} - \nabla^2\phi^n + \nabla^2\phi^n, f_b(\phi^{n+1}) - f_b(\phi^n) - f_b'(\phi^n)(\phi^{n+1} - \phi^n)\right)\\ =\ &-\left(\nabla^2\phi^{n+1} - \nabla^2\phi^n, (f_b'(\xi) - f_b'(\phi^n))(\phi^{n+1} - \phi^n)\right)\\ &-(\nabla^2\phi^n, f_b''(\xi)(\phi^{n+1} - \phi^n)^2)\\ \geq\ &-2L_4\left(|\nabla^2\phi^{n+1} - \nabla^2\phi^n|, |\phi^{n+1} - \phi^n|\right) - L_2\left(|\nabla^2\phi^n|, |\phi^{n+1} - \phi^n|^2\right)\\ \geq\ &-\Bigg(\tfrac{\varepsilon_0}{2}\|\nabla^2\phi^{n+1} - \nabla^2\phi^n\|^2 + \tfrac{8L_4^2}{\varepsilon_0}\|\phi^{n+1} - \phi^n\|^2\\ &+L_2\max|\nabla^2\phi^n|\|\phi^{n+1} - \phi^n\|^2\Bigg),\end{aligned} \tag{3.2.30}$$

where ε_0 is any positive constant. Here we choose $\varepsilon_0 = 1$.

$$\begin{aligned} T_3 &= \tfrac{1}{2}(f_b^2(\phi^{n+1}) - f_b^2(\phi^n), 1) - ((f_b^2(\xi))''(\phi^{n+1} - \phi^n)^2, 1) \\ &\geq \tfrac{1}{2}(f_b^2(\phi^{n+1}) - f_b^2(\phi^n), 1) - L_1\|\phi^{n+1} - \phi^n\|^2. \end{aligned} \tag{3.2.31}$$

For the third term S_3, it holds

$$\begin{aligned} \tfrac{1}{\lambda_A} S_3 &= (\phi^{n+1} - \phi^n, A^n - A_0) \\ &= (A^{n+1} - A^n)(A^n - A_0) \\ &= \Big((A^{n+1} - A_0) - (A^n - A_0)\Big)(A^n - A_0) \\ &= \tfrac{1}{2}\Big((A^{n+1} - A_0)^2 - (A^n - A_0)^2 - (A^{n+1} - A^n)^2\Big) \\ &\geq \tfrac{1}{2}\Big((A^{n+1} - A_0)^2 - (A^n - A_0)^2\Big) - \tfrac{1}{2}|\Omega|\|\phi^{n+1} - \phi^n\|^2, \end{aligned} \tag{3.2.32}$$

by noticing the fact

$$-(A^{n+1} - A^n)^2 = -\Big(\int_\Omega \phi^{n+1} - \phi^n d\mathbf{x}\Big)^2 \geq -|\Omega|\|\phi^{n+1} - \phi^n\|^2.$$

Combing all the three terms for S_1, S_2 and S_3, we have,

$$\begin{aligned} S \;\geq\; & F^{n+1} - F^n - \gamma_1 L_3\|\phi^{n+1} - \phi^n\|^2 - \tfrac{\lambda_A|\Omega|}{2}\|\phi^{n+1} - \phi^n\|^2 - \gamma_2 L_1\|\phi^{n+1} - \phi^n\|^2 \\ & -8\gamma_2 L_4^2\|\phi^{n+1} - \phi^n\|^2 - \gamma_2 L_2 \max|\nabla^2\phi^n|\|\phi^{n+1} - \phi^n\|^2. \end{aligned} \tag{3.2.33}$$

Under the assumption

$$C_1 > \gamma_1 L_3 + \gamma_2\Big(L_1 + +8L_4^2 + L_2 \max\|\nabla^2\phi^n\|\Big) + \frac{1}{2}\lambda_A|\Omega|. \tag{3.2.34}$$

We have directly

$$C_1\|\phi^{n+1} - \phi^n\|^2 + (\phi^{n+1} - \phi^n, \mu^{n+1}) > F^{n+1} - F^n, \tag{3.2.35}$$

□

Lemma 3.2.2. *Define the discrete chemical potential as*

$$\begin{aligned} \mu^{n+1} \;=\; & \gamma_1\Big(-\nabla^2\phi^{n+1} + f_s'(\phi^n)\Big) - \gamma_2(\nabla^2 - f_b'(\phi^n))(\nabla^2\phi^{n+1} - f_b(\phi^n)) \\ & +\lambda_A(A^n - A_0). \end{aligned} \tag{3.2.36}$$

Under the assumption (3.2.17), it holds

$$C_1\|\phi^{n+1}-\phi^n\|^2+C_2\|\nabla\phi^{n+1}-\nabla\phi^n\|^2+(\phi^{n+1}-\phi^n,\mu^{n+1})>F^{n+1}-F^n, \tag{3.2.37}$$

as long as

$$\begin{aligned} C_1 &> \gamma_1 L_3+\gamma_2\Big(L_1++\tfrac{8L_4^2}{\varepsilon_0}+L_2\max\|\nabla^2\phi^n\|\Big)+\tfrac{1}{2}\lambda_A|\Omega|,\\ C_2 &> \tfrac{1}{2}\varepsilon_0-\tfrac{1}{2}\gamma_2, \end{aligned} \tag{3.2.38}$$

with ε_0 any positive constant.

Proof. This proof is similar with Lemma 3.2.1. The only different part is that we use the Cauchy inequality with different parameter for (3.2.30), i.e.

$$\begin{aligned} &-2L_4\Big(|\nabla^2\phi^{n+1}-\nabla^2\phi^n|,|\phi^{n+1}-\phi^n|\Big)-L_2\Big(|\nabla^2\phi^n|,|\phi^{n+1}-\phi^n|^2\Big)\\ &\geq-\Big(\tfrac{\varepsilon_0}{2}\|\nabla^2\phi^{n+1}-\nabla^2\phi^n\|^2+8\tfrac{L_4^2}{\varepsilon_0}\|\phi^{n+1}-\phi^n\|^2\\ &+L_2\max|\nabla^2\phi^n|\|\phi^{n+1}-\phi^n\|^2\Big). \end{aligned} \tag{3.2.39}$$

□

Lemma 3.2.3. *Define the discrete chemical potential as*

$$\begin{aligned} \mu^{n+1} &= \gamma_1\Big(-\nabla^2\phi^{n+1}+f_s'(\phi^n)\Big)\\ &\quad-\gamma_2(\nabla^2-f_b'(\phi^n))(\nabla^2\phi^{n+1}-f_b(\phi^n))+\lambda_A(A^n-A_0). \end{aligned} \tag{3.2.40}$$

If we propose

$$f_b'(\phi^n)=\begin{cases} \frac{f_b(\phi^{n+1})-f_b(\phi^n)}{\phi^{n+1}-\phi^n}, & \text{if} \quad \phi^{n+1}\neq\phi^n,\\ f_b'(\phi^n), & \text{if} \quad \phi^{n+1}=\phi^n. \end{cases} \tag{3.2.41}$$

Under the assumption (3.2.17), it holds

$$C_1\|\phi^{n+1}-\phi^n\|^2+(\phi^{n+1}-\phi^n,\mu^{n+1})>F^{n+1}-F^n, \tag{3.2.42}$$

as long as

$$C_1>\gamma_1L_3+\gamma_2L_1++\frac{1}{2}\lambda_A|\Omega|. \tag{3.2.43}$$

Proof. Notice the fact, if we assume $f_b'(\phi^n)$ as (3.2.41), it holds directly

$$-\Big(\nabla^2\phi^{n+1}, f_b(\phi^{n+1}) - f_b(\phi^n) - f_b'(\phi^n)(\phi^{n+1}-\phi^n)\Big) = 0. \tag{3.2.44}$$

The extra constraints induced by this term could be reduced. □

Theorem 3.2.1. *Under the condition of either Lemma 3.2.1, Lemma 3.2.2 or Lemma 3.2.3, the scheme (3.2.8)-(3.2.10) admits a unique solution satisfying the following discrete energy dissipation law:*

$$\begin{gathered}\tfrac{1}{2}\|\mathbf{u}^{n+1}\|^2 + F^{n+1} + \tfrac{\delta t^2}{2}\|\nabla p^{n+1}\|^2 + \tfrac{1}{2}\|\tilde{\mathbf{u}}^{n+1} - \mathbf{u}^n\|^2 + 2\nu\delta t\|\nabla\tilde{\mathbf{u}}^{n+1}\|^2 \\ + \tfrac{\delta t}{M_1}\|\dot{\phi}^{n+1}\|^2 \leq \tfrac{1}{2}\|\mathbf{u}\|^n + F^n + \tfrac{\delta t^2}{2}\|\nabla p^n\|^2.\end{gathered} \tag{3.2.45}$$

Proof. The proof is similar with previous results when we only consider the surface tension energy, but with some tricky techniques. If we take inner product of (3.2.8) with $(\phi^{n+1}-\phi^n)$, we'll have

$$C_1\|\phi^{n+1}-\phi^n\|^2 + \frac{\delta t}{M_1}\|\dot{\phi}^{n+1}\|^2 - \delta t(\frac{\dot{\phi}^{n+1}}{M_1}, \mathbf{u}_\star^n\cdot\nabla\phi^n) + (\phi^{n+1}-\phi^n, \mu^{n+1}) = 0. \tag{3.2.46}$$

By either Lemma 3.2.1, Lemma 3.2.2 or Lemma 3.2.3, i.e.

$$C_1\|\phi^{n+1}-\phi^n\|^2 + (\phi^{n+1}-\phi^n, \mu^{n+1}) \geq F^{n+1} - F^n, \tag{3.2.47}$$

it holds,

$$F^{n+1} - F^n + \frac{\delta t}{M_1}\|\dot{\phi}^{n+1}\|^2 - \delta t(\frac{\dot{\phi}^{n+1}}{M_1}, \mathbf{u}_\star^n\cdot\nabla\phi^n) < 0. \tag{3.2.48}$$

If we take inner product of (3.2.9) with $\mathbf{u}_\star^n$, we have

$$\frac{1}{2}\Big(\|\mathbf{u}_\star^n\|^2 - \|\mathbf{u}^n\|^2 + \|\mathbf{u}_\star^n - \mathbf{u}^n\|^2\Big) + \delta t(\mathbf{u}_\star^n, \frac{\dot{\phi}^{n+1}}{M_1}\nabla\phi^n) = 0. \tag{3.2.49}$$

If we take inner prodcut of (3.2.10) with $\delta t\tilde{\mathbf{u}}^{n+1}$, we have

$$\frac{1}{2}\Big(\|\tilde{\mathbf{u}}^{n+1}\|^2 - \|\mathbf{u}_\star^n\|^2 + \|\tilde{\mathbf{u}}^{n+1} - \mathbf{u}^n\|^2\Big) + \delta t\nu\|\nabla\tilde{\mathbf{u}}^{n+1}\|^2 + (\tilde{\mathbf{u}}^{n+1}, \nabla p) = 0. \tag{3.2.50}$$

If we take inner product of (3.2.11) with $\delta t\mathbf{u}^{n+1}$, we have

$$\frac{1}{2}\Big(\|\mathbf{u}^{n+1}\|^2 - \|\tilde{\mathbf{u}}^{n+1}\|^2 + \|\mathbf{u}^{n+1} - \tilde{\mathbf{u}}^{n+1}\|^2\Big) = 0. \tag{3.2.51}$$

If we take inner product of (3.2.11) with $\delta t^2 p^n$, we have,

$$\delta t^2\Big(\|\nabla p^{n+1}\|^2 - \|\nabla p^n\|^2 - \|\nabla p^{n+1} - \nabla p^n\|^2\Big) - 2\delta t(\tilde{\mathbf{u}}^{n+1}, \nabla p^n) = 0. \tag{3.2.52}$$

And notice

$$\begin{aligned} \|\mathbf{u}^{n+1}\|^2 + \|\mathbf{u}^{n+1} - \tilde{\mathbf{u}}^{n+1}\|^2 &= \|\tilde{\mathbf{u}}^{n+1}\|^2, \\ \delta t^2\|\nabla p^{n+1} - \nabla p^n\|^2 &= \|\mathbf{u}^{n+1} - \tilde{\mathbf{u}}^{n+1}\|^2. \end{aligned} \tag{3.2.53}$$

Combing all the terms, we have

$$\begin{gathered} \tfrac{1}{2}\Big(\|\mathbf{u}^{n+1}\|^2 - \|\mathbf{u}_\star^n\|^2 + \|\tilde{\mathbf{u}}^{n+1} - \mathbf{u}_\star^n\|^2\Big) + \delta t^2\Big(\|\nabla p^{n+1}\| - \|\nabla p^n\|^2\Big) \\ +2\nu\delta t\|\nabla\tilde{\mathbf{u}}^{n+1}\|^2 = 0. \end{gathered} \tag{3.2.54}$$

Combing (3.2.48),(3.2.49),(3.2.54), we get the result,

$$\begin{gathered} \tfrac{1}{2}\|\mathbf{u}^{n+1}\|^2 + F^{n+1} + \tfrac{\delta t^2}{2}\|\nabla p^{n+1}\|^2 + \tfrac{1}{2}\|\tilde{\mathbf{u}}^{n+1} - \mathbf{u}^n\|^2 + 2\nu\delta t\|\nabla\tilde{\mathbf{u}}^{n+1}\|^2 \\ +\tfrac{\delta t}{M_1}\|\dot{\phi}^{n+1}\|^2 \le \tfrac{1}{2}\|\mathbf{u}\|^n + F^n + \tfrac{\delta t^2}{2}\|\nabla p^n\|^2. \end{gathered} \tag{3.2.55}$$

□

Theorem 3.2.2. *Under the condition of either Lemma 3.2.1, Lemma 3.2.2 or Lemma 3.2.3, the scheme (3.2.12)-(3.2.14) admits a unique solution satisfying the following discrete energy dissipation law:*

$$\begin{gathered} \tfrac{1}{2}\|\mathbf{u}^{n+1}\|^2 + F^{n+1} + \tfrac{\delta t^2}{2}\|\nabla p^{n+1}\|^2 + \tfrac{1}{2}\|\tilde{\mathbf{u}}^{n+1} - \mathbf{u}^n\|^2 + 2\nu\delta t\|\nabla\tilde{\mathbf{u}}^{n+1}\|^2 \\ +\tfrac{\delta t}{M_1}\|\nabla\mu^{n+1}\|^2 \le \tfrac{1}{2}\|\mathbf{u}\|^n + F^n + \tfrac{\delta t^2}{2}\|\nabla p^n\|^2, \end{gathered} \tag{3.2.56}$$

Proof. This proof is similar with the Allen-Cahn case. We thus leave it to interested readers. □

3.3 A DECOUPLED ENERGY STABLE SCHEME FOR A HYDRODYNAMIC PHASE-FIELD MODEL OF MIXTURES OF NEMATIC LIQUID CRYSTALS AND VISCOUS FLUIDS

Two-phase hydrodynamic model for mixtures of nematic liquid crystals and viscous fluids

We consider a two-phase hydrodynamic phase field model for immiscible mixtures of nematic liquid crystals (LC) immersed in a viscous fluid matrix. We use a phase function ϕ to represent the volume fraction of the liquid crystal phase,

$$\phi(x,t) = \begin{cases} 1 & \text{liquid crystal,} \\ 0 & \text{viscous fluid,} \end{cases} \tag{3.3.57}$$

with a thin smooth transitional layer of thickness ε separating the liquid crystal from the viscous fluid. The interface of the mixture is described by the level set $\Gamma_t = \{x : \phi(x,t) = \frac{1}{2}\}$. We use ρ and η to denote the volume-averaged density and viscosity. Without loss of generality, we assume all model parameters are already non-dimensionalized and therefore dimensionless.

The total energy of the mixture fluid system is given by the sum of the kinetic energy E_{kin}, the mixing free energy E_b, the bulk free energy for liquid crystals $E_{\mathbf{p}}$, and the anchoring energy for liquid crystals E_{anch} [128]:

$$E = E_b + E_{\mathbf{d}} + E_{anch} + E_{kin}. \tag{3.3.58}$$

Specifically, we denote $f(\phi) = \frac{1}{\varepsilon^2}\phi^2(1-\phi)^2$ as the Ginzburg-Landau double-well potential and define the mixing free energy functional by

$$E_b = \int_\Omega \gamma(\frac{1}{2}|\nabla\phi|^2 + f(\phi))d\mathbf{x}, \tag{3.3.59}$$

where γ is the strength of the energy related to the traditional surface tension [128].

We assume that the bulk energy for liquid crystals is given by the modified Oseen-Frank distortional energy with a penalizing bulk term for handling potential defects [26, 55, 56]:

$$E_{\mathbf{d}} = \int_\Omega \frac{1}{2}\phi^2 W(\mathbf{p}) d\mathbf{x}, \quad W(\mathbf{p}) = K(\frac{1}{2}|\nabla \mathbf{p}|^2 + g(\mathbf{p})), \tag{3.3.60}$$

where K is the Frank elastic constant [125] and $g(\mathbf{p}) = \frac{1}{4\delta^2}(|\mathbf{p}|^2 - 1)^2$ is a Ginzburg-Landau type penalty term, introduced to approximate the unit length constraint of $\mathbf{p}$ [62, 61], where δ is a model parameter measuring the size of the defect core.

At the interface between the viscous fluid and the liquid crystal, a surface energy known as the anchoring energy is necessary to yield a preferred orientation for the liquid crystal [42, 34]. The anchoring energy is given by

$$E_{anch} = \int_\Omega [\frac{A_1}{2}(\mathbf{p}\cdot\nabla\phi)^2 + \frac{A_2}{2}\Big(|\mathbf{p}|^2|\nabla\phi|^2 - (\mathbf{p}\cdot\nabla\phi)^2\Big)] d\mathbf{x}, \tag{3.3.61}$$

where A_1 and A_2 $(A_1 > 0, A_2 > 0)$ are the strength for the parallel and perpendicular anchoring energy, respectively.

The kinetic energy of the mixture system is

$$E_{kin} = \int_\Omega \frac{1}{2}\rho|\mathbf{u}|^2 d\mathbf{x}, \tag{3.3.62}$$

where ρ is the density of the mixture and $\mathbf{u}$ is the volume-averaged fluid velocity field.

Assuming (i). the phase field variable obeys the Cahn-Hilliard dynamics, (ii). the nematic director follows an Allen-Cahn dynamics [12, 28, 67, 68], (iii) the two fluids have a matching density $\rho = 1$ and viscosity η, we obtain the following dimensionless governing system of equations:

$$\begin{cases} \partial_t\mathbf{u} + \mathbf{u}\cdot\nabla\mathbf{u} = -\nabla p + \eta\Delta\mathbf{u} + \nabla\cdot\tau_e - \phi\nabla\mu - \mathbf{h}\nabla\mathbf{d}, \\ \nabla\cdot\mathbf{u} = 0, \\ \partial_t\mathbf{d} + \mathbf{u}\cdot\nabla\mathbf{d} - \mathbf{W}\cdot\mathbf{d} = a\mathbf{D}\cdot\mathbf{d} + M_1\mathbf{h}, \\ \partial_t\phi + \nabla\cdot(\mathbf{u}\phi) = M_2\Delta\mu, \end{cases} \tag{3.3.63}$$

where

$$\begin{aligned}
\tau_e &= -\tfrac{a}{2}(\mathbf{dh}+\mathbf{hd}) + \tfrac{1}{2}(\mathbf{dh}-\mathbf{hd}),\\
\mu &= \gamma(\Delta\phi - f(\phi)) - K\phi W(\mathbf{d}) - (A_1-A_2)\nabla\cdot((\mathbf{d}\cdot\nabla\phi)\mathbf{d})\\
&\quad -A_2\nabla\cdot(|\mathbf{d}|^2\nabla\phi),\\
\mathbf{h} &= \nabla\cdot(\tfrac{K\phi^2}{2}\nabla\mathbf{d}) + \tfrac{K\phi^2}{2}g'(\mathbf{d}) - (A_1-A_2)(\mathbf{d}\cdot\nabla\phi)\nabla\phi - A_2|\nabla\phi|^2\mathbf{d}.
\end{aligned} \tag{3.3.64}$$

Here $\mu = \frac{\delta F}{\delta\phi}$ is the chemical potential [130], $\mathbf{h} = -\frac{\delta F}{\delta\mathbf{p}}$ the molecular field, τ_e is the elastic stress tensor associated with liquid crystal dynamics [125, 126], $\mathbf{D}_{\alpha\beta} = \frac{1}{2}(\partial_\beta\mathbf{u}_\alpha + \partial_\alpha\mathbf{u}_\beta)$ is the rate of strain tensor, $\mathbf{W}_{\alpha\beta} = \frac{1}{2}(\partial_\beta\mathbf{u}_\alpha - \partial_\alpha\mathbf{u}_\beta)$ is the vorticity tensor, p is the hydrostatic pressure, $1/M_1$ is the relaxation time parameter of LC director dynamics, M_2 is the mobility parameter of the phase field function, a is a geometry parameter of liquid crystal molecules and η is the volume-averaged viscosity.

Remark 3.3.1. When the two fluids have different densities with a relatively small density difference, one can use the Boussinesq approximation [68, 121]. The case of different viscosities can usually be dealt with in a straightforward manner by assuming the viscosity is a linear or harmonic average of the phase function.

Throughout the paper, we assume the following boundary conditions

$$\mathbf{u}|_{\partial\Omega} = 0, \quad \nabla\phi\cdot\mathbf{n}|_{\partial\Omega} = 0, \quad \nabla\mu\cdot\mathbf{n}|_{\partial\Omega} = 0, \quad \nabla\mathbf{p}\cdot\mathbf{n}|_{\partial\Omega} = 0, \tag{3.3.65}$$

with $\mathbf{n}$ the unit outward normal, which warrants the boundary effect will not contribute to the energy dissipation. In fact, all results presented in this paper are valid for periodic boundary conditions as well.

Notice the fact that this system is energy dissipative, which enables us to prove the existence and uniqueness of the weak solution with certain smoothness by a standard Galerkin procedure [23]. If we use $\mathcal{E}$ to denote the total energy density, its time rate of change is given by

$$
\begin{aligned}
\frac{d\mathcal{E}}{dt} &= \tfrac{\partial}{\partial t}\int_\Omega \left(\tfrac{1}{2}\mathbf{u}^2 + E\right) d\mathbf{x} \\
&= \int_\Omega \mathbf{u}\cdot\partial_t\mathbf{u} + \tfrac{\delta E}{\delta\phi}\tfrac{\partial\phi}{\partial t} + \tfrac{\delta E}{\delta\mathbf{d}}\tfrac{\partial\mathbf{d}}{\partial t} d\mathbf{x} \\
&= \int_\Omega \mathbf{u}\cdot\Bigg(-\mathbf{u}\cdot\nabla\mathbf{u} - \nabla p + \eta\Delta\mathbf{u} - \phi\nabla\mu - \mathbf{h}\nabla\mathbf{d} + \nabla\cdot(-\tfrac{a}{2}(\mathbf{dh}+\mathbf{hd}) \\
&\quad +\tfrac{1}{2}(\mathbf{dh}-\mathbf{hd})\Bigg) + \mu(-\nabla\cdot(\mathbf{u}\phi) + M_2\Delta\mu) \\
&\quad -\mathbf{h}(-\mathbf{u}\cdot\nabla\mathbf{d} + \mathbf{W}\cdot\mathbf{d} + a\mathbf{D}\cdot\mathbf{d} + M_1\mathbf{h})d\mathbf{x} \\
&= \int_\Omega -\nabla\cdot(\mathbf{u}\tfrac{|\mathbf{u}|^2}{2}) + \tfrac{|\mathbf{u}|^2}{2}\nabla\cdot\mathbf{u} - \nabla\cdot(p\mathbf{u}) + p\nabla\cdot\mathbf{u} - \nabla\cdot(\mu\phi\mathbf{u}) \\
&\quad +\nabla\cdot(-\tfrac{a}{2}(\mathbf{dh}+\mathbf{hd})\mathbf{u} + \tfrac{1}{2}(\mathbf{dh}-\mathbf{hd})\mathbf{u}) + \nabla\cdot(\eta\mathbf{u}\nabla\mathbf{u}) - \eta|\nabla\mathbf{u}|^2 \\
&\quad -M_1|\mathbf{h}|^2 + \nabla\cdot(M_2\mu\nabla\mu) - M_2|\nabla\mu|^2 d\mathbf{x} \\
&= -\int_\Omega(\eta|\nabla\mathbf{u}|^2 + M_1|\mathbf{h}|^2 + M_2|\nabla\mu|^2)d\mathbf{x}.
\end{aligned}
\tag{3.3.66}
$$

Clearly, the parameters η, M_1 and M_2 affect the magnitude of the dissipation rate.

Decoupled semi-discrete scheme

One of the desirable properties for the discretized dissipative system to have is to maintain its own energy dissipation law that is consistent with the energy law obeyed by the continuous differential system. Practically, this is an indication for a good approximation to the differential dissipative system. This type of numerical scheme is known as the energy stable scheme. In the following, we will design a semi-discrete energy stable scheme that addresses the following issues:

- the coupling of the velocity and pressure through the incompressible condition;
- the stiffness in the phase field equation and the director equation associated with the interfacial width ε and the defect core size δ;
- the nonlinear couplings among the momentum transport equation, the phase transport equation and the director equation.

In doing so, we develop an energy stable scheme based on a stabilization technique [98]. To prove energy stability of the scheme, we have to put some constraints on the potential function $f(\phi)$ and $g(\mathbf{p})$, i.e., they satisfy the following conditions: (i). f and g have continuous second order derivatives, (ii). there exist constants L_1 and L_2 such that

$$\max_{|\mathbf{p}|\in\mathbb{R}^3} |H(\mathbf{p})| \leq L_2, \quad \max_{|\phi|\in\mathbb{R}} |f''(\phi)| \leq L_1, \tag{3.3.67}$$

where $H(\mathbf{p})$ is the Hessian matrix of $g(\mathbf{p})$.

One immediately notice that this condition is not satisfied by the usual double-well potentials $f(\phi) = \frac{1}{\varepsilon^2}\phi^2(\phi-1)^2$ and $g(\mathbf{p}) = \frac{1}{4\eta^2}(|\mathbf{p}|^2-1)^2$. However, we can modify $f(\phi)$ to quadratic growth outside of a physically meaningful interval $[-M, M]$ without affecting the solution if the maximum norm of the initial condition ϕ_0 is bounded by M. Analogously, we can modify the function g outside a ball in $\mathbb{R}^3$ of radius M. Therefore, it is common (cf. [49, 20, 98]) to consider the Cahn-Hilliard equations with a modified double-well potential $\tilde{f}(\phi)$ and Allen-Cahn with a modified $\tilde{g}$. In the following, we drop the tilde $\tilde{\bullet}$ and assume both f and g satisfy the conditions (i) and (ii) listed above. We now present the numerical scheme as follows.

The semi-discrete scheme

Given the initial conditions $\mathbf{p}^0$, ϕ^0, $\mathbf{u}^0$ and $p^0 = 0$, having computed $\mathbf{p}^n$, ϕ^n, $\mathbf{u}^n$ and p^n for $n \geq 0$, we compute $(\mathbf{p}^{n+1}, \phi^{n+1}, \mathbf{u}^{n+1}, p^{n+1})$ in the following sequence.

1. Step 1: update $\mathbf{d}^{n+1}$:

$$\begin{cases} \dot{\mathbf{d}}^{n+1} &= M_1 \mathbf{h}^{n+1} \\ \dot{\mathbf{d}}^{n+1} &= \frac{\mathbf{d}^{n+1}-\mathbf{d}^n}{\delta t} + \mathbf{u}_\star^n \cdot \nabla \mathbf{d}^n - \mathbf{W}_\star^n \cdot \mathbf{d}^n - a\mathbf{D}_\star^n \cdot \mathbf{d}^n, \\ \mathbf{h}^{n+1} &= -C_1^n\Big(\mathbf{d}^{n+1} - \mathbf{d}^n\Big) + \nabla \cdot (\frac{K}{2}(\phi^n)^2 \nabla \mathbf{d}^{n+1}) - \frac{K}{2}(\phi^n)^2 g'(\mathbf{d}^n) \\ & \quad -(A_1 - A_2)(\mathbf{d}^n \cdot \nabla\phi^n)\nabla\phi^n - A_2|\nabla\phi^n|^2\mathbf{d}^{n+1}, \\ \frac{\partial \mathbf{d}}{\partial \mathbf{n}}|_{\partial\Omega} &= 0, \end{cases} \tag{3.3.68}$$

with

$$\begin{aligned} \mathbf{u}_\star^n &= \mathbf{u}^n - \delta t \mathbf{h}^{n+1}\nabla \mathbf{d}^n + \delta t \nabla\cdot\left(\tfrac{1-a}{2}\mathbf{d}^n\mathbf{h}^{n+1} - \tfrac{1+a}{2}\mathbf{h}^{n+1}\mathbf{d}^n\right), \\ \mathbf{W}_\star^n &= \tfrac{1}{2}\Big(\nabla\mathbf{u}_\star^n - (\nabla\mathbf{u}_\star^n)^T\Big), \quad \mathbf{D}_\star^n = \tfrac{1}{2}\Big(\nabla\mathbf{u}_\star^n + (\nabla\mathbf{u}_\star^n)^T\Big). \end{aligned} \tag{3.3.69}$$

We impose an additional boundary condition $\mathbf{u}_\star^n|_{\partial\Omega} = \mathbf{0}$ in this step when physical boundary conditions are imposed instead of the periodic boundary condition. This condition sometimes is satisfied automatically if the liquid crystal phase (denoted by $\phi = 1$) is completely suspended inside Ω, namely, $\phi|_{\partial\Omega} = 0$ and $\nabla\phi|_{\partial\Omega} = \mathbf{0}$. By definition, $\mathbf{h}^{n+1}|_{\partial\Omega} = \mathbf{0}$ and $\mathbf{u}_\star^n|_{\partial\Omega} = \mathbf{u}_n|_{\partial\Omega} = \mathbf{0}$. Otherwise, this new boundary condition serves as a bona fide intermediate boundary condition for $\mathbf{d}^{n+1}$.

2. Step 2: update ϕ^{n+1}:

$$\begin{cases} \dot{\phi}^{n+1} &= M_2\Delta\mu^{n+1}, \\ \mu^{n+1} &= C_2^n(\phi^{n+1}-\phi^n) + C_3^n(\Delta\phi^{n+1}-\Delta\phi^n) + \gamma(-\Delta\phi^{n+1} + f'(\phi^n)) \\ & \quad +\phi^{n+1}W(\mathbf{d}^{n+1}) - (A_1 - A_2)\nabla\cdot\Big((\mathbf{d}^n\cdot\nabla\phi^n)\mathbf{d}^{n+1}\Big) \\ & \quad -A_2\nabla\cdot(|\mathbf{d}^{n+1}|^2\nabla\phi^{n+1}), \\ \frac{\partial\phi^{n+1}}{\partial\mathbf{n}}|_{\partial\Omega} &= 0, \quad \frac{\partial\mu^{n+1}}{\partial\mathbf{n}}|_{\partial\Omega} = 0, \end{cases} \tag{3.3.70}$$

with

$$\begin{aligned} &\dot{\phi}^{n+1} = \tfrac{\phi^{n+1}-\phi^n}{\delta t} + \nabla\cdot\Big(\mathbf{u}_{\star\star}^n\phi^n\Big), \\ &\mathbf{u}_{\star\star}^n = \mathbf{u}_\star^n - \delta t\phi^n\nabla\mu^{n+1}, \\ &W(\mathbf{d}^{n+1}) = K\Big(\tfrac{1}{2}|\nabla\mathbf{d}^{n+1}|^2 + g(\mathbf{d}^{n+1})\Big). \end{aligned} \tag{3.3.71}$$

3. Step 3: update $\mathbf{u}^{n+1}$:

$$\begin{cases} \frac{\tilde{\mathbf{u}}^{n+1}-\mathbf{u}^n}{\delta t} + (\mathbf{u}^n\cdot\nabla)\tilde{\mathbf{u}}^{n+1} = \eta\Delta\tilde{\mathbf{u}}^{n+1} - \nabla p^n - \phi^n\nabla\mu^{n+1} \\ -\mathbf{h}^{n+1}\nabla\mathbf{d}^n + \nabla\cdot\left(-\frac{a}{2}(\mathbf{d}^n\mathbf{h}^{n+1} + \mathbf{h}^{n+1}\mathbf{d}^n) + \frac{1}{2}(\mathbf{d}^n\mathbf{h}^{n+1} - \mathbf{h}^{n+1}\mathbf{d}^n)\right), \\ \tilde{\mathbf{u}}^{n+1}|_{\partial\Omega} = 0. \end{cases} \tag{3.3.72}$$

$$\begin{cases} \frac{\mathbf{u}^{n+1}-\tilde{\mathbf{u}}^{n+1}}{\delta t} & = & -\nabla(p^{n+1}-p^{n}), \\ \nabla\cdot\mathbf{u}^{n+1} & = & 0, \quad \mathbf{u}^{n+1}|_{\partial\Omega}=0. \end{cases} \tag{3.3.73}$$

In the above, C_1^n, C_2^n and C_3^n are stabilizing parameters to be determined. The above scheme is constructed by combining several effective approaches in the approximation of Cahn-Hilliard equation [98], Navier-Stokes equations [36] and phase-field models [93, 10].

Remark 3.3.2. A pressure-correction scheme [36] is used to decouple the computation of the pressure from that of the velocity.

Remark 3.3.3. We note that the explicit discretization of $f'(\phi)=\frac{2}{\varepsilon^2}\phi(1-\phi)(1-2\phi)$ often leads to a severe restriction on the time step δt when $\varepsilon \ll 1$. Thus, we introduce a stabilizing term to improve stability while preserving simplicity in (3.3.70), which allows us to treat the nonlinear term explicitly without subject to any time step constraint [93, 98, 94]. This stabilizing term introduces an error of order $O(\delta t)$ in a small region near the interface, the same order as the error introduced by treating $f(\phi)$ explicitly; so the overall truncation error of the scheme is essentially the same with or without the stabilizing term. A similar approach is applied to the director equation for the treatment of $g(\mathbf{p})$.

Remark 3.3.4. The scheme given by (3.3.68)-(3.3.73) is a fully decoupled, linear scheme. Hence, one only needs to solve a series of elliptic equations, which can be done very efficiently using fast solvers. Of course, some of these elliptic equations may be of variable coefficients.

Remark 3.3.5. If we don't study the embedded phase and boundary interaction, the new intermediate boundary condition on $\mathbf{d}^{n+1}$ in practice can be avoided so long as we don't allow the embedded phase denoted by $\phi=1$ to touch the boundary. This condition is unnecessary if we deal with a periodic boundary condition.

We shall show next that the above scheme is energy stable unconditionally assuming each step can be solved uniquely.

Semi-discrete energy dissipation law

In this section, we prove that the scheme derived in the previous section is unconditionally energy stable. Instead of going directly to the proof, we first provide some lemmas to help readers to better follow the details of the proof.

Lemma 3.3.1. *Denote* $\delta\phi^{n+1} = \phi^{n+1} - \phi^n$ *and* $\delta\delta\phi^{n+1} = \phi^{n+1} - 2\phi^n + \phi^{n-1}$. *Then, the following equalities hold,*

$$\begin{aligned}
2(\phi^{n+1} - \phi^n, \phi^{n+1}) &= \|\phi^{n+1}\|^2 - \|\phi^n\|^2 + \|\phi^{n+1} - \phi^n\|^2, \\
2(\phi^{n+1} - \phi^n, \phi^n) &= \|\phi^{n+1}\|^2 - \|\phi^n\|^2 - \|\phi^{n+1} - \phi^n\|^2, \\
2(\nabla\phi^{n+1} - \nabla\phi^n, \nabla\phi^{n+1}) &+ \|\nabla\phi^{n+1}\|^2 - \|\nabla\phi^n\|^2 + \|\nabla\phi^{n+1} - \nabla\phi^n\|^2, \\
2(\nabla\phi^{n+1} - \nabla\phi^n, \nabla\phi^n) &= \|\nabla\phi^{n+1}\|^2 - \|\nabla\phi^n\|^2 - \||\nabla\phi^{n+1} - \nabla\phi^n\|^2.
\end{aligned} \tag{3.3.74}$$

Proof. This is trivial. We can obtain the equalities by simply expanding the inner product on the right hand side and then combining the common terms. □

Lemma 3.3.2. *If* $F \in C^2(\mathcal{R}^k)$, *where* k *is the dimension, and*

$$\max_{\mathbf{x}\in\mathcal{R}^k} |F''(\mathbf{x})| < L, \tag{3.3.75}$$

$\forall \boldsymbol{x}^{n+1}, \boldsymbol{x}^n \in \mathcal{R}^k$, *the following inequality holds,*

$$(\mathbf{x}^{n+1} - \mathbf{x}^n, F'(\mathbf{x}^n)) \geq (F(\mathbf{x}^{n+1}) - F(\mathbf{x}^n), 1) - L\|\mathbf{x}^{n+1} - \mathbf{x}^n\|^2. \tag{3.3.76}$$

Proof. Notice the fact,

$$\begin{aligned}
\Big(F(\mathbf{x}^{n+1}) - F(\mathbf{x}^n), 1\Big) &= \Big(\textstyle\int_{\mathbf{x}^n}^{\mathbf{x}^{n+1}} F'(\mathbf{x})d\mathbf{x}, 1\Big) \\
&= \Big((\mathbf{x}^{n+1} - \mathbf{x}^n)F'(\mathbf{x}^n) + \textstyle\int_{\mathbf{x}^n}^{\mathbf{x}^{n+1}} (\mathbf{x}^{n+1} - \mathbf{x})F''(\mathbf{x})d\mathbf{x}, 1\Big) \\
&\leq \Big(\mathbf{x}^{n+1} - \mathbf{x}^n, F'(\mathbf{x}^n)\Big) + L\|\mathbf{x}^{n+1} - \mathbf{x}^n\|^2.
\end{aligned} \tag{3.3.77}$$

Then, we obtain

$$(\mathbf{x}^{n+1}-\mathbf{x}^n, F'(\mathbf{x}^n)) \geq (F(\mathbf{x}^{n+1})-F(\mathbf{x}^n),1) - L\|\mathbf{x}^{n+1}-\mathbf{x}^n\|^2. \tag{3.3.78}$$

□

Lemma 3.3.3. *The following identity holds,*

$$\int_\Omega (\mathbf{v}\cdot\nabla)\mathbf{u}\cdot\mathbf{u}d\mathbf{x} = 0, \tag{3.3.79}$$

provided that $\boldsymbol{n}\cdot\mathbf{v}|_\Gamma = 0$, $\mathbf{v}$ *and* $\mathbf{u}$ *are sufficiently smooth and* $\nabla\cdot\mathbf{v}=0$, *where* $\boldsymbol{n}$ *is the unit external normal of the surface.*

Proof. It is straightforward to show the following:

$$\begin{aligned} \textstyle\int_\Omega (\mathbf{v}\cdot\nabla)\mathbf{u}\cdot\mathbf{u}d\mathbf{x} &= \textstyle\int_\Omega \nabla\cdot(\mathbf{v}\frac{|\mathbf{u}|^2}{2}) - \frac{|\mathbf{u}|^2}{2}\nabla\cdot\mathbf{v}d\mathbf{x} \\ &= \textstyle\int_{\partial\Omega} \mathbf{n}\cdot\mathbf{v}\frac{|\mathbf{u}|^2}{2}ds \\ &= 0. \end{aligned} \tag{3.3.80}$$

□

Lemma 3.3.4. *If* C_1^n,C_2^n *and* C_3^n *satisfy the following conditions,*

$$\begin{aligned} C_1^n &\geq \tfrac{KL_2}{2}\|\phi^n\|_\infty^2 + \tfrac{1}{2}\max(A_1-2A_2,0)\|\nabla\phi^n\|_\infty, \\ C_2^n &\geq \gamma L_1, \\ C_3^n &\geq \tfrac{1}{2}\max(A_1-2A_2,0)\|\mathbf{d}^{n+1}\|_\infty - \tfrac{\gamma}{2}, \end{aligned} \tag{3.3.81}$$

then

$$(\phi^{n+1}-\phi^n, \mu^{n+1}) - (\mathbf{d}^{n+1}-\mathbf{d}^n, \mathbf{h}^{n+1}) \geq F^{n+1} - F^n, \tag{3.3.82}$$

where F^n *is the semi-discrete free energy defined as*

$$\begin{aligned} F^n &= F_b^n + F_{\mathbf{d}}^n + F_{anch}^n, \\ F_b^n &= \gamma\Big(\tfrac{1}{2}|\nabla\phi^n|^2 + f(\phi^n), 1\Big), \\ F_{\mathbf{d}}^n &= \Big(\tfrac{1}{2}(\phi^n)^2 W(\mathbf{d}^n), 1\Big), \quad W(\mathbf{d}^n) = K\Big(\tfrac{1}{2}|\nabla\mathbf{d}^n|^2 + g(\mathbf{d}^n)\Big), \\ F_{anch}^n &= \tfrac{A_1}{2}\Big((\nabla\phi^n\cdot\mathbf{d}^n)^2, 1\Big) + \tfrac{A_2}{2}\Big(|\mathbf{d}^n|^2|\nabla\phi^n|^2 - (\nabla\phi^n\cdot\mathbf{d}^n)^2, 1\Big). \end{aligned} \tag{3.3.83}$$

Proof. Using the definition of $\mathbf{u}^{n+1}$ in (3.3.70) and $\mathbf{h}^{n+1}$ in (3.3.68), the first term on the left hand in (3.3.82) can be expanded as

$$\begin{aligned}
&(\phi^{n+1}-\phi^n,\mu^{n+1}) = C_2^n\|\phi^{n+1}-\phi^n\|^2 + C_3^n\|\nabla\phi^{n+1}-\nabla\phi^n\|^2\\
&+\tfrac{\gamma}{2}\Big(\|\nabla\phi^{n+1}\|^2-\|\nabla\phi^n\|^2+\|\nabla\phi^{n+1}-\nabla\phi^n\|^2\Big)+\gamma(\phi^{n+1}-\phi^n,f'(\phi^n))\\
&+\Big(\phi^{n+1}-\phi^n,\phi^{n+1}W(\mathbf{d}^{n+1})\Big)-\Big(\phi^{n+1}-\phi^n,(A_1-A_2)\nabla\cdot\Big((\mathbf{d}^n\cdot\nabla\phi^n)\mathbf{d}^{n+1}\Big)\\
&+\Big(\phi^{n+1}-\phi^n,A_2\nabla\cdot(|\mathbf{d}^{n+1}|^2\nabla\phi^{n+1})\Big).
\end{aligned} \tag{3.3.84}$$

The second term on the left hand in (3.3.82) can be rewritten into the following

$$\begin{aligned}
&-(\mathbf{d}^{n+1}-\mathbf{d}^n,\mathbf{h}^{n+1}) = C_1^n\|\mathbf{d}^{n+1}-\mathbf{d}^n\|^2-(\mathbf{d}^{n+1}-\mathbf{d}^n,\nabla\cdot(\tfrac{K}{2}(\phi^n)^2\nabla\mathbf{d}^{n+1}))\\
&+(\mathbf{d}^{n+1}-\mathbf{d}^n,\tfrac{K}{2}(\phi^n)^2g'(\mathbf{d}^n))+(A_1-A_2)(\mathbf{d}^{n+1}-\mathbf{d}^n,(\mathbf{d}^n\cdot\nabla\phi^n)\nabla\phi^n)\\
&+A_2(\mathbf{d}^{n+1}-\mathbf{d}^n,|\nabla\phi^n|^2\mathbf{d}^{n+1}).
\end{aligned} \tag{3.3.85}$$

We denote

$$\begin{aligned}
T &= (\phi^{n+1}-\phi^n,\mu^{n+1}),\\
T_0 &= C_2^n\|\phi^{n+1}-\phi^n\|^2+C_3^n\|\nabla\phi^{n+1}-\nabla\phi^n\|^2,\\
T_1 &= \gamma(\phi^{n+1}-\phi^n,f'(\phi^n))+\tfrac{\gamma}{2}(\|\nabla\phi^{n+1}\|^2-\|\nabla\phi^n\|^2+\|\nabla\phi^{n+1}-\nabla\phi^n\|^2),\\
T_2 &= (\phi^{n+1}-\phi^n,\phi^{n+1}W(\mathbf{d}^{n+1})),\\
T_3 &= -(A_1-A_2)\Big(\phi^{n+1}-\phi^n,\nabla\cdot((\mathbf{d}^n\cdot\nabla\phi^n)\mathbf{d}^{n+1})\Big),\\
T_4 &= -A_2\Big(\phi^{n+1}-\phi^n,\nabla\cdot(|\mathbf{d}^{n+1}|^2\nabla\phi^{n+1})\Big).
\end{aligned} \tag{3.3.86}$$

In addition, we introduce

$$\begin{aligned}
P &= -(\mathbf{d}^{n+1}-\mathbf{d}^n,\mathbf{h}^{n+1}),\\
P_0 &= C_1^n\|\mathbf{d}^{n+1}-\mathbf{d}^n\|^2,\\
P_1 &= -(\mathbf{d}^{n+1}-\mathbf{d}^n,\nabla\cdot(\tfrac{K}{2}(\phi^n)^2\nabla\mathbf{d}^{n+1})),\\
P_2 &= (\mathbf{d}^{n+1}-\mathbf{d}^n,\tfrac{K}{2}(\phi^n)^2g'(\mathbf{d}^n)),\\
P_3 &= (A_1-A_2)(\mathbf{d}^{n+1}-\mathbf{d}^n,(\mathbf{d}^n\cdot\nabla\phi^n)\nabla\phi^n),\\
P_4 &= A_2(\mathbf{d}^{n+1}-\mathbf{d}^n,|\nabla\phi^n|^2\mathbf{d}^{n+1}),
\end{aligned} \tag{3.3.87}$$

such that

$$T = \sum_{i=0}^{4} T_i, \quad P = \sum_{i=0}^{4} P_i. \tag{3.3.88}$$

Next, we analyze these terms one-by-one. For T_1, we have,

$$\begin{aligned} T_1 &= \gamma(\phi^{n+1} - \phi^n, f'(\phi^n)) + \tfrac{\gamma}{2}(\|\nabla\phi^{n+1}\|^2 - \|\nabla\phi^n\|^2 + \|\nabla\phi^{n+1} - \nabla\phi^n\|^2) \\ &= \gamma(f(\phi^{n+1}) - f(\phi^n), 1) - \gamma L_1\|\phi^{n+1} - \phi^n\|^2 \\ &\quad + \tfrac{\gamma}{2}(\|\nabla\phi^{n+1}\|^2 - \|\nabla\phi^n\|^2 + \|\nabla\phi^{n+1} - \nabla\phi^n\|^2), \end{aligned} \tag{3.3.89}$$

i.e.

$$T_1 \geq F_b^{n+1} - F_b^n + \frac{\gamma}{2}\|\nabla\phi^{n+1} - \nabla\phi^n\|^2 - \gamma L_1\|\phi^{n+1} - \phi^n\|^2. \tag{3.3.90}$$

For T_2, we have,

$$\begin{aligned} T_2 &= (\phi^{n+1} - \phi^n, \phi^{n+1}W(\mathbf{d}^{n+1})) \\ &= (\tfrac{1}{2}(\phi^{n+1})^2 - \tfrac{1}{2}(\phi^n)^2, W(\mathbf{d}^{n+1})) + \tfrac{1}{2}\Big((\phi^{n+1} - \phi^n)^2, W(\mathbf{d}^{n+1})\Big) \\ &\geq (\tfrac{1}{2}(\phi^{n+1})^2 - \tfrac{1}{2}(\phi^n)^2, W(\mathbf{d}^{n+1})), \end{aligned} \tag{3.3.91}$$

if $W(\mathbf{d}) \geq 0$, $\forall \mathbf{d} \in \mathcal{R}^3$, which is true in our case.

For P_1, we have

$$\begin{aligned} P_1 &= (\nabla\mathbf{d}^{n+1} - \nabla\mathbf{d}^n, \tfrac{K}{2}(\phi^n)^2\nabla\mathbf{d}^{n+1}) \\ &= (\tfrac{K}{2}(\phi^n)^2, \tfrac{1}{2}(\nabla\mathbf{d}^{n+1})^2 - \tfrac{1}{2}(\nabla\mathbf{d}^n)^2) + (\tfrac{K}{2}(\phi^n)^2, (\nabla\mathbf{d}^{n+1} - \nabla\mathbf{d}^n)^2) \\ &\geq (\tfrac{K}{2}(\phi^n)^2, \tfrac{1}{2}(\nabla\mathbf{d}^{n+1})^2 - \tfrac{1}{2}(\nabla\mathbf{d}^n)^2). \end{aligned} \tag{3.3.92}$$

For P_2, we use Lemma 3.3.2 and obtain

$$\begin{aligned} P_2 &\geq (\tfrac{K}{2}(\phi^n)^2, g(\mathbf{d}^{n+1}) - g(\mathbf{d}^n)) - (\tfrac{K}{2}(\phi^n)^2, L_2(\mathbf{d}^{n+1} - \mathbf{d}^n)^2) \\ &\geq (\tfrac{K}{2}(\phi^n)^2, g(\mathbf{d}^{n+1}) - g(\mathbf{d}^n)) - \tfrac{L_2K}{2}\|(\phi^n)^2\|_\infty\|\mathbf{d}^{n+1} - \mathbf{d}^n\|^2. \end{aligned} \tag{3.3.93}$$

Combining T_2, P_1 and P_2, we obtain

$$T_2 + P_1 + P_2 \geq F_{\mathbf{d}}^{n+1} - F_{\mathbf{d}}^n - \frac{L_2K}{2}\|(\phi^n)^2\|_\infty\|\mathbf{d}^{n+1} - \mathbf{d}^n\|^2. \tag{3.3.94}$$

Combining T_3 and P_3, we have

$$\begin{aligned}
& T_3 + P_3 \\
= \; & (A_1 - A_2)\Big(\Big(\mathbf{d}^{n+1} - \mathbf{d}^n, (\mathbf{d}^n \cdot \nabla\phi^n)\nabla\phi^n\Big) \\
& -\Big(\phi^{n+1} - \phi^n, \nabla \cdot \Big((\mathbf{d}^n \cdot \nabla\phi^n)\mathbf{d}^{n+1}\Big)\Big)\Big) \\
= \; & (A_1 - A_2)\Big(\Big(\mathbf{d}^{n+1} - \mathbf{d}^n, (\mathbf{d}^n \cdot \nabla\phi^n)\nabla\phi^n\Big) \\
& +\Big(\nabla\phi^{n+1} - \nabla\phi^n, (\mathbf{d}^n \cdot \nabla\phi^n)\mathbf{d}^{n+1}\Big)\Big) \\
= \; & (A_1 - A_2)\Big((\mathbf{d}^n \cdot \nabla\phi^n, \mathbf{d}^{n+1} \cdot \nabla\phi^{n+1}) - (\mathbf{d}^n \cdot \nabla\phi^n, \mathbf{d}^n \cdot \nabla\phi^n)\Big) \\
= \; & \tfrac{A_1 - A_2}{2}\Big(\|\mathbf{d}^{n+1} \cdot \nabla\phi^{n+1}\|^2 - \|\mathbf{d}^n \cdot \nabla\phi^n\|^2 - \|\mathbf{d}^{n+1} \cdot \nabla\phi^{n+1} - \mathbf{d}^n \cdot \nabla\phi^n\|^2\Big).
\end{aligned} \tag{3.3.95}$$

Adding T_4 with P_4, we have

$$\begin{aligned}
& T_4 + P_4 \\
= \; & A_2\Big((\nabla\phi^{n+1} - \nabla\phi^n, |\mathbf{d}^{n+1}|^2\nabla\phi^{n+1}) + (\mathbf{d}^{n+1} - \mathbf{d}^n, |\nabla\phi^n|^2\mathbf{d}^{n+1})\Big) \\
= \; & \tfrac{A_2}{2}\Big(\Big(|\nabla\phi^{n+1}|^2 - |\nabla\phi|^2 + |\nabla\phi^{n+1} - \nabla\phi^n|^2, |\mathbf{d}^{n+1}|^2\Big) + \\
& \Big(|\mathbf{d}^{n+1}|^2 - |\mathbf{d}^n|^2 + |\mathbf{d}^{n+1} - \mathbf{d}^n|^2, |\nabla\phi^n|^2\Big)\Big) \\
= \; & \tfrac{A_2}{2}\Big(|\mathbf{d}^{n+1}|^2|\nabla\phi^{n+1}|^2 - |\mathbf{d}^n|^2|\nabla\phi^n|^2, 1\Big) + \tfrac{A_2}{2}(|\nabla\phi^{n+1} - \nabla\phi^n|^2, |\mathbf{d}^{n+1}|^2) \\
& +\tfrac{A_2}{2}(|\mathbf{d}^{n+1} - \mathbf{d}^n|^2, |\nabla\phi^n|^2).
\end{aligned} \tag{3.3.96}$$

Combining T_3, T_4, P_3 and P_4, we have

$$\begin{aligned}
& T_3 + T_4 + P_3 + P_4 = F_{anch}^{n+1} - F_{anch}^n - \tfrac{A_1 - A_2}{2}(\|\mathbf{d}^{n+1} \cdot \nabla\phi^{n+1} - \mathbf{d}^n \cdot \nabla\phi^n\|^2) \\
& +\tfrac{A_2}{2}(|\nabla\phi^{n+1} - \nabla\phi^n|^2, |\mathbf{d}^{n+1}|^2) + \tfrac{A_2}{2}(|\mathbf{d}^{n+1} - \mathbf{d}^n|^2, |\nabla\phi^n|^2).
\end{aligned} \tag{3.3.97}$$

Note that

$$\begin{aligned}
& -\|\mathbf{d}^{n+1} \cdot \nabla\phi^{n+1} - \mathbf{d}^n \cdot \nabla\phi^n\|^2 \\
= \; & -\|\mathbf{d}^{n+1} \cdot \nabla\phi^{n+1} - \mathbf{d}^{n+1} \cdot \nabla\phi^n + \mathbf{d}^{n+1} \cdot \nabla\phi^n - \mathbf{d}^n \cdot \nabla\phi^n\|^2 \\
\geq \; & -\|\mathbf{d}^{n+1} \cdot (\nabla\phi^{n+1} - \nabla\phi^n)\|^2 - \|\nabla\phi^n \cdot (\mathbf{d}^{n+1} - \mathbf{d}^n)\|^2 \\
\geq \; & -(|\mathbf{d}^{n+1}|^2, |\nabla\phi^{n+1} - \nabla\phi^n|^2) - (|\nabla\phi^n|^2, |\mathbf{d}^{n+1} - \mathbf{d}^n|^2).
\end{aligned} \tag{3.3.98}$$

Then, we have

$$\begin{aligned}&T_3+T_4+P_3+P_4 \geq F_{anch}^{n+1}-F_{anch}^{n}-\tfrac{1}{2}\max(A_1-2A_2,0)\\&\Big(\|(\mathbf{d}^{n+1})^2\|_\infty\|\nabla\phi^{n+1}-\nabla\phi^n\|^2+\|(\nabla\phi^n)^2\|_\infty\|\mathbf{d}^{n+1}-\mathbf{d}^n\|^2\Big).\end{aligned} \tag{3.3.99}$$

Adding up (3.3.90),(3.3.94), (3.3.99), T_0 and P_0, we have

$$\begin{aligned}&(\phi^{n+1}-\phi^n,\mu^{n+1})-(\mathbf{d}^{n+1}-\mathbf{d}^n,\mathbf{h}^{n+1})\\
=\;&\textstyle\sum_{i=0}^4 T_i+\sum_{i=0}^4 P_i\\
\geq\;&F^{n+1}-F^n+C_2^n\|\phi^{n+1}-\phi^n\|^2+C_3^n\|\nabla\phi^{n+1}-\nabla\phi^n\|^2+C_1^n\|\mathbf{d}^{n+1}-\mathbf{d}^n\|^2\\
&+\tfrac{\gamma}{2}\|\nabla\phi^{n+1}-\nabla\phi^n\|^2-\gamma L_1\|\phi^{n+1}-\phi^n\|^2-\tfrac{KL_2}{2}\|\phi^n\|_\infty^2\|\mathbf{d}^{n+1}-\mathbf{d}^n\|^2\\
&-\tfrac{1}{2}\max(A_1-2A_2,0)\Big(\|(\mathbf{d}^{n+1})^2\|_\infty\|\nabla\phi^{n+1}-\nabla\phi^n\|^2\\
&+\|(\nabla\phi^n)^2\|_\infty\|\mathbf{d}^{n+1}-\mathbf{d}^n\|^2\Big)\\
=\;&F^{n+1}-F^n+(C_1^n-\tfrac{KL_2}{2}\|\phi^n\|_\infty^2-\tfrac{1}{2}\max(A_1-2A_2,0)\|\nabla\phi^n\|_\infty)\\
&\|\mathbf{d}^{n+1}-\mathbf{d}^n\|^2+(C_2^n-\gamma L_1)\|\nabla\phi^{n+1}-\nabla\phi^n\|^2\\
&+(C_3^n+\tfrac{\gamma}{2}-\tfrac{1}{2}\max(A_1-2A_2,0)\|\mathbf{d}^{n+1}\|_\infty)\|\nabla\phi^{n+1}-\nabla\phi^n\|^2.\end{aligned} \tag{3.3.100}$$

By the assumption, we have,

$$\begin{aligned}C_1^n &\geq \tfrac{KL_2}{2}\|\phi^n\|_\infty^2+\tfrac{1}{2}\max(A_1-2A_2,0)\|\nabla\phi^n\|_\infty,\\
C_2^n &\geq \gamma L_1,\\
C_3^n &\geq \tfrac{1}{2}\max(A_1-2A_2,0)\|\mathbf{d}^{n+1}\|_\infty-\tfrac{\gamma}{2}.\end{aligned} \tag{3.3.101}$$

Finally, we arrive at

$$(\phi^{n+1}-\phi^n,\mu^{n+1})-(\mathbf{d}^{n+1}-\mathbf{d}^n,\mathbf{h}^{n+1})\geq F^{n+1}-F^n. \tag{3.3.102}$$

□

Theorem 3.3.1. *Under the conditions given in Lemma 3.3.4, the scheme given by* (3.3.68)-(3.3.73) *admits a unique solution satisfying the following semi-discrete energy dissipation law:*

$$\begin{aligned}&\tfrac{1}{2}\|\mathbf{u}^{n+1}\|^2+F^{n+1}+\tfrac{\delta t^2}{2}\|\nabla p^{n+1}\|^2+\delta t\Big(\eta\|\nabla\tilde{\mathbf{u}}^{n+1}\|^2+M_2\|\nabla\mu^{n+1}\|^2\\&+M_1\|\mathbf{h}^{n+1}\|^2\Big)\leq\tfrac{1}{2}\|\mathbf{u}^n\|^2+F^n+\tfrac{\delta t^2}{2}\|\nabla p^n\|^2,\end{aligned} \tag{3.3.103}$$

where the semi-discrete energy F^n is defined in (3.3.83).

Proof. From the definition of $\mathbf{u}_\star^n$ in equation (3.3.69) and $\mathbf{u}_{\star\star}^n$ in equation (3.3.71), we can rewrite the momentum equation as follows

$$\frac{\tilde{\mathbf{u}}^{n+1}-\mathbf{u}_{\star\star}^n}{\delta t}+(\mathbf{u}^n\cdot\nabla)\tilde{\mathbf{u}}^{n+1}-\eta\nabla\tilde{\mathbf{u}}^{n+1}+\nabla p^n=0. \tag{3.3.104}$$

Taking the inner-product of (3.3.104) with $2\delta t\tilde{\mathbf{u}}^{n+1}$, we obtain,

$$\|\tilde{\mathbf{u}}^{n+1}\|^2-\|\mathbf{u}_{\star\star}^n\|^2+\|\tilde{\mathbf{u}}^{n+1}-\mathbf{u}_{\star\star}^n\|^2+2\eta\delta\|\nabla\tilde{\mathbf{u}}^{n+1}\|^2+2\delta t(\nabla p^n,\tilde{\mathbf{u}}^{n+1})=0. \tag{3.3.105}$$

To deal with the pressure term, we take the inner product of (3.3.73) with $2\delta t^2\nabla p^n$ to arrive at

$$\delta t^2(\|\nabla p^{n+1}\|^2-\|\nabla p^n\|^2-\|\nabla p^{n+1}-\nabla p^n\|^2)=2\delta t(\tilde{\mathbf{u}}^{n+1},\nabla p^n). \tag{3.3.106}$$

Taking the inner product of (3.3.73) with $\mathbf{u}^{n+1}$, we obtain

$$\|\mathbf{u}^{n+1}\|^2+\|\mathbf{u}^{n+1}-\tilde{\mathbf{u}}^{n+1}\|^2=\|\tilde{\mathbf{u}}^{n+1}\|^2. \tag{3.3.107}$$

It follows from (3.3.73) directly that

$$\delta t^2\|\nabla p^{n+1}-\nabla p^n\|^2=\|\tilde{\mathbf{u}}^{n+1}-\mathbf{u}^{n+1}\|^2. \tag{3.3.108}$$

Combining (3.3.105)-(3.3.108), we obtain

$$\begin{aligned}\|\mathbf{u}^{n+1}\|^2-\|\mathbf{u}_{\star\star}^n\|^2+\|\tilde{\mathbf{u}}^{n+1}-\mathbf{u}_{\star\star}^n\|^2+\delta t^2(\|\nabla p^{n+1}\|^2-\|\nabla p^n\|^2)&\\+2\eta\delta t\|\nabla\tilde{\mathbf{u}}^{n+1}\|^2=0.&\end{aligned} \tag{3.3.109}$$

If we take the inner product of (3.3.68) with $2\delta t\mathbf{h}^{n+1}$, we get

$$\begin{aligned}2\delta tM_1\|\mathbf{h}^{n+1}\|^2-2\delta t(\mathbf{h}^{n+1},(\mathbf{u}_\star^n\cdot\nabla)\mathbf{d}^n)-2(\mathbf{d}^{n+1}-\mathbf{d}^n,\mathbf{h}^{n+1})&\\+2\delta t\Big(\mathbf{h}^{n+1},(\mathbf{W}_\star^n+a\mathbf{D}_\star^n)\cdot\mathbf{d}^n\Big)=0.&\end{aligned} \tag{3.3.110}$$

Taking the inner product of (3.3.69) with $2\mathbf{u}_\star^n$, we obtain

$$\begin{aligned}\|\mathbf{u}_\star^n\|^2-\|\mathbf{u}^n\|^2+\|\mathbf{u}_\star^n-\mathbf{u}^n\|^2-2\delta t(\mathbf{h}^{n+1}\nabla\mathbf{d}^n,\mathbf{u}_\star^n))&\\-\delta t\Big(\nabla\cdot(\tfrac{1-a}{2}\mathbf{d}^n\mathbf{h}^{n+1}-\tfrac{1+a}{2}\mathbf{h}^{n+1}\mathbf{d}^n),\mathbf{u}_\star^n\Big)=0.&\end{aligned} \tag{3.3.111}$$

Adding (3.3.110) with (3.3.111) and noticing the fact that

$$\Big(\nabla\cdot(\frac{1-a}{2}\mathbf{d}^n\mathbf{h}^{n+1}-\frac{1+a}{2}\mathbf{h}^{n+1}\mathbf{d}^n),\mathbf{u}_\star^n\Big)=\Big(\mathbf{h}^{n+1},(\mathbf{W}_\star^n+a\mathbf{D}_\star^n)\cdot\mathbf{d}^n\Big),\quad(3.3.112)$$

we arrive at

$$\|\mathbf{u}_\star^n\|^2-\|\mathbf{u}^n\|^2+\|\mathbf{u}_\star^n-\mathbf{u}^n\|^2+2\delta tM_1\|\mathbf{h}^{n+1}\|^2-2(\mathbf{d}^{n+1}-\mathbf{d}^n,\mathbf{h}^{n+1})=0.\quad(3.3.113)$$

If we take the inner product of (3.3.70) with $2\delta t\mu^{n+1}$, we obtain

$$2(\phi^{n+1}-\phi^n,\mu^{n+1})+2\delta t(\nabla\cdot(\phi^n\mathbf{u}_{\star\star}^n),\mu^{n+1})+2M_2\delta t\|\nabla\mu^{n+1}\|^2=0.\quad(3.3.114)$$

Taking the inner product of (3.3.71) with $2\mathbf{u}_{\star\star}^n$, we have

$$\|\mathbf{u}_{\star\star}^n\|^2-\|\mathbf{u}_\star^n\|^2+\|\mathbf{u}_{\star\star}^n-\mathbf{u}_\star^n\|^2+2\delta t(\mathbf{u}_{\star\star}^n,\phi^n\nabla\mu^{n+1}))=0.\quad(3.3.115)$$

Adding (3.3.114) with (3.3.115), we arrive at

$$\|\mathbf{u}_{\star\star}^n\|^2-\|\mathbf{u}_\star^n\|^2+\|\mathbf{u}_{\star\star}^n-\mathbf{u}_\star^n\|^2+2(\phi^{n+1}-\phi^n,\mu^{n+1})+2M_2\delta t\|\nabla\mu^{n+1}\|^2=0.\quad(3.3.116)$$

Finally, adding up the equations (3.3.109),(3.3.113), (3.3.116) and dividing both side by 2, we obtain

$$\begin{aligned}&\tfrac{1}{2}\Big(\|\mathbf{u}^{n+1}\|^2-\|\mathbf{u}^n\|^2+\|\tilde{\mathbf{u}}^{n+1}-\mathbf{u}_{\star\star}^n\|^2\Big)+\tfrac{1}{2}\delta t^2(\|\nabla p^{n+1}\|-\|\nabla p^n\|^2)\\&+\eta\delta t\|\nabla\tilde{\mathbf{u}}^{n+1}\|^2+\delta tM_2\|\nabla\mu^{n+1}\|^2+\delta tM_1\|\mathbf{h}^{n+1}\|^2\\&+(\phi^{n+1}-\phi^n,\mu^{n+1})-(\mathbf{d}^{n+1}-\mathbf{d}^n,\mathbf{h}^{n+1})=0.\end{aligned}\quad(3.3.117)$$

According to Lemma 3.3.4

$$(\phi^{n+1}-\phi^n,\mu^{n+1})-(\mathbf{d}^{n+1}-\mathbf{d}^n,\mathbf{h}^{n+1})\geq F^{n+1}-F^n,\quad(3.3.118)$$

hence, we finally obtain

$$\begin{aligned}&\tfrac{1}{2}\|\mathbf{u}^{n+1}\|^2+F^{n+1}+\tfrac{\delta t^2}{2}\|\nabla p^{n+1}\|^2+\delta t\Big(\eta\|\nabla\tilde{\mathbf{u}}^{n+1}\|^2+M_2\|\nabla\mu^{n+1}\|^2\\&+M_1\|\mathbf{h}^{n+1}\|^2\Big)\leq\tfrac{1}{2}\|\mathbf{u}^n\|^2+F^n+\tfrac{\delta t^2}{2}\|\nabla p^n\|^2.\end{aligned}\quad(3.3.119)$$

□

CHAPTER 4

MATHEMATICAL MODELING AND SIMULATIONS OF BIOFILMS DYNAMICS

Bacteria are ubiquitous in our daily life. As human beings living in a society, in their natural environments, bacteria do not exist as isolated cells but grow and survive in organized communities, which is known as biofilms.

In this chapter, we first briefly review the biological background of biofilms and related theoretical models in the literature. After that, we show a general modeling framework for studying biofilm dynamics. In particular, the antimicrobial persistence of biofilms and quorum sensing in biofilms are investigated.

4.1 BACKGROUND OF BIOFILMS RESEARCH

Biofilms are usually formed on moisture surfaces by bacteria colonies. And it is commonly perceived by the medical community that biofilms are responsible for many diseases or ailments associated with chronic infections[90]. Unlike a planktonic bacterium, biofilms are always hard to be eradicated by the standard antimicrobial treatment [58]. Thus, an understanding of the mechanism that underlies biofilm persistence to antimicrobial agents can greatly enhance therapeutic treatment of diseases related with biofilms.

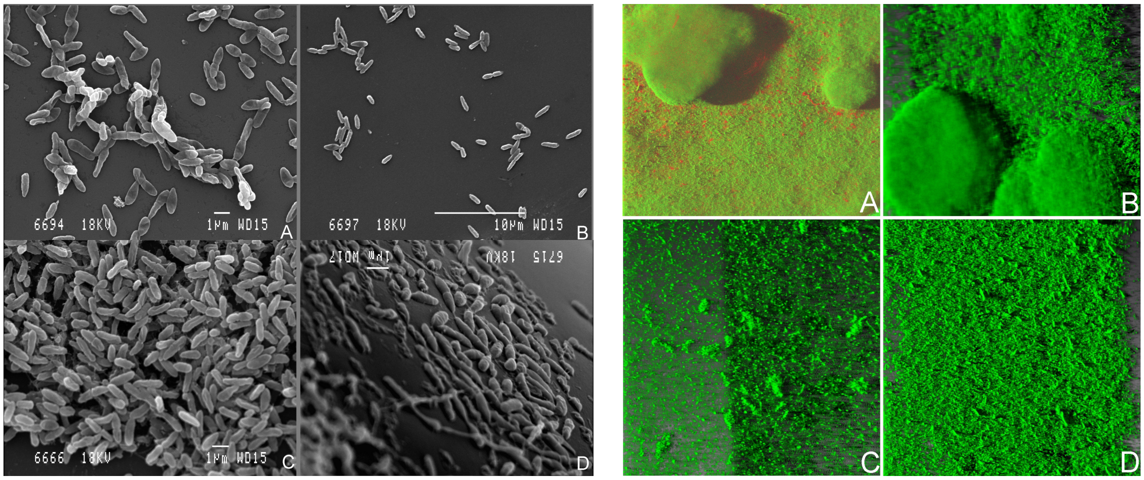

(a) (b)

Figure 4.1: Biofilm of Pseudomonas at different scales. (A) Scanning electron microscopy images of Pseudomonas aeruginosa isolated attaching to glass surfaces; (B) CLSM images of GFP-tagged Pseudomonas aeruginosa biofilms in a glass capillary flow reactor 72h post-inoculation, shwoing variation in biofilm structure. Images are from [21].

Biofilm development

Conceptually, biofilms could be defined as an aggregate of micro-organisms in which cells adhere to each other on biotic or abiotic surfaces. These adherent cells are frequently embedded within a self-produced slimy, glue-like matrix of extracellular polymeric substances (EPS), which takes the role as facilities in biofilms. Besides water, the main components in biofilms are microbial cells and EPS. In Figure 4.1(A), scanning electron microscopy images for biofilms of Pseudomonas aeruginosa are shown. And Confocal laser scanning microscopy image of mushroom shape biofilms are shown in Figure 4.1(B).

The basic process of biofilm development is summarized as five stages, as shown in Figure 4.2(A). Mainly, the bacteria would go through a cycle of attachment, growth and dispersal (or death). It has been suggested that biofilm development is influenced by a number of different process such as adhesion, detachment, nutrient transport, quorum sensing, cell death and active dispersal, as well as other stresses from sur-

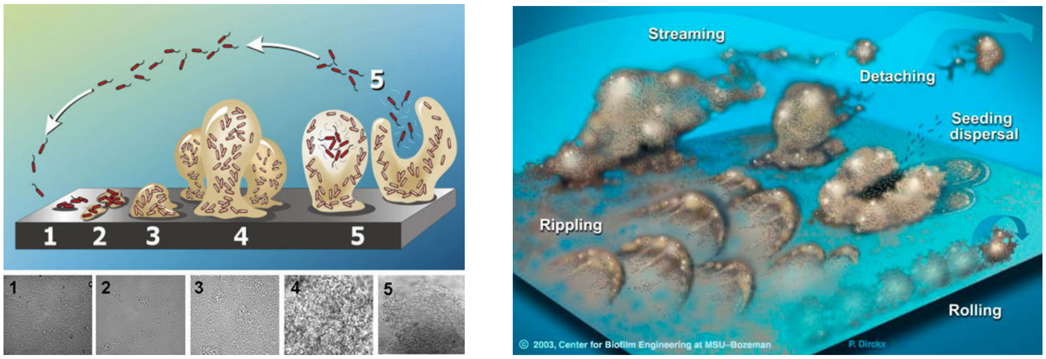

(a) Biofilm formation (b) Biofilm migration

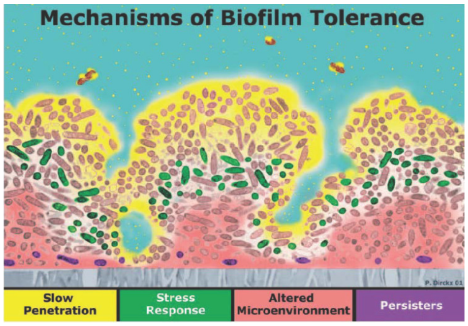

(c) Mechanisms of biofilm tolerance

Figure 4.2: Biofilm development. This figure shows cartoons of biofilm development. (a) Five stages of biofilm development: (1) attachment; (2) lag-stage; (3) exponential-stage; (4) stationary stage; (5) dispersal or detachment (from [76]); (b) biofilm migration under hydrodynamic shear (from Center for Biofilm Engineering at MSU); (c) mechanisms of biofilm tolerance to antimicrobial agents (from Center for Biofilm Engineering at MSU).

roundings, saying hydrodynamic shear. Under hydrodynamic shear, various pattern formations have been observed, namely streaming, rippling and rolling. When the hydrodynamic stress is high, biofilm detachment, rolling or seeding dispersal might happen, as shown in Figure 4.2(B).

Quorum-sensing in biofilms

Though bacteria are single cellular, bacteria in biofilms always show multi-cellular phenomenons. One particular reason is bacteria in biofilms can communicate and co-operate by secreting some dilutable signaling molecule and sensing its concentration, which mechanism is known as quorum sensing (QS).

In details, these bacteria will secrete some QS molecules (known as autoinducers) and they also have a receptor, which can bind the QS molecules secreted by other bacteria. Once the concentration of the autoinducers has reached certain threshold (which is likely happen where there are dense bacteria, since otherwise the QS molecule will diffuse aways without reaching the threshold), the binding between the receptor with the inducer will activate certain gene transcription. Quorum sensing has been shown to be responsible for mediating a variety of social activities in biofilms, which include the secretion of diverse byproducts, biofilm growth [32], swarming motility and virulence gene expressions [86], biofilm dispersion [16], antimicrobial resistance [110] and so on. Especially, the phenomenon of quorum sensing regulating expopolysacharride production during biofilm formation has been widely reported [116, 112, 71].

Antimicrobial tolerance in biofilms

Biofilms are known to be tolerance to antimicrobial treatment. Besides gene mutations, which is out scope of this thesis, there are several hypothesis, as shown in Figure 4.2(C), depending on specific biofilms.

The first and most straightforward explanation for the failure of antimicrobial treatment of biofilms is the slow-penetration induced by the extra cellular substances (EPS). Basically, EPS is believed to act as a protective barrier to prevent the antimicrobial agents from penetrating deep into the biofilm region, either by reacting with antimicrobial agents [101] or by simply slowing down the diffusion rate via its densely distributed network meshes [107].

Besides, the common recognition on this antimicrobial tolerance lays on the existence of a small portion of bacteria, which is in dormant status and tolerance to antimicrobial agents, usually called persister. It is commonly admitted that persister is different from drug-resistant mutants, whose antibiotic tolerance is heritable.

From the clinical point of view, understanding the mechanism of persister formation would be essential for biofilm control and thereby impact on the treatment of diseases responsible by biofilms. For review papers on mechanisms underlying the persister formation, readers are referred to the works by Kim Lewis [58] and [59]. As dormant variants of regular bacterial cells, which doesn't undergo genetic changes, it is convinced that persister are converted from regular cells due to stresses [3], such as nutrient depletion [7, 2], existence of antimicrobial agents [84] and so on. Later, when the environment is tolerable, say nutrient is sufficient or the concentration of antimicrobial agents drops under a certain threshold value, biofilms can relapse [9], which implies that persister convert back into susceptible bacteria for regrowth.

A review of existing mathematical models

From the mathematical perspective, many models have been proposed trying to interpret experimental observations on biofilm structures and function. We provide a brief review in this subsection. Interested readers can refer to [50, 114] for further details. In terms of length scale we are focusing on, the mathematical models in literature can be categorized into: (i) microscopic scale models (agent based models), such as [1]; (ii) mesoscopic scale models (kinetic theory models), such as [113] and (iii) macroscopic scale models (continuum theories), such as [130].

On the issue of biofilm persistence to antimicrobial agents, simple mathematical models have also been developed to test certain mechanisms for persister formation based on the experimental evidence that supports the concept of persister. For instance in [88], the author claims using a simple mathematical model that persister formation can lead to higher bacterial persistence to antimicrobial agents than those grown in plancktonic culture. In [40], a 3D agent-based model for biofilm dynamics under antimicrobial treatment was developed, in which it showed that substrate limitation can contribute to the persistence of biofilms to antimicrobial agents. Cogan has worked on possible mechanisms of persister formation using time-dependent, but spatially homogeneous models recently [18, 19, 54].

Concerning coupling biofilm growth with quorum sensing features, several mathematical models have been developed. The dependence of quorum sensing on the depth of a growing biofilm is discussed in [17]. In [77], the evolution of quorum sensing in bacterial biofilms is simulated by an individual-based model. In [81], quorum sensing regulation and its heterogeneity in Pseudomonas syringae on leaves is studied by treating it as a non-negative stochastic process. Recently, [72] proposed a single cell spatial model for quorum sensing. The inhibition of quorum sensing is modeled by [29] as a stochastic process on the level of individual cells, claiming he time at which treatment is initiated is crucial for effective prevention of quorum sensing. The hydrodynamic effects on quorum sensing induction have also been investigated theoretically. A 2D partial differential equation model coupled with the Stokes flow is proposed in [30] and later they extended this model [31] and proved its well-posedness in [103]. Another 2D continuum model with Stokes background flow is proposed in [111], where the shape of biofilms at the onset of the hydrodynamic shear is studied.

Recently, modeling biofilms as multiphase complex fluids has emerged as a promising approach to address some complex and intriguing issues associated with biofilm dynamics[117, 130], where bacteria are regarded as colloids and the EPS is modeled as a polymer gel. This approach is promising, as from experimental observation, biofilms behave like viscoelastic fluids. In such an approach, a complex fluid model can be devised to analyze the structure formation and function of biofilms in a hydrodynamical setting. In this research direction, the work of Wang et al.[130, 131] represents some latest development. They developed hydrodynamic models for biofilm formation and flow-biomass interaction by treating the biofilm system as a single fluid model with multiple effective fluid components. And in text section, we will extend their work to study quorum sensing and antimicrobial persistence in biofilms.

4.2 A 3D NUMERICAL STUDY OF ANTIMICROBIAL PERSISTENCE IN HETEROGENEOUS MULTI-SPECIES BIOFILMS

Mathematical model formulation

To make our current work consistent with the previous models [130, 131], we adopt the same notations here. Recall that in [130], ϕ_n is used to denote the volume fraction of biomass (bacteria + EPS) and ϕ_s the volume fraction of the effective solvent (water+nutrient). By assuming incompressibility of the fluid mixture, it follows that

$$\phi_n + \phi_s = 1. \tag{4.2.1}$$

In order to analyse the dynamics inside biofilms with different bacteria phenotypes, as well as EPS, further refinement of the model is necessary. In this paper, we denote the volume fraction of bacteria and EPS by ϕ_b and ϕ_p, respectively. In addition, the bacteria are further categorized into three different phenotypes according to their reaction to antimicrobial treatment: the susceptible bacteria, which are susceptible to antimicrobial treatment, the persister bacteria, which are persistent to antimicrobial treatment and the dead bacteria, which lose mortality after antimicrobial treatment. Their volume fractions are denoted, respectively, as ϕ_{bs}, ϕ_{bp} and ϕ_{bd}. I.e.,

$$\phi_n = \phi_b + \phi_p, \quad \phi_b = \phi_{bs} + \phi_{bp} + \phi_{bd}. \tag{4.2.2}$$

For hydrodynamic properties, we use ρ_b, ρ_p and ρ_s to denote the density of bacteria, EPS and solvent, and $\mathbf{v}_b$, $\mathbf{v}_p$ and $\mathbf{v}_s$ for the velocity of bacteria, EPS, and solvent, respectively. Then, the volume averaged velocity and density are given respectively by

$$\mathbf{v} = \phi_b\mathbf{v}_b + \phi_p\mathbf{v}_p + \phi_s\mathbf{v}_s, \quad \rho = \phi_b\rho_b + \phi_p\rho_p + \phi_s\rho_s. \tag{4.2.3}$$

In this model, we make a simplifying assumption that all components in the biomass including the bacteria and EPS share the same density and the same property in terms of hydrodynamic interaction with solvent. The modified Flory-Huggins mixing free energy with a conformational entropy is adopted to model the molecular interaction (molecular level mixing) in this biological system [130],

$$f = k_B T \left(\frac{\gamma_1}{2} \|\nabla \phi_n\|^2 + \gamma_2 \left(\frac{\phi_n}{N} \ln \phi_n + \phi_s \ln \phi_s + \chi \phi_n \phi_s \right) \right), \tag{4.2.4}$$

in which γ_1 and γ_2 parametrize the strength of the conformation entropy and bulk mixing free energy, respectively, χ is the mixing parameter, N is the extended polymerization index for biomass, k_B is the Boltzmann constant and T is the absolute temperature. This free energy can be easily extended into multiple components by proposing every component interact with solvent distinctly. Readers can read our related work [64, 65] for more details. However, in this paper, we keep this form for simplicity.

Besides the biomass components, we also introduce some functional components, whose molecular weight is small compared with the components comprising the biomass. For these molecules, we neglect their mass in the model, but keep their biochemical effects. We include the nutrient, QS molecules, antimicrobial agents and a functional protein (named growth factor in this paper), which represents the extra-cellular RNA or enzymes that are necessary for bacteria proliferation and QS molecules production, in this class of functional biomass components. Their concentrations are denoted as C, H, A and Q, respectively. To help the reader to better understand the biofilm system we are studying in this paper, a schematic portrait of a biofilm colony and its effective components are shown in Figure 4.3.

Transport equations for biomass

Given the mixing free energy density functional f in equation (4.2.4), the "extended" chemical potentials with respect to each component can be calculated as

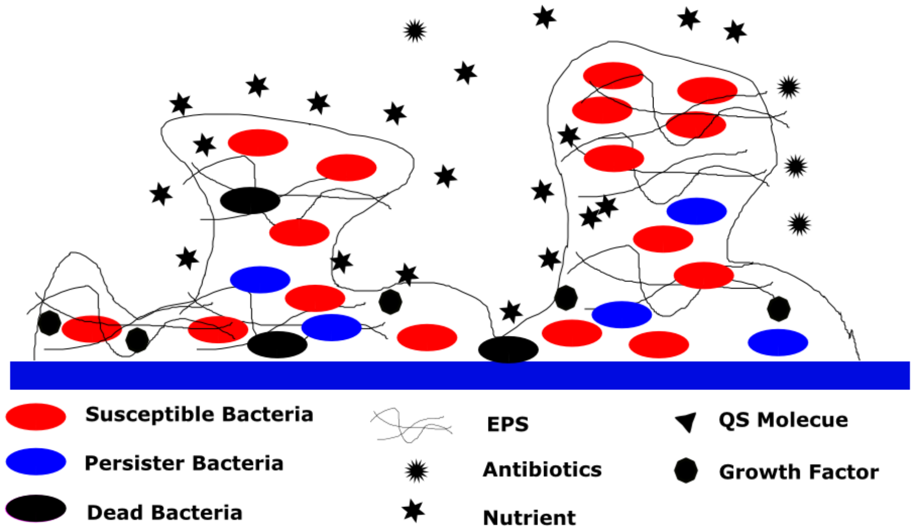

Figure 4.3: A schematic portrait of effective components in the biofilm system studied. The blue bar denotes the solid substrate, where the biofilm is attached.

follows

$$\mu_{bs} = \frac{\delta f}{\delta \phi_{bs}}, \quad \mu_{bp} = \frac{\delta f}{\delta \phi_{bp}}, \quad \mu_{bd} = \frac{\delta f}{\delta \phi_{bd}}, \quad \mu_{p} = \frac{\delta f}{\delta \phi_{p}}. \tag{4.2.5}$$

The transport of each biomass component is assumed to be convected by the volume-averaged velocity as well as driven by the osmotic pressure. Hence, we propose the transport equation for the volume fraction of each biomass component as governed by a Cahn-Hilliard equation with reactive dynamics,

$$\begin{aligned} \partial_t \phi_{bi} + \nabla \cdot (\phi_{bi}\mathbf{v}) &= \nabla \cdot (\lambda_{bi}\phi_{bi}\nabla\mu_{bi}) + g_{bi}, \quad i = s, p, d. \\ \partial_t \phi_{p} + \nabla \cdot (\phi_{p}\mathbf{v}) &= \nabla \cdot (\lambda_{p}\phi_{p}\nabla\mu_{p}) + g_{p}, \end{aligned} \tag{4.2.6}$$

where $g_{bi}, i = s, p, d$ and g_p are the reactive terms for the bacteria and EPS, respectively; λ_{bi}, $i = s, p, d$ and λ_p are the mobility parameters for the transporting components. Notice that, if we add up the equations in (4.2.6), we end up with

$$\partial_t \phi_n + \nabla \cdot (\phi_n \mathbf{v}) = \nabla \cdot \left(\lambda \nabla \frac{\delta F}{\delta \phi_n} \right) + g_n, \tag{4.2.7}$$

where the motility parameter and reactive term are given respectively by

$$\begin{aligned} \lambda &= \lambda_{bs}\phi_{bs} + \lambda_{bp}\phi_{bp} + \lambda_{bd}\phi_{bd} + \lambda_{p}\phi_{p}, \\ g_n &= g_{bs} + g_{bp} + g_{bd} + g_{p}. \end{aligned} \tag{4.2.8}$$

Thus, this is consistent with the model developed in [130] for the two component case. With the detailed transport equations, we define the velocity for the bacteria, EPS, and solvent, respectively, as follows:

$$\begin{aligned} \mathbf{v}_b &= \mathbf{v} - \tfrac{\lambda_{bs}\phi_{bs}\nabla\mu_{bs}+\lambda_{bp}\phi_{bp}\nabla\mu_{bp}+\lambda_{bd}\phi_{bd}\nabla\mu_{bd}}{\phi_b}, \text{if} \quad \phi_b \neq 0, \\ \mathbf{v}_p &= \mathbf{v} - \lambda_p\phi_p\nabla\mu_p, \\ \mathbf{v}_s &= \tfrac{1}{\phi_s}(\mathbf{v} - \mathbf{v}_b\phi_b - \mathbf{v}_p\phi_p). \end{aligned} \tag{4.2.9}$$

Here, we assume the bacteria, regardless whether they are live or dead, persisters or susceptible cells, and EPS mix with the solvent due to the osmotic pressure equally. In other word, in this simplified model, the motility of each biomass component is assumed the same, although the model can be systematically modified for cases of different motilities as we did in our previous work if necessary [64].

For reactive kinetics, we assume both susceptible bacteria and persisters can proliferate following a logistic model with the growth rate regulated by the concentration of a regulatory protein [4], antimicrobial agents [11] and nutrient, whose concentrations are denoted by Q, A and C respectively. The susceptible and the persister cells can be converted into each other [3]. The rate of conversion from the susceptible cell to the persister is denoted as b_{sp} and the inverse conversion rate is denoted as b_{ps}. The conversion rate is usually nonlinear, and highly correlated with the existence of antimicrobial agents and availability of nutrient supply. We choose them as constants for simplicity in this study. In addition, we denote the natural death rate for the susceptible bacteria by r_{bs}. The antimicrobial agent kills susceptible and persister cells at different rates, which are denoted as c_3, c_{12}, respectively. The killing rate for persisters is presumably very low [48] (which is the reason why they are named persisters). Summarizing the mechanisms assumed above, we propose the reactive terms for susceptible bacteria and persisters as follows,

$$\begin{aligned} g_{bs} &= c_2 \tfrac{Q^2}{k_Q^2+Q^2} \tfrac{k_{12}^2}{A^2+k_{12}^2} \tfrac{C}{C+k_2} (1 - \tfrac{\phi_{bs}}{S_{\max}}) \phi_{bs} \\ &\quad - b_{sp}\phi_{bs} + b_{ps}\phi_{bp} - r_{bs}\phi_{bs} - \tfrac{c_3 A}{A+k_3}\phi_{bs}, \\ g_{bp} &= c_4 \tfrac{Q^2}{k_Q^2+Q^2} \tfrac{k_{12}^2}{A^2+k_{12}^2} \tfrac{C}{C+k_2} (1 - \tfrac{\phi_{bp}}{P_{\max}}) \phi_{bp} + b_{sp}\phi_{bs} - b_{ps}\phi_{bp} - \tfrac{c_{12} A}{A+k_3}\phi_{bp}, \end{aligned} \qquad (4.2.10)$$

where S_{max} and P_{max} are the carrying capacity for the susceptible and persister cells, respectively, c_2, c_4, k_{12}, k_3, k_Q are model parameters. The regulatory protein (Q), which we call it the growth factor or functional molecule, is a proxy for an ensemble of regulatory proteins that regulates the growth of live bacteria. Its contribution to the growth rate of bacteria is given by a Hill model. The antimicrobial agent clearly reduces the bacterial growth rate. In this model, we assume that the limiting effect is given by a factor inversely proportional to the square of its concentration. This reflects the switching effects when the concentration reaches a certain threshold, where power two controls the steepness of the switch curve. This choice is made based on our numerical fitting in [100]. The contribution of nutrient to the growth is given by a monod model that we have employed in our previous work and in many others' work as well.

The dead bacterial reactive rate is governed by the following reaction equation:

$$g_{bd} = \left(r_{bs} + \frac{c_3 A}{A + k_3} \right) \phi_{bs} + \frac{c_{12} A}{A + k_3} \phi_{bp} - \frac{r_{dp} k_{13}}{k_{13} + A} \phi_{bd}, \qquad (4.2.11)$$

where, on the right hand side, the first two terms are the growth terms due to the death of susceptible and persister cells, respectively, and the last term represents the breaking down or dissolution of dead bacteria into EPS and solvent components due to cell lysis [5]. Here r_{dp} is the maximum dissolution rate of dead bacteria, and k_3, k_{13} are two half salutation rates. The dissolution rate is a decreasing function of the concentration of the antimicrobial agent. This reflects that during antimicrobial treatment, as the metabolism of live cell decreases due to the existence of antimicrobial agents, cell lysis is compressed.

For the EPS production, we consider that live bacteria produce EPS with a growth rate affected by the concentration of nutrient and quorum-sensing molecules [116, 112, 71]. The mechanism is effectively modeled by a Hill type kinetic equation. In addition, we require that EPS concentration would not exceed a threashold. The dissolved dead bacteria would attached to EPS meshwork, which contributes to the second term in the following reactive equation. The reactive equation is thus proposed as follows:

$$g_p = c_5(\phi_{bs} + \phi_{bp}) \frac{C}{C + k_2} \frac{H^2}{H^2 + k_9^2} (1 - \frac{\phi_p}{E_{\max}}) + \frac{r_{dp} k_{13}}{k_{13} + A} \phi_{bd}. \tag{4.2.12}$$

Here the first part is the gain of EPS due to the live bacteria and the second part is the gain from the dead bacterial conversion; c_5 is the maximum EPS production rate due to live bacteria, k_2, k_9 are two half salutation constants and E_{max} is the carrying capacity for the EPS in the biofilm.

Transport equations for functional components

In addition to the biomass and effective solvent, there are functional components whose molecules are so small that their mass is negligible compared to the other biomass components. However, their chemical and biological effects are retained in the model. Thus, instead of tracking their volume fractions, we account for their concentrations instead. These molecules are nutrient, quorum sensing molecules, antimicrobial agents, as well as the functional protein or the growth factor, whose concentration are denoted as C, H, A and Q, respectively.

In our model formulation, the nutrient (C) is assumed to be convected with solvent. Its governing equation is given by a convection-diffusion-reaction equation with varying diffusion coefficient, i.e.,

$$\frac{\partial(\phi_s C)}{\partial t} + \nabla \cdot (\mathbf{v} \phi_s C) = \nabla \cdot (D_c \phi_s \nabla C) - c_7(\phi_{bs} + \phi_{bp} + \phi_{bd}) \frac{C}{C + k_2}, \tag{4.2.13}$$

where D_c is the diffusion rate and c_7 is the maximum nutrient consumption rate by bacteria. In particular, oxygen is normally regarded as the main component in the nutrient for the biofilm formation. Since the molecular mass of the oxygen is relatively small, it can penetrate EPS and the membrane of cells equally. Therefore, the diffusion coefficient of oxygen in biofilms is assumed a decreasing function of ϕ_n as follows,

$$D_c = D_{c0}\frac{2(1-\phi_n)}{2+\phi_n}, \tag{4.2.14}$$

where D_{c0} is the diffusion rate of nutrient in pure solvent. This diffusion coefficient accounts for the barrier effect of the biomass to the diffusion of small molecular substances.

Similar to nutrient, the antimicrobial agent is also treated as a phantom material whose mass is neglected while the chemical effect is retained. The transport equation for antimicrobial agents is proposed as follows

$$\frac{\partial(\phi_s A)}{\partial t} + \nabla\cdot(A\mathbf{v}\phi_s) = \nabla\cdot(D_a\phi_s\nabla A) - c_8(\phi_{bs}+\phi_{bp})\frac{A}{k_8+A} - r_a A, \tag{4.2.15}$$

where D_a is the diffusion coefficient of antimicrobial agents, and c_8 is the decay rate due to drug consumption, k_8 is a half saturation constant, and r_a is the natural decay rate of the antimicrobial efficacy. In our experiment, the antimicrobial agent is CHX, which loses half of its efficacy in one week. Since antimicrobial molecules are bigger molecules compared to nutrient molecules. Biomass, such as the membrane of live bacteria and EPS, as well as dead cells, can prevent antimicrobial agents from penetrating deeper into the biofilm colony. Thus, its diffusion rate is approximated by the Hinson Model [39],

$$D_a = D_{a0}\frac{2(1-\phi_b)}{2+\phi_b}\frac{1}{\phi_s+\frac{\phi_p}{D_{pr}}}, \tag{4.2.16}$$

where D_{a0} is the diffusion rate of antimicrobial agents in pure solvent, and D_{pr} is a parameter adjusting the slow penetrating effects due to the presence of EPS.

For quorum sensing molecules, we propose that its growth depends on the concentration of susceptible bacteria and the growth factor, while, in the meantime, it saturates when reaches a maximum level. Besides, the existence of antimicrobial agents can accelerate its saturation. Thus, the transport equation for quorum sensing molecules (H) is given by

$$\frac{\partial(\phi_s H)}{\partial t} + \nabla \cdot (\mathbf{v}\phi_s H) = \nabla \cdot (\phi_s D_h \nabla H) + c_A \phi_{bs} \frac{Q^2}{k_Q^2 + Q^2}(1 - \frac{H}{h_0}), \qquad (4.2.17)$$

where D_h is the isotropic diffusion rate of QS molecules, c_A is the production rate of quorum sensing molecules due to bacteria, k_Q is the model parameter in the Hill model and h_0 is the carrying capacity for quorum sensing molecules. For quorum sensing molecules, we assume their growth is regulated by the growth factor Q in the form of a Hill model.

For the growth factor, the transport equation is proposed following a similar approach,

$$\frac{\partial(\phi_s Q)}{\partial t} + \nabla \cdot (\mathbf{v}\phi_s Q) = \nabla \cdot (\phi_s D_q \nabla Q) + c_q \phi_{bs}(1 - \frac{Q}{q_0}), \qquad (4.2.18)$$

where D_q is the isotropic diffusion rate, c_q is the maximum production rate for the growth factor and q_0 is its carrying capacity. We assume that the growth factor is mainly produced by the susceptible bacteria ϕ_{bs} since the persister bacteria are metabolic inactive in the biofilm.

Continuity and momentum equation for the fluid mixture

To close this system, the governing equation for the averaged velocity $\mathbf{v}$ is given. As an approximation, we assume it's solenoidal. Then the continuity and the momentum equation are given, respectively, by

$$\begin{aligned} &\rho(\partial_t \mathbf{v} + \mathbf{v} \cdot \nabla \mathbf{v}) = \nabla \cdot (\phi_b \tau_b + \phi_p \tau_p + \phi_s \tau_s) - \nabla p - \gamma_1 k_b T \nabla \cdot (\nabla \phi_n \otimes \nabla \phi_n), \\ &\nabla \cdot \mathbf{v} = 0. \end{aligned} \qquad (4.2.19)$$

where p is the hydrostatic pressure and τ_b, τ_p and τ_s are the stress tensor induced by the bacteria, EPS, and solvent in the biomass, respectively. The last term in the momentum equation is due to the spatial inhomogeneity of biomass distribution, derived from the variation principle [130].

In this paper, we are interested in hydrodynamics, especially related to the growth, of inhomogeneous biofilms, in which the dominating time scale is significantly larger than the relaxation time scale in the biomass, especially, EPS. We therefore model all components in the biomass as viscous fluids, i.e.,

$$\tau_b = 2\eta_b \mathbf{D}_n, \tau_p = 2\eta_p \mathbf{D}_p, \tau_s = 2\eta_s \mathbf{D}_s, \tag{4.2.20}$$

where η_b, η_p and η_s are the viscosity of the bacterial, EPS and effective solvent component in the biomass, respectively. Here, the rates of strain tensors are defined respectively by

$$\mathbf{D}_b = \frac{1}{2}\left(\nabla \mathbf{v}_b + \nabla \mathbf{v}_b^T\right), \quad \mathbf{D}_p = \frac{1}{2}\left(\nabla \mathbf{v}_p + \nabla \mathbf{v}_p^T\right), \quad \mathbf{D}_s = \frac{1}{2}\left(\nabla \mathbf{v}_s + \nabla \mathbf{v}_s^T\right), \tag{4.2.21}$$

where $\mathbf{v}_b$, $\mathbf{v}_p$ and $\mathbf{v}_s$ are the effective velocity for bacteria, EPS and solvent, respectively, as defined in equation (4.2.9).

We note that, in this model, the motility and viscosity of each bacterial component are assumed the same for simplicity although we can handle distinct viscosities and motilities for different biomass components easily should the effect be identified by experiments to be significant. In some cases, dead bacteria would be flushed out along with the flow, which contributes to the heterogeneous structure in the biofilm, but this depends on the choice of antimicrobial agents. In this study, we assume the antibiotics would not change the viscosity of dead bacteria too much, thus dead bacteria stay within the biofilm colony.

Boundary conditions

The boundary conditions are proposed depending on the physical situations we intend to simulate. In this paper, our main goal is to simulate biofilm dynamics in a culture dish. Thus, we propose a boxed domain

$$\Omega = [0, \quad L_x] \times [0, \quad L_y] \times [0, \quad L_z], \tag{4.2.22}$$

where L_x, L_y, L_z is the length in the x, y and z direction, respectively. In addition, we assume the boundary conditions in both x and z direction are periodic. In the y direction, no-flux boundary conditions for the biomass and functional molecules are imposed, that's,

$$\begin{aligned}
[P\mathbf{v}\phi_s - D_p\phi_s\nabla P]\cdot\mathbf{n}|_{y=0,L_y} &= 0, \quad P = C, H, A, Q, \\
\nabla\phi_i\cdot\mathbf{n}|_{y=0,L_y} &= 0, \quad i = bs, bp, bd, p, \\
(\mathbf{v}\phi_i - \lambda\phi_i\nabla\tfrac{\delta F}{\delta\phi_i})\cdot\mathbf{n}|_{y=0,L_y} &= 0, \quad i = bs, bp, bp, p.
\end{aligned} \tag{4.2.23}$$

In addition, we impose the non-slip boundary condition for the average velocity field $\mathbf{v}|_{y=0,L_y} = 0$. We also impose a nutrient feeding condition $c|_{y=L_y} = c^*$ in place of the zero-flux condition.

Nondimensionalization

Let t_0 denote the reference time scale and h_0 denote the length scale, the variables and parameters are nondimensionalized as follows,

$$\tilde{t} = \frac{t}{t_0}, \tilde{x} = \frac{x}{h}, \tilde{\mathbf{v}} = \frac{\mathbf{v}t_0}{h}, \tilde{\tau} = \frac{\tau t_0^2}{\rho_0 h^2}, \tilde{C} = \frac{C}{c_0}, \tilde{A} = \frac{A}{d_0}, \tilde{H} = \frac{H}{h_0}, \tilde{Q} = \frac{Q}{q_0}, \tag{4.2.24}$$

where c_0 h_0, d_0 and q_0 represent the characteristic substrate concentration of nutrient, quorum sensing molecules, antimicrobial agents and growth factor, respectively. Then, the resultant non-dimensionalized parameters are summarized as follows

$$\begin{gathered}
\Lambda = \tfrac{\lambda\rho_0}{t_0}, \quad \Gamma_1 = \tfrac{\gamma_1 kT t_0^2}{\rho_0 h^4}, \quad \Gamma_2 = \tfrac{\gamma_2 kT t_0^2}{\rho_0 h^2}, \tilde{\rho} = \phi_s\tfrac{\rho_s}{\rho_0} + \phi_b\tfrac{\rho_b}{\rho_0} + \phi_p\tfrac{\rho_p}{\rho_0}, \\
R_{e_s} = \tfrac{\rho_0 h^2}{\eta_s t_0}, \quad R_{e_b} = \tfrac{\rho_0 h^2}{\eta_b t_0}, \quad R_{e_p} = \tfrac{\rho_0 h^2}{\eta_p t_0}, \\
\tilde{c}_i = c_i t_0, \quad i = 2, 3, 4, 5, 12, \tilde{c}_7 = \tfrac{c_7 t_0}{c_0}, \quad \tilde{c}_8 = \tfrac{c_8 t_0}{A_0}, \tilde{c}_a = \tfrac{c_a t_0}{h_0}, c_q = \tfrac{c_q t_0}{q_0}, \\
\tilde{b}_{sp} = b_{sp} t_0, \quad \tilde{b}_{ps} = b_{ps} t_0, \quad \tilde{r}_{bs} = r_{bs} t_0, \quad \tilde{r}_{bp} = r_{bp} t_0, \tilde{r}_a = \tfrac{r_a t_0}{A_0}, \\
\tilde{k}_{11} = \tfrac{k_{11}}{H_0}, \quad \tilde{k}_{12} = \tfrac{k_{12}}{A_0}, \quad \tilde{k}_2 = \tfrac{k_2}{c_0}, \tilde{k}_3 = \tfrac{k_3}{A_0}.
\end{gathered} \tag{4.2.25}$$

For simplify, we drop the tilde symbol $(\tilde{\bullet})$ for the parameters. The governing equations with the non-dimensionalizsed parameters are given below

$$
\begin{aligned}
&\rho(\partial_t \mathbf{v} + \mathbf{v}\cdot\nabla\mathbf{v}) = \nabla\cdot(\phi_b\tau_b + \phi_p\tau_p + \phi_s\tau_s) - [\nabla p + \Gamma_1\nabla\cdot(\nabla\phi_n\otimes\nabla\phi_n)],\\
&\nabla\cdot\mathbf{v} = 0,\\
&\partial_t\phi_{bi} + \nabla\cdot(\phi_{bi}\mathbf{v}) = \nabla\cdot(\Lambda\phi_{bi}\nabla\mu_{bi}) + g_{bi}, \quad i = s,p,d,\\
&\partial_t\phi_p + \nabla\cdot(\phi_p\mathbf{v}) = \nabla\cdot(\Lambda\phi_p\nabla\mu_p) + g_p,\\
&\tfrac{\partial(\phi_s P)}{\partial t} + \nabla\cdot(\mathbf{v}\phi_s P) = \nabla\cdot(\phi_s D_P\nabla P) + g_P, \quad P = C,H,A,Q.
\end{aligned}
\tag{4.2.26}
$$

where

$$
\begin{aligned}
g_{bs} &= c_2\tfrac{Q^2}{k_Q^2+Q^2}\tfrac{k_{12}^2}{A^2+k_{12}^2}\tfrac{C}{C+k_2}(1-\tfrac{\phi_{bs}}{S_{\max}})\phi_{bs} - b_{sp}\phi_{bs} + b_{ps}\phi_{bp} - r_{bs}\phi_{bs} - \tfrac{c_3A}{A+k_3}\phi_{bs},\\
g_{bp} &= c_4\tfrac{Q^2}{k_Q^2+Q^2}\tfrac{k_{12}^2}{A^2+k_{12}^2}\tfrac{C}{C+k_2}(1-\tfrac{\phi_{bp}}{P_{\max}})\phi_{bp} + b_{sp}\phi_{bs} - b_{ps}\phi_{bp} - \tfrac{c_{12}A}{A+k_3}\phi_{bp},\\
g_{bd} &= \left(r_{bs} + c_3\tfrac{A}{A+k_3}\right)\phi_{bs} + \tfrac{c_{12}A}{A+k_3}\phi_{bp} - \tfrac{r_{dp}k_{13}}{k_{13}+A}\phi_{bd},\\
g_p &= c_5(\phi_{bs}+\phi_{bp})\tfrac{C}{C+k_2}\tfrac{H^2}{H^2+k_9^2}(1-\tfrac{\phi_p}{E_{\max}}) + \tfrac{r_{dp}k_{13}}{k_{13}+A}\phi_{bd},\\
g_C &= -c_7(\phi_{bs}+\phi_{bp})\tfrac{C}{C+k_2},\\
g_A &= -c_8(\phi_{bs}+\phi_{bp}+\phi_{bd})\tfrac{A}{k_8+A} - r_aA,\\
g_H &= c_A\tfrac{Q^2}{Q^2+k_Q^2}\phi_{bs}(1-H),\\
g_Q &= c_q\phi_{bs}(1-Q).
\end{aligned}
\tag{4.2.27}
$$

Overall, we have 14 coupled PDEs in the governing system of equations.

Numerical results and discussion

Parameters and model calibration against experiments

All dimensional parameters used in this paper are summarized in Table 4.1. Some parameters are chosen from published results in the literature, where the sources of references are cited; others are determined by fitting experimental data obtained by our experimental group [99]. In this paper, we use two characteristic time scales for t_0: (a). the growth time scale is set at $t_0 = 8.64\times10^4$ seconds (1 day) and (b). the time scale is set as $t_0 = 5$ seconds when simulating the antimicrobial treatment. In the following, all parameter values used in the numerical study are chosen from Table 4.1 unless noticed otherwise.

For a complex hydrodynamical model such as this, where many model parameters are employed to describe the reactive kinetics, a good way to calibrate the model parameters is by analyzing the reactive kinetics in a spatially homogeneous domain. The experiment used in this paper to benchmark the model is a study conducted on bacterial persistence to antimicrobial treatment in a multispecies biofilm at different ages [99, 100]. To make our model comparable with the experiments, we make two assumptions: (i). the biofilm thickness in the experiment is proportional to its volume fraction and (ii). the experimental data can be described by the reactive kinetic model where spatial transport is neglected. In the experiment detailed in [99], the multi-species biofilm samples were grown from plaque bacteria on collagen-coated hydroxyapatite discs in brain-heart infusion for time periods ranging from 2 days to 12 weeks. At each time period, ratios of bacteria killed by CHX for 1 min, 3 min or 10 min, as well as the control set, were measured, respectively. The experimental data that we use in model calibration are customarily obtained by averaging over a spatial domain in the samples. Therefore, they are suitable for the spatially homogeneous reactive kinetics in the model. The comparison of numerical results governed by reactive kinetics and the experimental data are shown in Figure 4.4, where model parameters not available in the literature are fitted manually. It shows that our model predictions agree quantitatively well with the experimental data collected [99]. The results show that mature biofilms are more resistant to CHX treatment than young biofilms under normal conditions.

The experimentally calibrated model predicts that low concentration of the growth factor leads to a small change in the killing ratio during the first two weeks, which verifies the hypothesis made for the model that the low concentration of growth factor can reduce the metabolism of young biofilms. However, when the concentration of the growth factor reaches a threshold, bacteria become active and effective reproduction in cells as well as EPS ensue. In biofilm colinies, EPS builds a meshwork to encapsulate the bacteria, some of which are anchored around the membrane of bacteria while others form threads in the network. In mature biofilms, the densely distributed EPS network can significantly slow down the penetration of antimicrobial agents deep into the biofilm colony, and thereby effectively protect the bacteria from antimicrobial treatment. This perhaps explains the apparent drop of killing ratio in the second and third week in the experiments. After the first three weeks, the structure of the biofilm becomes fairly stable due to the reduced nutrient supply and weakened metabolism within biofilms. As the result, the killing ratio keeps within a fairly stable range.

In the numerical investigation on the recovery of spatially heterogeneous biofilms after antimicrobial treatment, we choose three-week-old biofilms after for 1 min, 3 min and 10 min CHX treatment as initial conditions, respectively. We note that, in the model system (both experimental and theoretical), post antimicrobial effects are due to the residual antimicrobial agents left in the biofilm. The numerical results together with the experimental data [100] are shown in Figure 4.5, where bacteria within the biofilm can not be eradicated completely, even with a strong dose of antimicrobial agents for a quite long time. Therefore, biofilm growth can relapse after antimicrobial treatment ceases. This effect is interpreted as the existence of persister cells in the biofilm by the model.

The model calibration determines the parameters in the reactive kinetic component of the model. Our objective next is to use the hydrodynamic model developed to simulate dynamics of heterogeneous biofilm growth, recovery after antimicrobial treatment and biomass-drug interaction by coupling hydrodynamic transport. The ultimate goal, of course, is to use the model to make sensible predictions for biofilm dynamics.

3D numerical simulations of biofilm recovery after antimicrobial treatment

It has been known that morphological structures of biofilms affect the microbial activity and biofilm function. To conduct numerical studies with spatially heterogeneous experimental data as the initial input, we must first reconstruct the biofilm morphology from the experimentally acquired confocal laser scanning microscopy (CLSM) images. This requires us to map the image data to 3D values of our model variables. These converted 3D biofilm profiles are then used as initial conditions for our numerical investigations. Readers, who are interested in the image analysis of experimental biofilm data, please refer to Chapter 6 in [57].

Specifically, given an RGB CLSM image like the one in Figure 4.6(a), we use the method given in the Appendix to reconstruct the morphological structure of live bacteria and dead bacteria depicted in Figure 4.6(b) and Figure 4.6(c), respectively. In the CLSM images shown in Figure 4.7, the dead bacteria are stained red and the live ones green. At any given location, only the one with a larger volume fraction is shown. These images are obtained in one of our experiments to show the biofilm recovery process after antimicrobial treatment. These converted data will be used as initial conditions in our numerical simulations in the following.

Numerically simulated growth of heterogeneous biofilms

We now investigate biofilm growth dynamics with a focus on structural heterogeneity using one of the experimentally acquired image data as the initial state. We use the experiment data shown in Figure 4.7(b) and convert them into volume fractions of susceptible bacteria, persisters, and dead bacteria, respectively. In this simulation, we assume that the live bacteria consist of entirely susceptible bacteria initially, which is shown in Figure 4.8. In the simulation, a computational box/domain is assigned to include the biofilm and sufficient amount of ambient fluid matrix on top of the biofilm. The biofilm is assumed to grow on a solid substrate at the bottom and the lateral sides while nutrient is supplied through the top boundary of the computational box. Figure 4.8(a) depicts the initial distribution of the susceptible bacteria in its volume fraction.

At the initial stage, the bacteria undergo a lag phase, in which there are no significant cell reproduction activities. This is the phase where the bacteria are still in the process trying to adjust to the environment. We notice that the maximum volume fraction of the susceptible cells drops initially by comparing the volume fraction in Figure 4.8(a) with that in Figure 4.8(b). During this process, the growth factor is produced and accumulated. When the concentration of growth factor Q reaches a threshold, bacteria start to reproduce and so do quorum sensing molecules. Meanwhile, the conversion between various phenotypes (persister and susceptible bacteria) begins (shown in Figure 4.8(f),) in which some susceptible bacteria convert into persisters. As it is shown in Figure 4.8(g), EPS production is seen to increase as more quorum sensing molecules are added to the biofilm system; in the meantime, some dead bacteria begin to dissolve into EPS. At this stage, the biofilm is still not well-developed as both persisters and EPS are still low in their respective volume fractions. Later at $t = 70$, when the biofilm is well-developed, we observe that susceptible cells, persisters and EPS reach their respective environmental carrying capacities and the biofilm exhibits more heterogenous structures in space. By comparing Figure 4.8(o) with 4.8(c), we note that the more quorum sensing molecules are there, the higher is the EPS concentration, which confirms the regulating effect of QS on the EPS production.

Antimicrobial treatment of biofilms

Once biofilms are formed, antimicrobial agents are normally used as a chemical means to treat them. Here, antimicrobial treatment of biofilms in heterogeneous settings are numerically investigated using the multiphase hydrodynamic model. Figure 4.9 depicts the growth dynamics of a biofilm with the initial profile converted from CLSM images of a three week old biofilm undergoing antimicrobial treatment for 3 minutes. The characteristic time scale used in this study is $t_0 = 5$s. In these figures, if there exist both live and dead bacteria in a single pixel, we plot the one with a higher volume fraction. So, the bacterial type shown in the figure is the dominating phenotype. The bacterial distribution at a set of time slots is shown in Figure 4.9(a-e), where a disinfection process in a heterogeneous biofilm is undertaking. At the marker of 2.5 minutes ($t = 30$), shown in Figure 4.9(g), most of the susceptible bacteria are killed, while the volume fraction of persister does not change much. The distribution of dead bacteria at $t = 30$ is shown in Figure 4.9(i). At the end of the treatment, not only the bacterial distribution is highly heterogeneous, but also is the concentration of antimicrobial agents (shown in Figure 4.9 (f).) From this numerical simulation, we draw one conclusion that the residual concentration of antimicrobial agents correlates strongly with the population of persistent bacteria and EPS spatially (see Figure 4.9(h) and (f).) This is perhaps related to the slow penetration of antimicrobial agents in the biomass as well as the consumption of antimicrobial agents by persisters and EPS.

Biofilm recovery after antimicrobial treatment

From the experimental observation [100] as well as the theoretical study discussed above, antimicrobial treatment of biofilms once may not eradicate biofilms completely since some phenotype of bacteria, i.e. the persister, can still be alive after the treatment. Thus, once dosing of antimicrobial agents ceases, the residual antimicrobial agents may lead to a relapse of biofilm growth.

In the study reported in [100], the portion of viable bacteria in multi species biofilms after exposure to two preparations containing high concentrations of CHX using CLSM and scanning electron microscopy (SEM) are quantitatively measured over a period of time. In this paper, we use the 3D hydrodynamic model to predict the recovery of the multi-species biofilm with heterogeneous structure after antimicrobial treatment. A 3D numerical prediction of this recovery process is depicted in Figure 4.10. The initial profile of both live bacteria and dead bacteria are converted from CLSM images of a biofilm after 3-minute treatment with CHX. In the subfigures presented, plot the bacterial type with a higher volume fraction at any point in space. The simulation agrees qualitatively well with the experiment, as shown in Figure 4.7. The model prediction strongly supports the hypothesis that there exist persisters in the biofilm which then leads biofilm relapse. The persister keeps in a dominant state during the antimicrobial treatment since they are tolerant to the severe environment when the concentration of antimicrobial agents is high. However, when the concentration of CHX drops below a threshold such that it is no longer fatal to the bacteria any more, the persister becomes metabolic-active and begins to convert back into the susceptible cell to resume the cell reproduction. Figure 4.10 shows that bacteria grow in a relative slow process initially and eventually live bacteria take over the entire domain leading to biofilm relapse (shown in Figure 4.10(e, f)). This simulation documents the recovery process of a heterogeneous biofilm after CHX treatment.

Strategies for disinfecting biofilms

As observed in the experiment [99] as well as verified through our calibrated model prediction [100], younger biofilms are easier to be treated than the mature ones. In order to investigate the underlying mechanism, we conduct a series of 3D numerical investigations on antimicrobial treatment of biofilms of different ages. One typical comparative study is summarized in Figure 4.11, where 1-day old, 7-day old and 35-day old biofilms are treated by antimicrobial agents for 3 minutes, respectively. The initial biofilm profiles are taken from simulations in Figure 4.8 at time $t = 1, 7, 35$ respectively. The remaining biomass right after the treatment is plotted in Figure 4.11 for the three biofilm samples, respectively. As shown in Figure 4.11(a-d), bacteria in the 1-day old biofilm is eradicated completely, i.e. no live bacteria after the 3-min treatment is observed, whereas some live bacteria are still observed in the older biofilms (the 7-day old and the 35-day old one) after the treatment (shown in Figure 4.11(e,f,i,j), respectively.) Interestingly, the susceptible bacteria in 7-day old biofilm are nearly eradicated as depicted in Figure 4.11(e) while there still exist susceptible bacteria in the 35-day old biofilm after the 3-min treatment. This is apparently due to the protective nature of EPS in the older biofilm. With a thicker layer of EPS in the 35-day old biofilm than in the 7-day old one, antimicrobial agents diffuse much less effectively into the 35-day old biofilm than into the 7-day old one.

Therefore, it suggests that earlier treatment of a biofilm before it becomes mature is much more effective in eradicating the bacteria in the biofilm than a late treatment. In addition, the choice of antimicrobial agents for treating biofilms should be based on the age of the biofilm. For young biofilms, antimicrobial agents that can make the growth factor (necessary enzyme or extra cellular DNA) ineffective could be more effective since it can suppress the growth of biofilms by trapping it in the lag phase, where, according to [48], the conversion between the susceptible and the persister cells is slow. However, once the biofilm becomes mature, antimicrobial agents that can penetrate EPS protection layers better would have a better disinfecting effect.

Conclusion

We have developed a multiphase hydrodynamic model for fluid-structure interaction in biofilms to include interactions among various biomass components, quorum sensing molecules and growth factors, as well as the structural heterogeneity using a phase field formulation [130, 131, 114, 113, 64, 65]. A full 3D numerical solver based on the hydrodynamic theory is developed and implemented on GPUs for simulating biofilm hydrodynamics in a boxed geometry. This model is calibrated by a set of related experiments on multispecies biofilms [99, 100].

The mechanisms behind biofilm growth and antimicrobial persistence are investigated theoretically. The model assumes the existence of persisters in biofilms, which is validated by the favorable comparison with the experiment. Through numerical studies, we confirm that EPS prevents antimicrobial agents from penetrating into the biofilm, which makes mature biofilms harder to be treated effectively by antimicrobial agents when compared with young biofilms. In addition, our model shows that quorum sensing plays an important role in the biofilm formation and enhancing antimicrobial persistence in mature biofilms. The biofilm recovery process after antimicrobial treatment is analyzed. The model predicts that treating biofilms at an earlier age is much more effective in preventing biofilm relapse than at an older age. Consequently, when the biofilm has grown older, antimicrobial treatment would not be effective and biofilm could recover several weeks after the antimicrobial treatment.

Feeded with initial conditions from CLSM images of biofilm samples, our 3D hydrodynamic model can predict the spatial-temporal structure qualitatively well. By taking the available CLSM data, we have investigated the biofilm growth dynamics during and after the disinfection process. Given the spacial-temporal distribution of biomass and functional molecules measured from CLSM data, our 3D biofilm solver can be used to predict the future course of biofilm re-development. For future research, we will further investigate the roughness, thickness, as well as the surface area of biofilm colonies through a combination of CLSM data and our 3D hydrodynamic model prediction. Thus, this 3D predictive tool developed here provides a powerful framework for further investigation of biofilm dynamics and the impact of functional molecules as well as antimicrobial agents.

Table 4.1: Values of dimentional parameters.

Symbol	Description	value	Unit	Reference
h	Characteristic length scale	1×10^{-3}	m	[130]
t_0	Characteristic time scale	5 or 8.64×10^4	s	
L_x, L_y, L_z	size of computational domain	$1 - 2 \times 10^{-3}$	m	[130]
T	Absolute Temperature	303	K	[130]
γ_1	Distortional energy coefficient	8×10^6	m^{-1}	[130]
γ_2	Mixing free energy coefficient	3×10^{17}	m^{-3}	[130]
χ	Flory Huggins parameter	0.55		[130]
λ	Mobility parameter	1×10^{-9}	$kg^{-1}m^3s$	
N	Generalized polymerization	1×10^3		[130]
ρ_n	Network density	1×10^3	$kg\ m^{-3}$	[131]
ρ_s	Solvent density	1×10^3	$kg\ m^{-3}$	[131]
η_p, η_b	Dynamic viscosity of biomass	10	$kg/(ms)$	
η_s	Dynamic viscosity of solvent	1.002×10^{-3}	$kg/(ms)$	[131]
D_c	Nutrient diffusion coefficient	2.3×10^{-9}	$m^{-2}s^{-1}$	[130]
D_a	AHL diffusion coefficient	2.3×10^{-10}	$m^{-2}s^{-1}$	[107]
D_d	Antimicrobial diffusion coefficient	2.3×10^{-9}	$m^{-2}s^{-1}$	[107]
c_0, h_0, d_0, q_0	characteristic molecule concentration	8.24×10^{-3}	$kg\ m^{-3}$	[100]
c_2	maximum growth rate for the susceptible	3×10^{-6}	s^{-1}	[100]
c_3	maximum death rate for the susceptible	6.5×10^{-2}	s^{-1}	[100]
c_4	maximum growth rate for the persister	3×10^{-7}	s^{-1}	[100]
c_{12}	maximum death rate for the persister	6×10^{-4}	s^{-1}	[100]
c_5	maximum EPS production rate	3.5×10^{-3}	s^{-1}	[100]
c_7, c_8	maximum nutrient or antimicrobial consumption rate	1.0×10^{-7}	s^{-1}	[100]
c_A	QS molecule production rate	6×10^{-7}	s^{-1}	[100]
c_q	growth factor production rate	1.0×10^{-5}	s^{-1}	[100]
r_a	decaying rate of effective antibiotics	1×10^{-6}	s^{-1}	[100]
b_{sp}, b_{ps}	conversion rate	1.5×10^{-7}	s^{-1}	[100]
r_{bs}	natural death rate of susceptible bacteria	2×10^{-7}	s^{-1}	[100]
r_{dp}	dead bacteria recycling rate into EPS	2.2×10^{-6}	s^{-1}	[100]
D_{pr}	Hinson constant	0.007		[100]
k_3	Monod constant	3.5×10^{-3}	$kg\ m^{-3}$	[100]
k_2, k_8	Monod constant	3.5×10^{-4}	$kg\ m^{-3}$	[100]
k_9	Monod constant	6.6×10^{-3}	$kg\ m^{-3}$	[100]
k_{12}	Monod constant	6.0×10^{-7}	$kg\ m^{-3}$	[100]
k_Q	Monod constant	2.5×10^{-3}		[100]
$S_{\max}$	carrying capacity for susceptible bacteria	0.08		[100]
$P_{\max}$	carrying capacity for the persisters	0.018		[100]
$E_{\max}$	carrying capacity for EPS	0.15		[100]

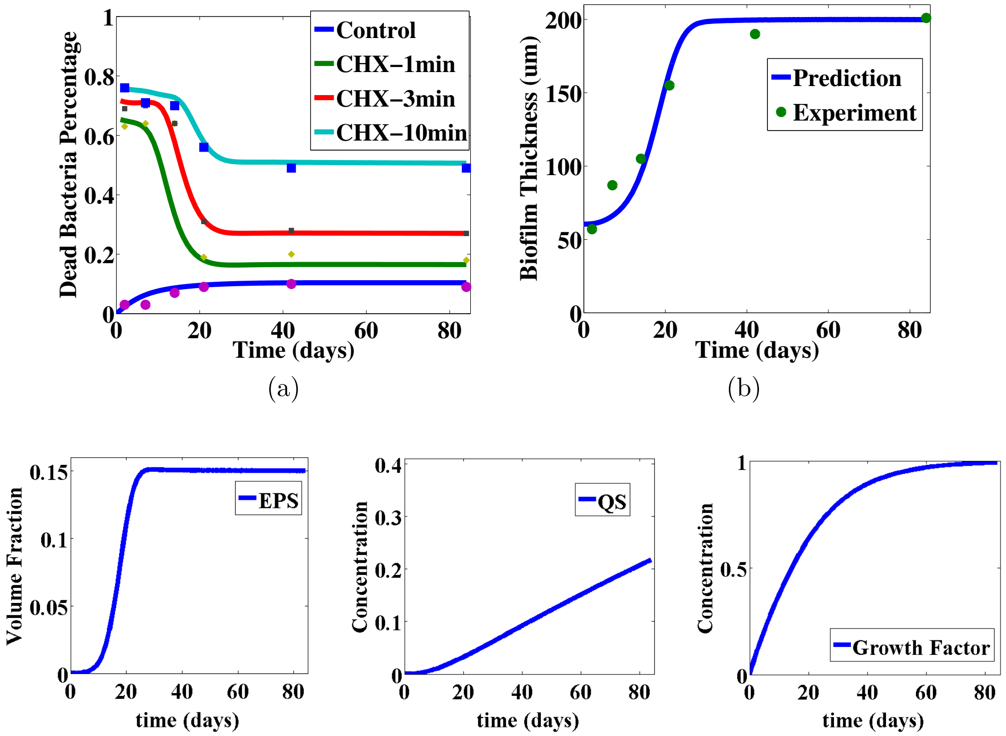

(a) (b)

(c) (d) (e)

Figure 4.4: Model prediction and comparison with experiments. (a) Percentage of dead bacterial cells at different times of biofilm recovery after being treated with CHX for 1, 3 and 10 minutes, respectively. The dots are the experimental data and the continuous curves are model predictions fitted to the experimental data. The bottom curve is the one corresponding to the natural death in a controlled experiment. All the experimental data are obtained from [28]. (b) The biofilm thickness in the controlled experiment and the prediction of the model. The initial values of volume fractions of various bacterial types and EPS, concentrations of nutrient, QS molecules, and growth factors are given by $(\phi_{bs}, \phi_{bp}, \phi_{bd}, \phi_p, C, A, Q, H) = (0.056, 0.024, 0, 0, 1.0, 0, 0, 0)$. (c) The model predicted EPS volume fraction in the controlled experiment. (d) The model predicted concentration of QS molecules in the controlled experiment. (e) The model predicted concentration of growth factors in the controlled experiment. In the controlled experiment, where biomass naturally grows, the biofilm thickness and the EPS volume fraction are increasing functions of time that saturate at their respective plateaus after 25 days of growth; concentrations of QS molecules and growth factors are monotonically increasing functions of time without showing an apparent saturation at the end of the experiment.

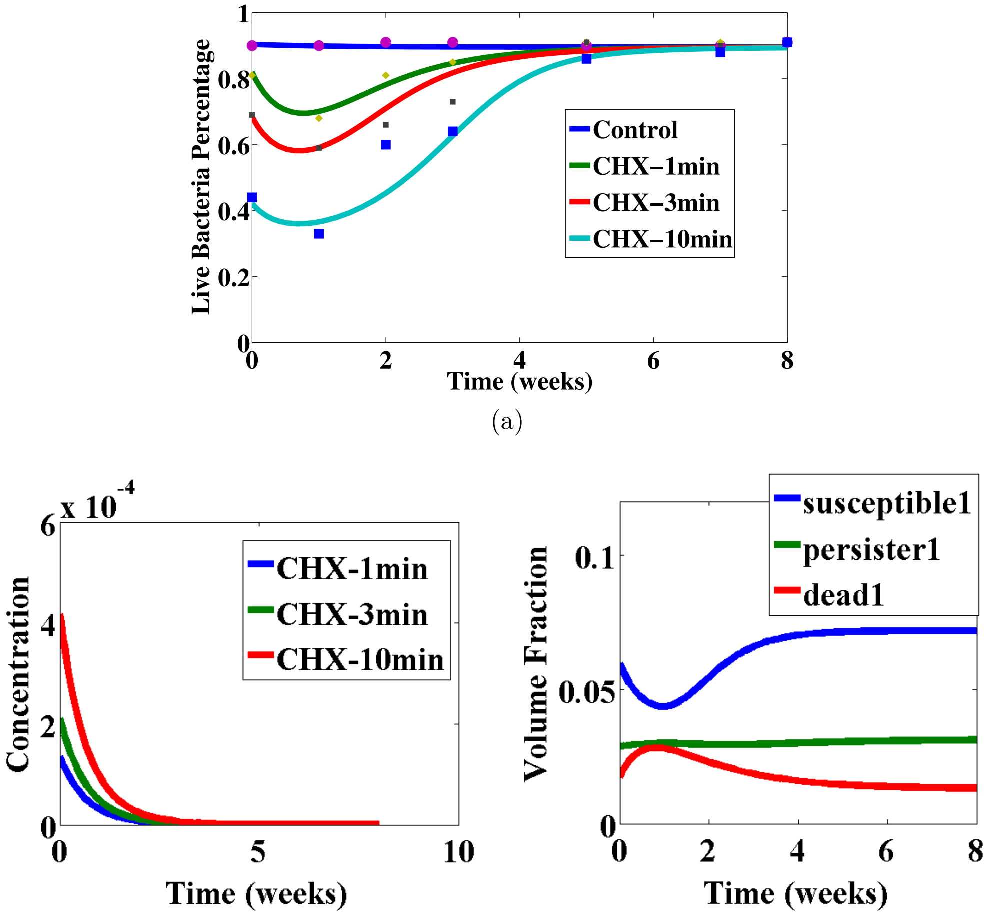

(a)

(b)

(c)

Figure 4.5: Model prediction of biofilm recovery after antimicrobial treatment. This figure shows live bacteria percentage over total bacteria, the concentration of antimicrobial agents in biofilms, and volume fractions of various bacteria types up to 8 weeks after the biofilm being treated with CHX. The initial profile is obtained from a 3-week old biofilm in Figure 4.4. The concentrations of residual CHX are obtained from the model prediction at $t = 21$ days with 1.67×10^{-4}, 2.1×10^{-4} and 3.75×10^{-4} corresponding to CHX treatment for 1, 3, 10 minutes, respectively. The concentration of nutrient is set at 1 initially. (a) The percentage of live bacterial cell volume in biofilms during recovery after treatment with CHX for 1, 3, 10 minutes and the control set (without treatment), respectively. The longer the biofilm is treated with CHX, the longer it takes for the residual bacterial cells to regain their populations. (b) The concentration of the residual CHX as a function of time after the biofilm is treated with CHX for 1, 3, 10 minutes, respectively. (c) The model predicted volume fraction of the dead, susceptible and persistent cells after the biofilm being treated with CHX for 1 minute.

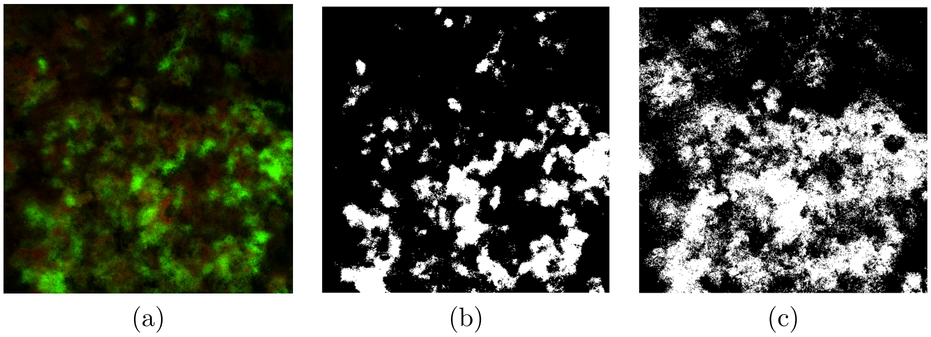
(a) (b) (c)

Figure 4.6: Reconstructing biofilm morphology through CLSM images. This figure shows the original CLSM image intensity of the dead and live bacteria in a biofilm and the ones that are reconstructed from the CLSM image. (a). The original CLSM image in which dead bacteria are stained as red and live ones green. The blank region in (b) and (c) is occupied by the live and dead bacteria, respectively. The dark region in (b) represents that the region free of live bacteria and the dark one in (c) denotes the region free of dead bacteria.

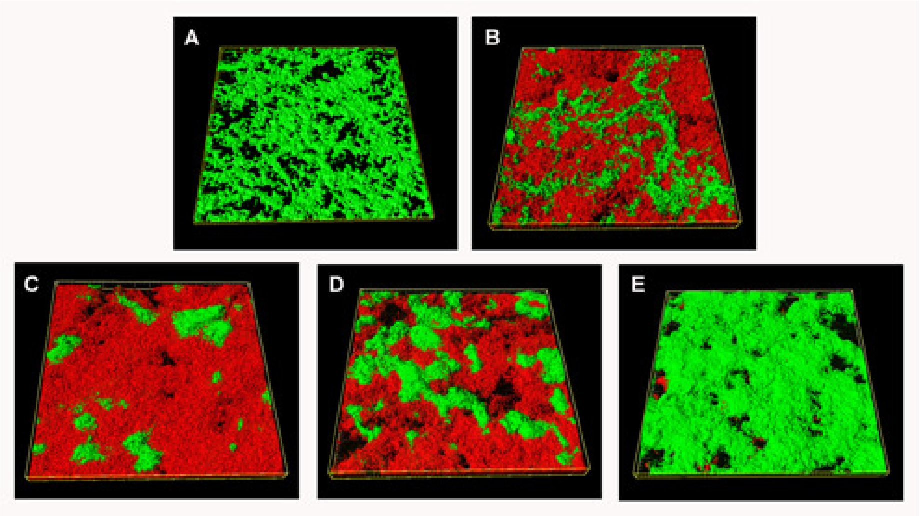

Figure 4.7: Biofilm recovery after 10-minute treatment with CHX-Plus. (a). A 3D image of CLSM scans of a 3-week-old biofilm prior to the treatment. (b). The 3D image after 10 minute treatment with CHX-Plus. (c). The biofilm is 1 week after the treatment. (d). The biofilm is three weeks after the treatment. (e). The biofilm is eight weeks after the treatment. The green fluorescence indicates viable live bacterial cells and the red one indicates dead cells.

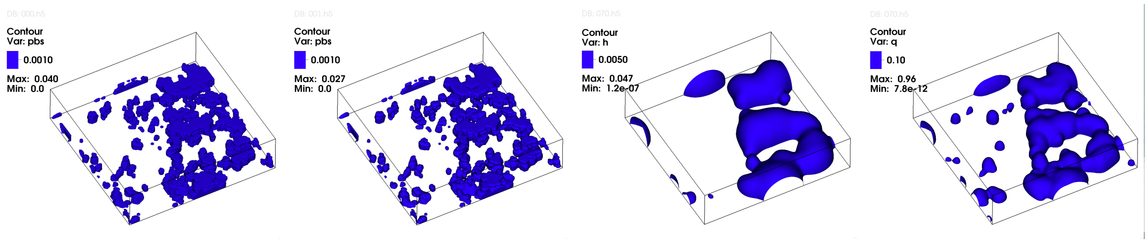

(a) ϕ_{bs} at $t = 0$ (b) ϕ_{bs} at $t = 1$ (c) H at $t = 70$ (d) Q at $t = 70$

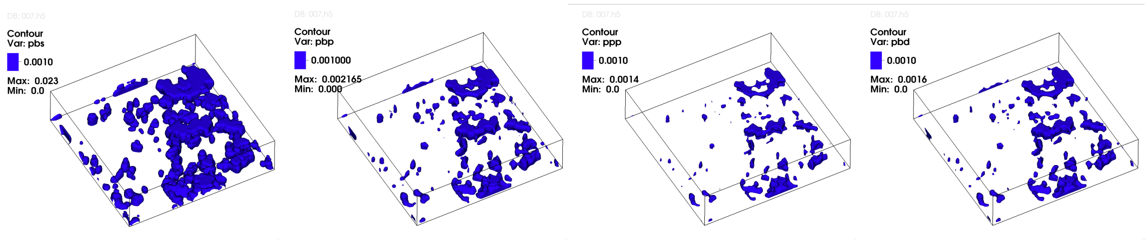

(e) ϕ_{bs} at $t = 7$ (f) ϕ_{bp} at $t = 7$ (g) ϕ_{p} at $t = 7$ (h) ϕ_{bd} at $t = 7$

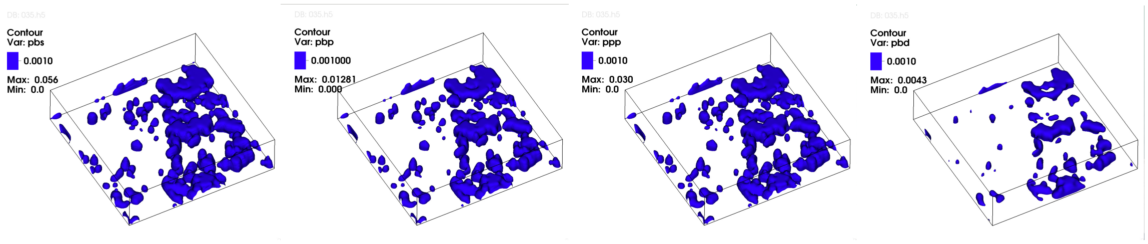

(i) ϕ_{bs} at $t = 35$ (j) ϕ_{bp} at $t = 35$ (k) ϕ_{p} at $t = 35$ (l) ϕ_{bd} at $t = 35$

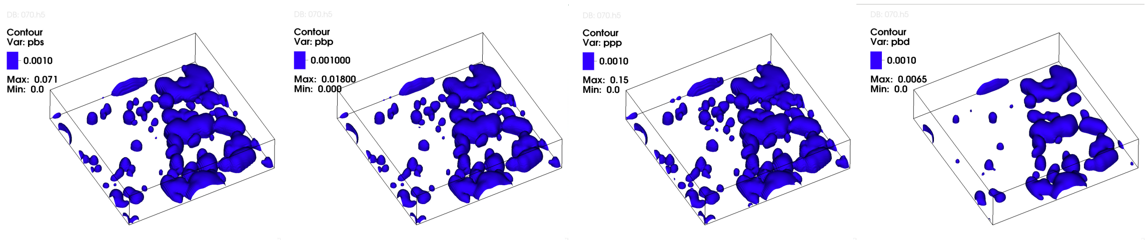

(m) ϕ_{bs} at $t = 70$ (n) ϕ_{bp} at $t = 70$ (o) ϕ_{p} at $t = 70$ (p) ϕ_{bd} at $t = 70$

Figure 4.8: Heterogeneous growth in a biofilm. This figure shows contour plot of the volume fraction of susceptible, persistent and dead bacteria and concentrations of EPS, growth factor, and QS molecules at selected time slot during the biofilm growth. The initial condition of the simulation is converted from a CLSM biofilm data set. (a) depicts the initial profile of susceptible bacteria, where the populations of persisters and dead bacteria are assumed zero initially. (b) depicts the profile of susceptible bacteria at $t = 1$. The distribution of quorum sensing molecules and the growth factor at $t = 70$ are shown in (c) and (d), respectively. The profile of biomass components: susceptible bacteria, persister bacteria, EPS and dead bacteria at different times are shown in (e-h) at $t = 7$, (i-l) at $t = 35$, (m-p) at $t = 70$. The characteristic time scale is set as $t_0 = 8.64 \times 10^4$s.

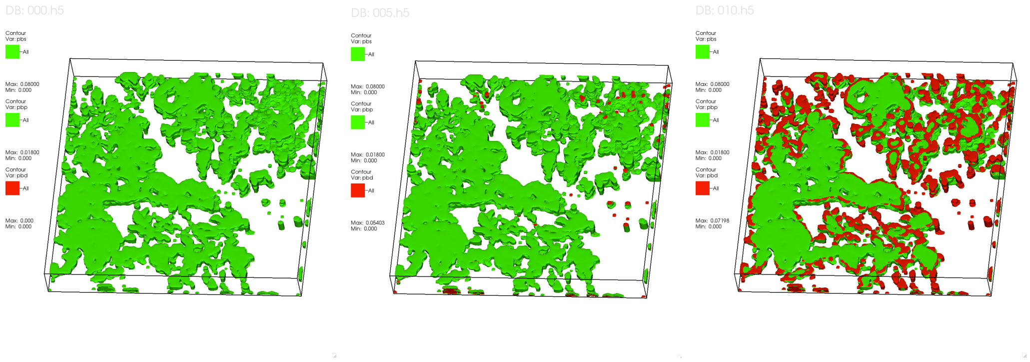

(a) Bacteria at $t = 0$ (b) Bacteria at $t = 5$ (c) Bacteria at $t = 10$

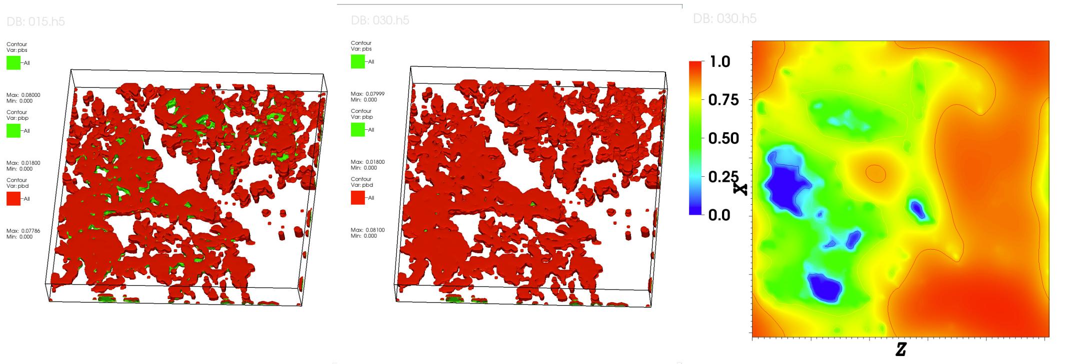

(d) Bacteria at $t = 15$ (e) Bacteria at $t = 30$ (f) 2D slice($y = 0.2$) of d at $t = 30$

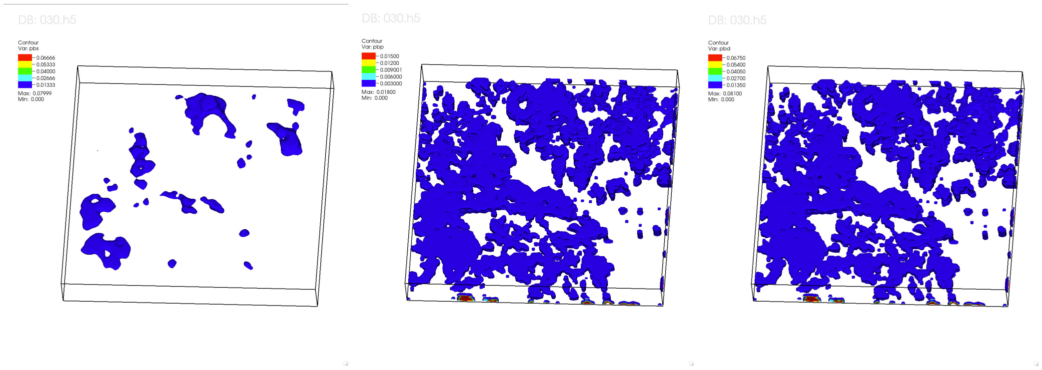

(g) ϕ_{bs} at $t = 30$ (h) ϕ_{bp} at $t = 30$ (i) ϕ_{bd} at $t = 30$

Figure 4.9: Various stages of antimicrobial treatment of a three-week old biofilm. The initial biofilm morphology is reconstructed from a three-week-old CLSM biofilm image. All components are assumed to have the same spatial distribution like the live one in the experimental data set, with the initial volume fractions $(\phi_{bs}, \phi_{bp}, \phi_{bd}, \phi_p) = (0.08, 0.018, 0, 0.08)$. (a-e) show bacterial profiles at different times, where we use green to represent the live bacteria and red the dead bacteria; (f) 2D slice ($y = 0.2$) of the concentration of antimicrobial agents at $t = 30$; (g-i) the volume fraction of each bacteria component at $t = 30$, respectively. The characteristic time scale is set as $t_0 = 5$s.

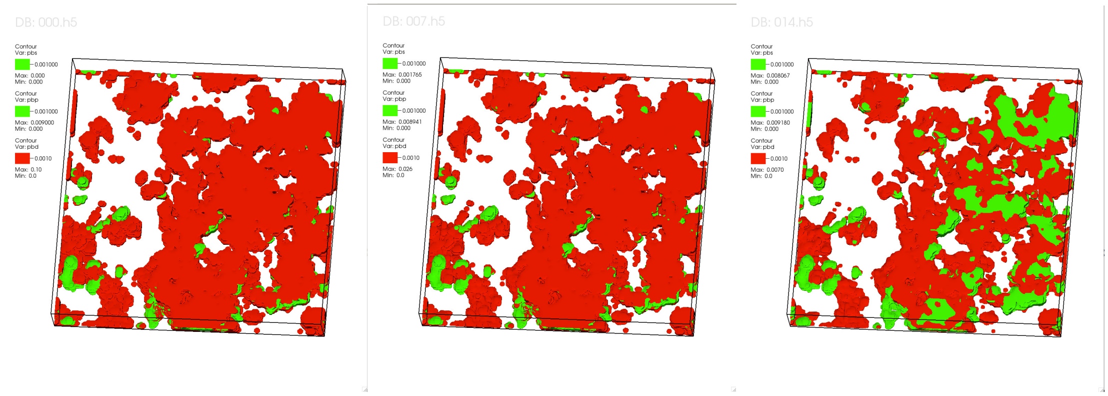

(a) Bacteria at $t = 0$ (b) Bacteria at $t = 7$ (c) Bacteria at $t = 14$

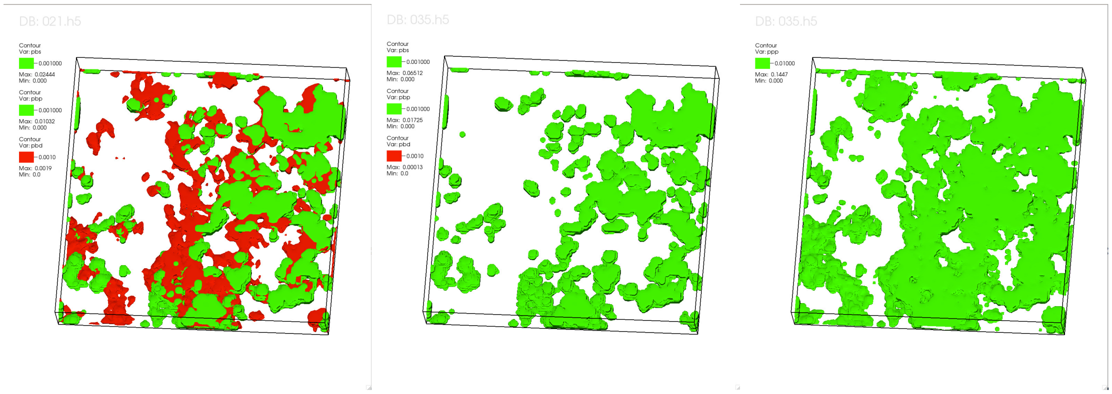

(d) Bacteria at $t = 21$ (e) Bacteria at $t = 35$ (f) EPS at $t = 35$

Figure 4.10: Biofilm recovery after antimicrobial treatment. This shows that the survival bacteria of a biofilm treated by antimicrobial agents regrow into a new biofilm. The initial biofilm morphology is reconstructed from the CLSM image of a 3 week old biofilm after 3 minute CHX treatment, where we assume EPS has the distribution proportional to that of the live bacteria and the initial volume fractions are given by $(\phi_{bs}, \phi_{bp}, \phi_{bd}, \phi_p) = (0, 0.01, 0.1, 0.1)$. The contours of all biomass component are plotted. (a)-(e) shows the distribution of bacteria at $t = 0, 7, 14, 21, 35$, respectively, where the red represents the dead bacteria and the green the total live bacteria, including both persister and susceptible cells. (f). depicts the contour of the EPS volume fraction at $t = 35$. The characteristic time scale is set as $t_0 = 8.64 \times 10^4$s.

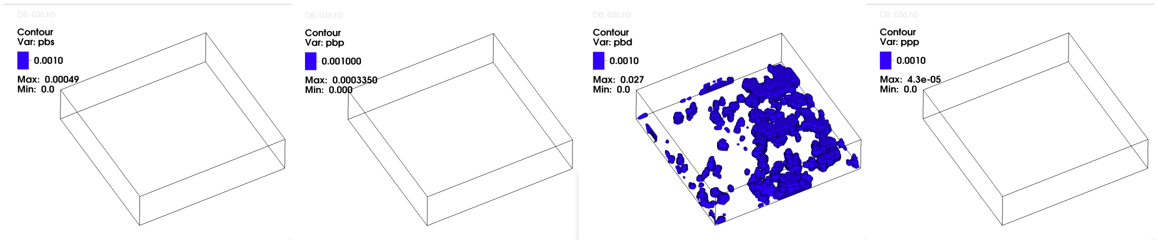

(a) ϕ_{bs} at $t = 36$ (b) ϕ_{bp} at $t = 36$ (c) ϕ_{bd} at $t = 36$ (d) ϕ_p at $t = 36$

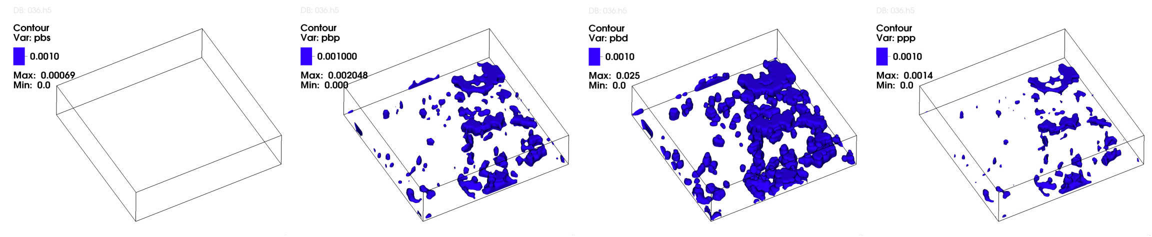

(e) ϕ_{bs} at $t = 36$ (f) ϕ_{bp} at $t = 36$ (g) ϕ_{bd} at $t = 36$ (h) ϕ_p at $t = 36$

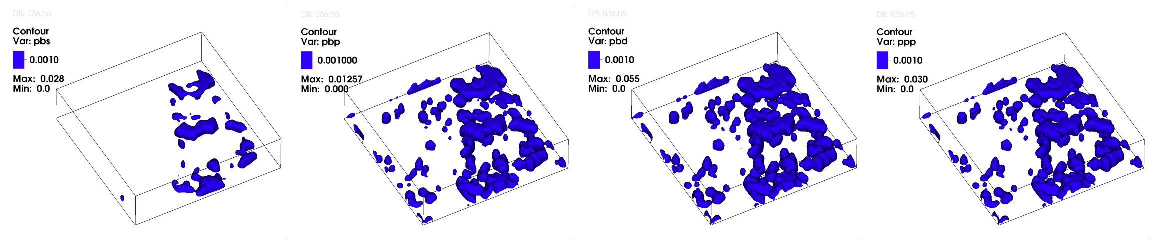

(i) ϕ_{bs} at $t = 36$ (j) ϕ_{bp} at $t = 36$ (k) ϕ_{bd} at $t = 36$ (l) ϕ_p at $t = 36$

Figure 4.11: Antimicrobial treatment of biofilms at different ages. This simulation shows that an older biofilm is more persistent to antimicrobial agents than younger ones by comparing the remaining components of 1, 7 and 35 day old biofilms at the end of a 3-minute treatment with antimicrobial agents. The phenomenon can be explained by the existence of the persister and EPS network. The initial biofilm profiles are taken from Figure 4.8 at time $1, 7, 35$ days, respectively. The contour of each biomass component at the end of 3-minute treatment by CHX is shown for the 1 day old biofilm (a-d), the 7 day old biofilm (e-h), the 35 day old biofilm (i-l), respectively. The characteristic time scale is set as $t_0 = 5$s.

CHAPTER 5

MATHEMATICAL MODELING AND SIMULATIONS OF EUKARYOTIC CELL MORPHOLOGY AND MITOTIC DYNAMICS

In previous chapter, we have proposed hydrodynamic models to study biofilms, which are micro-organism of bacteria, the major type of prokaryotic cells. In this chapter, we switch our topic into eukaryotic cells. In particular, we focus on animal cells. First of all, we give a brief introduction on the biological background, and a overview of current mathematical models in the literature. Then we will propose several hydrodynamic models to investigate the dynamics of animal cell morphology and mitosis. Several qualitative patterns have been observed.

5.1 BACKGROUND ON CELL MORPHOLOGY AND MITOTIC DYNAMICS

When attached on a substrate, the cell usually exerts a flat morphology. Before mitosis (when a mother cell duplicates into two identical daughter cells), the cell would undergo a drastic shape change, from essentially flat to round in a process known as mitotic cell rounding (MCR). MCR has been proposed to facilitate organization within the mitotic cell and be necessary for the geometric requirements of division [104]. A typical experiment observation is shown in Figure 5.1, where we can observe a spreaded cell rounds up in a time series.

The mechanisms in the molecular level is still unclear. In [53], the authors have identified that moesin is activated and necessary to increase cortical rigidity and cell

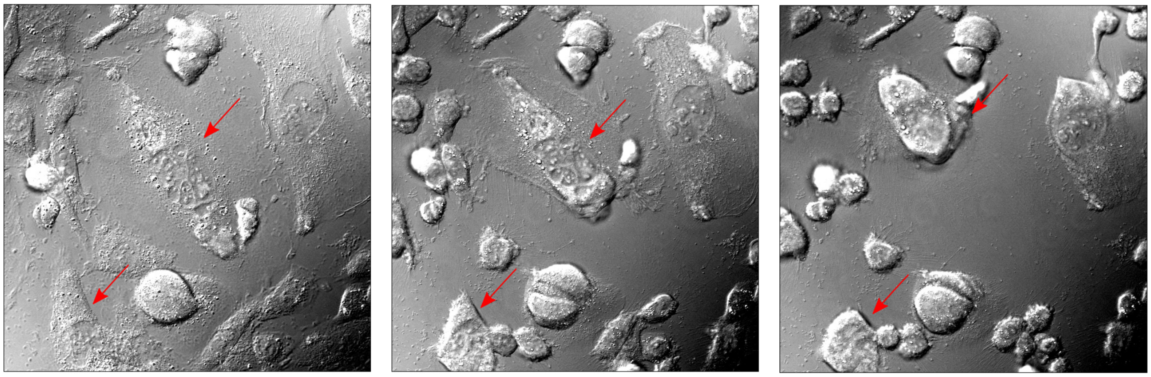

Figure 5.1: Mitotic cell rounding. This figure shows three time slots of cells on a substrate, indicating spreaded cell rounding up from a flat morphology(see red arrow). Images are courtesied from Maryna Kapustina from UNC.

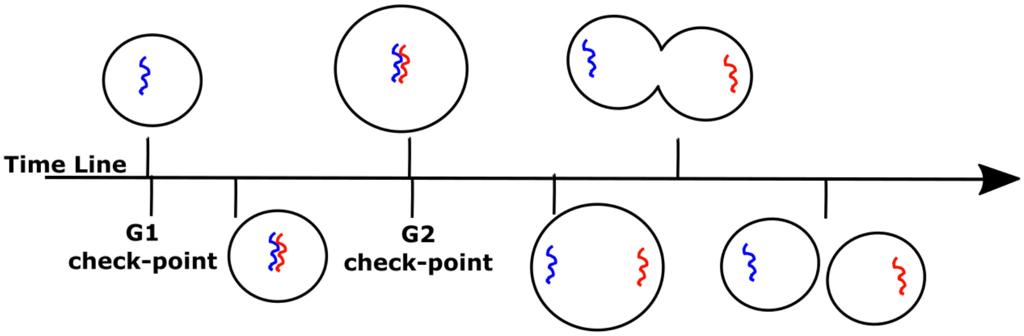

Figure 5.2: A time line for a cell cycle.

rounding. In [70], the authors proposed that the mitotic increase in RhoA activity leads to rearrangements of the cortical actin cytoskeleton that promote cortical rigidity, resulting in mitotic cell rounding. In [105], the author has proposed that its is the balance between globally outward osmotic pressure and locally inward actomyosin-cortex-dependent surface tension.

After the cells round up, some of them would enter a cell cycle, where a parent cell undergoes a sequence of intracellular transformations and eventually divides into two or more offspring cells. For eukaryotic cells, the cell proliferation process is called mitosis. The late stage of the cell mitotic process for eukaryotic cells, after the nucleus has been dissolved and chromosomes have been separated, is called cytokinesis. A cartoon showing the cell mitosis is given in Figure 5.2. Experimental observations have provide us with a basic phase diagram of cell mitosis. For eukaryotic cells, at the beginning of the cell mitotic process, the parent cell first duplicates its genetic substances and then forms a mitotic spindle consisting of microtubules [75]. Through a cascade of signaling processes [78], the actin and myosin molecules undergo a self-assembly process to remodel the cell cortex, an intracellular layer rich in actin-filaments and myosin molecules located immediately adjacent to the cell membrane [73]. In sync with the elongation of the mitotic spindle, more actin and myosin molecules ascend to a ring like region in a plane roughly orthogonal to the axis of the mitotic spindle to form the cytokinetic ring or contractile ring in the plane transverse to the axis of the spindle. The plane is called the cleavage plane or division plane [15]. As more actomyosin molecules are accumulated along the cytokinetic ring, a contracting force is generated which points inward toward the axis of the spindle [73]. The contracting force pushes the membrane inward to create what is known as the cleavage furrow on the membrane [87]. The contractile ring is a dynamic structure within the cortex, in which F-actin and myosin-II are continuously assembled and disassembled to maintain a roughly constant actomyosin molecular concentration as well as a contracting force to squeeze the cell along the contractile ring.

In figure 5.3, the distribution of myosin II of a purple urchin zygotes during its mitosis is shown. In Figure 5.4, the contractile ring made of F-actin is shown. In particular, the F-actin orientation on the contractile ring is stained.

Recall we mentioned after mitotic cell rounding and before cell mitosis, cells are usually in round shapes. However, if we zoom into a smaller length-scale, we can observe that the morphology of cell is not smooth at all, but with small bleb-like protrusions in smaller scale of 10-100 nm, compared with the cell radius 1-10 μm. as shown in Figure 5.5. Notice the cell rounding dynamics happens in a quick manner (approximate 30 seconds). There is little mass exchange between cytosol and extracellular substance, i.e. the total volume of the single cell is approximately conserved.

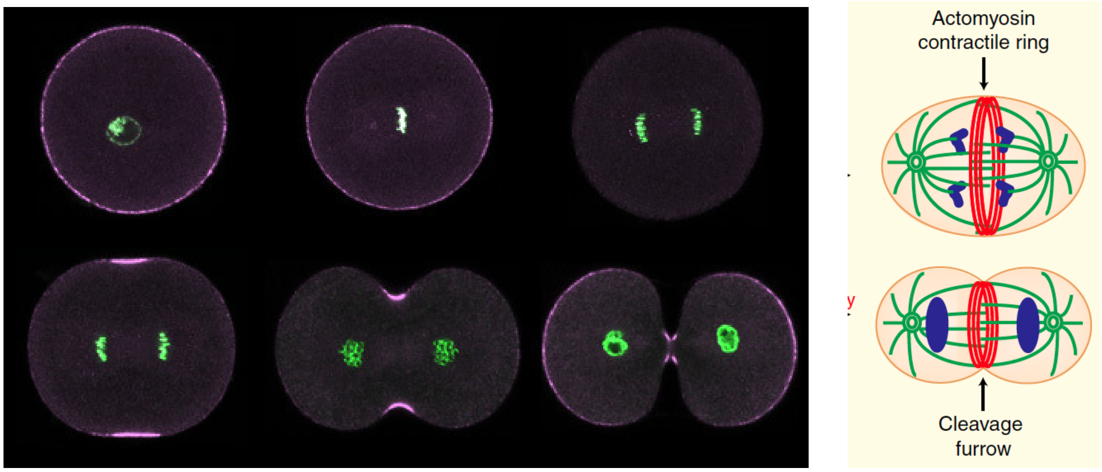

(a) Actomyosin Distribution during cytokinesis (b) Contractile Ring

Figure 5.3: Animal cell cytokinesis: (A) purple urchin zygotes during first mitosis, stained for DNA (green) and phosphorylated myosin II (magenta); (B) a cartoon of actomyosin contractile ring and cleavage furrow. Images of (A) is from http://php.med.unsw.edu.au/cellbiology/; Image of (B) is from [73].

However, as the rounded cell has less surface area than a flat one of the same volume, there is excess surface area of the rounded cell, which leads to the dynamics of bleb-like protrusions on cell membrane.

A review of existing mathematical models

In literature, there are some efforts [127, 108], though apparently, there is still a gap in-between the numerical simulations and experiment observations. In [38], the author has derived cell membrane model through a thermodynamical consistent approach. In particular, a heuristic derivation for the phase field approximation of the line energy and Gaussian bending energy is presented. Vesicle equilibrium states at the minimum energy has been studied thoroughly by Udo Seifert in the series of papers [91, 92] by studying either spontaneous curvature or bilayer-coupling models [43, 6]. In particular, a phase diagram of shape transformation has been given. In [66], the spontaneous tubulation of membranes induced by spontaneous curvature is discussed. The budding dynamics by a Monte Carlo simulation is studied in [52]. For

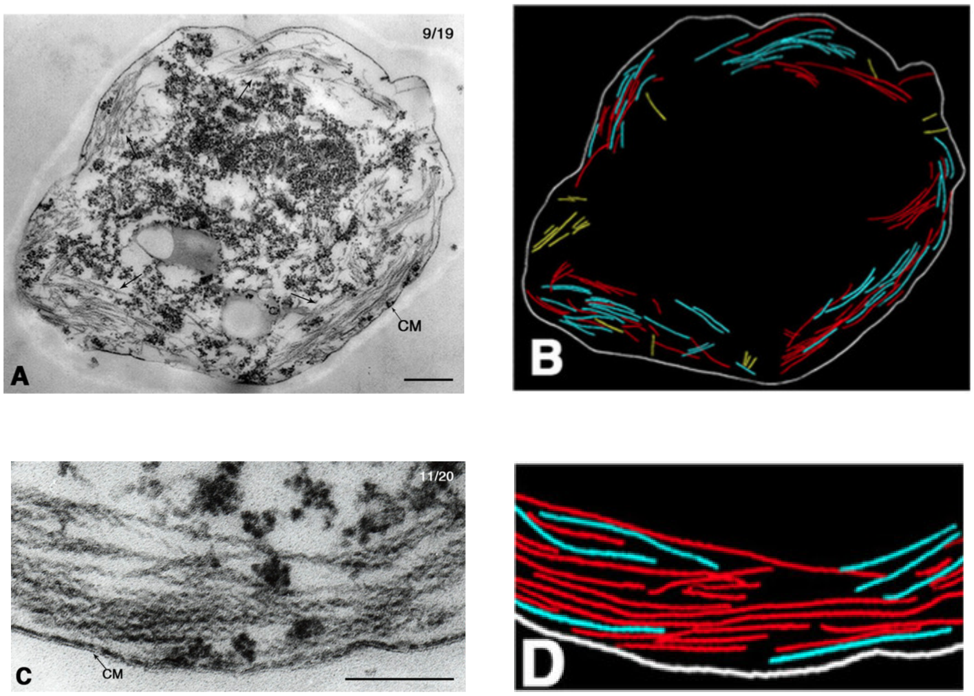

Figure 5.4: Arrangement of F-actin in the contractile ring. (A) an image of the contractile ring at late anaphase; (B)tracing of F-actin shown in A; (C) a magnififed image of (A); (D) a magnified image of (B). (Images are from [45])

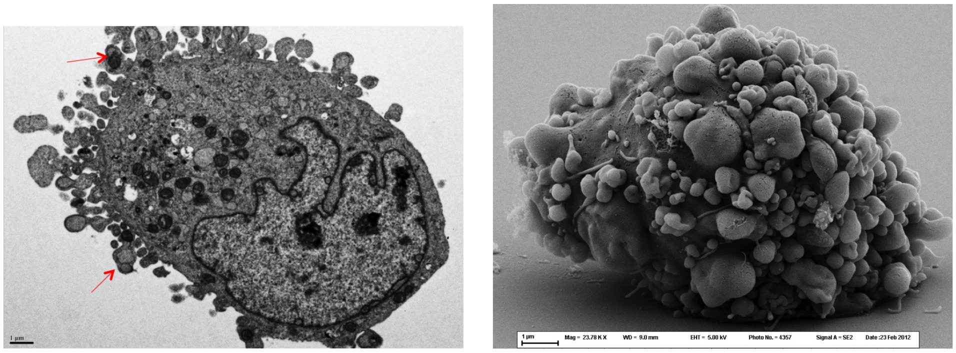

(a) BliP (b) BliP

Figure 5.5: Cell bleb-like protrusion. (A) folding of the membrane-cortex couple as visualized in TEM; (B) SEM of CHO cell after rounding. Experiment data is from Kenneth Jacobson's lab at UNC.

phase field modeling for cell membrane dynamics, Wang and Du [115] have proposed a two-component phase field model for vesicle membrane. In [69], the author have proposed a similar model, instead of having two components for membrane, they propose and solve the surface mass conservation equation explicitly.

5.2 MODELING THE EXCESS CELL MEMBRANE STORED IN A COMPLEX MORPHOLOGY OF BLEB-LIKE PROTRUSIONS

Mathematical model formation

In this section, we formulate a 3D phase field model for a cell immersed in a buffer. The model is formulated in 3 space dimensions (3D), but it also restricts to 2D for purposes of modeling a planar projection or cell cross-section. The phase field method is an alternative to sharp interface methods for composite materials with distinct components separated by a diffuse boundary (a thin layer) whose shape and evolution are part of the solution. For every pair of neighboring material components, a phase field variable is introduced that interpolates between components over a finite thickness layer, called a diffuse interface. In our problem, we have three phases (exterior buffer, cortex, interior cytosol) and two diffuse interfaces (lipid bilayer membrane between buffer and cortex, cortex-cytosol transition layer). Figure 1 is a 2D schematic of a 2D cell cross-section with individual components and diffuse interfaces labeled.

We begin with the introduction of phase variables ϕ_i, $i = 1, 2, 3$ that denote the volume fractions of phase 1 (the buffer), phase 2 (cortex) and phase 3 (interior cytosol), respectively. Clearly in any pure phase i, the respective $\phi_i = 1$, whereas in diffuse interfaces between phases i and j, $\phi_i + \phi_j = 1$, with $\phi_k = 0, k \neq i, j$, and everywhere the total volume fraction is 1. Thus in the external buffer, $\phi_1 = 1$; in the F-actin rich, cell cortical layer, $\phi_2 = 1$; and in the interior cytoplasm, $\phi_3 = 1$. (We do not explicitly model the nucleus within the cytoplasm for this paper since we are primarily concerned with a stationary rounded morphology.) The phase boundaries are: the lipid bilayer membrane that separates the buffer and cortical layer, where $0 < \phi_1, \phi_2 < 1$; and, the transition layer between the cortex and interior cytosol where $0 < \phi_2, \phi_3 < 1$. For graphical purposes and for matching 2D TEM and 3D

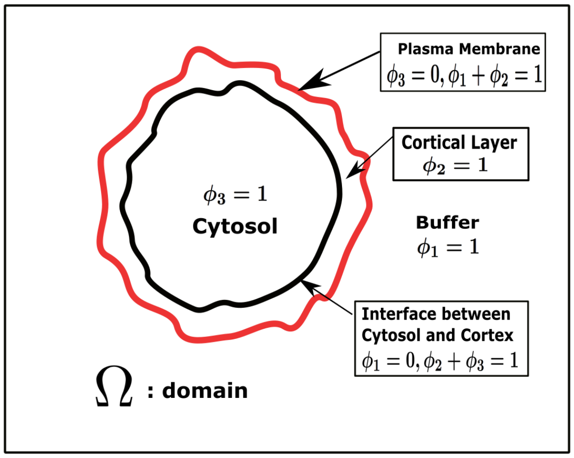

Figure 5.6: Schematic for the cell-buffer phase field formulation: ϕ_1, ϕ_2, ϕ_3 represent volume fractions of the buffer, cortex and cytosol, respectively. The computational domain is denoted as Ω. The cell lipid bilayer membrane is defined by the level set $\phi_1 = \frac{1}{2}$ and the interface between the cytosol and the cortex is defined by the level set $\phi_3 = \frac{1}{2}$.

SEM images, the cell membrane surface is defined by $\phi_1 = \phi_2 = 1/2$, while the cortex-cytosol surface is defined by $\phi_2 = \phi_3 = 1/2$. We do not allow all three phases to come into contact for the purposes of this paper.

The buffer and interior cytosol are modeled as viscous fluids with specified viscosities and the cortex is modeled as a nematic gel. The governing equations for the three phases and two diffuse interfaces are presented next. The phase field method is an energy-based variational theory, comprised of energy functionals for each phase and diffusive interface, from which energy minimization governs evolution from initial data.

Free energy

We denote the free energy of the cortex by $F_{\mathbf{p}}$, where the subscript $\mathbf{p}$ is the nematic director; the free energy for all interfacial tensions by F_S, where S denotes surface energies; and the free energy for the lipid bilayer membrane bending energy by F_B, where B denotes bending. The bilayer membrane and the F-actin cortex may be bound or tethered, modeled by an orientational anchoring condition that can be tuned between parallel and normal alignment of the cortex, and with an energy cost of membrane-cortex anchoring denoted by F_{anch}. The membrane surface area and the cell volume are assumed to be known from experimental measurements of the spread cell configuration and conserved in the transition from spread to rounded configuration as discussed in the experimental section. The phase transport equations for the phase variables in this paper are Cahn-Hilliard equations that ensure the conservation of the volume of each component including the cell volume [12]. Therefore, the cell volume is determined by the initial value in this model. To ensure conservation of membrane surface area, we introduce an energy, F_{SA}, that penalizes the departure from the known membrane surface area. Putting these contributions together, the total free energy is given by the sum:

$$F = F_S + F_B + F_{\mathbf{p}} + F_{anch} + F_{SA}. \tag{5.2.1}$$

We now describe these energy terms in more detail. The interfacial surface energy contributions are built into ϕ_1 and ϕ_2 at the buffer-cortex boundary (the lipid bilayer membrane) and into ϕ_2 and ϕ_3 at the cortex-cytosol phase boundary. Each contribution is modeled by a standard phase field approximation to the surface energy at the interface, consisting of an energy penalty for conformational entropy together with the Ginzburg-Landau double well potential whose two minima define the two adjacent phases, and finally an energy term that penalizes coexistence of the three phases:

$$F_S = \int_\Omega \sum_{i=1}^{3} 3\sqrt{2}\gamma_{is}\left(\frac{\varepsilon}{2}\|\nabla\phi_i\|^2 + \frac{1}{\varepsilon}\phi_i^2(1-\phi_i)^2\right) + \frac{\gamma_{123}}{2}\Pi_{i=1}^{3}\phi_i^2 d\mathbf{x}, \tag{5.2.2}$$

where k_B is the Boltzmann constant, T is the absolute temperature, γ_{1s} and γ_{2s} contribute the bilayer membrane surface tension while γ_{2s} and γ_{3s} contribute surface tension for the cortex-cytosol diffuse interface.

Since the membrane is represented by either $\phi_1 = \frac{1}{2}$ or $\phi_2 = \frac{1}{2}$ in the phase field formulation, the Helfrich bending elastic energy for the cell membrane is built into the buffer (ϕ_1) or cortex (ϕ_2) phase variable, arbitrarily chosen as ϕ_1 here, given by

$$F_B = \int_\Omega 3\sqrt{2}\gamma_{1b}\varepsilon \left(\nabla^2\phi_1 - \frac{2}{\varepsilon^2}\phi_1(\phi_1 - 1)(2\phi_1 - 1 - \frac{\varepsilon}{\sqrt{2}}C_1)\right)^2 d\mathbf{x}. \tag{5.2.3}$$

where γ_{1b} parametrizes the bending rigidity of the bilayer membrane. The function C_1 is the spontaneous curvature of the membrane, a key element of our model that warrants discussion. C_1 is a proxy for the concentration of membrane-cortex binding proteins. Domains rich in binding proteins bind the membrane to the cortex, inheriting the mean curvature of the cortex. Domains free of binding proteins allow the membrane to detach from the cortex and depending on the dimensions of the detached domain, invaginations and bleb-like protrusions (BLiPs) form. In the absence of detailed measurements of the regulatory binding protein species, we use either 2D micrographs of the membrane morphology or 3D reconstructions of the membrane morphology (see the next paragraph) to fit the spontaneous curvature function C_1. Note that the interplay between domains free of, versus rich in, the binding protein species dictate the membrane morphology, which in turn dictates the spontaneous curvature function C_1. We choose the level set $\phi_1 = 1/2$ to define and match the membrane morphology captured in 2D micrographs and reconstructed from 3D micrographs.

The elastic energy associated with the (apolar) nematic gel model of the filamentous actin cortex is described in terms of a direction $\mathbf{p}$ for the principal axis of orientation, while $\|p\|$ is allowed to vary between 0 for the isotropic phase and 1 for a perfectly aligned phase. $\mathbf{p}$ is called the nematic director and $\|\mathbf{p}\|$ is called the nematic order parameter. The elastic energy of the cortex is then given by a Frank-Oseen distortional energy together with a Landau-deGennes bulk free energy,

$$F_{\mathbf{p}} = \int_\Omega \frac{1}{2}\phi_2^2 \left(\frac{K}{2}\|\nabla\mathbf{p}\|^2 + \frac{h_2}{4}\|\mathbf{p}\|^4 - \frac{h_1}{2}\|\mathbf{p}\|^2\right) d\mathbf{x}. \tag{5.2.4}$$

where: the prefactor ϕ_2^2 restricts the nematic elastic energy to the cortex, K is the Frank elastic constant (we assume the bend, splay and twist constants are equal for this paper), controlling energy cost for orientational gradients within the actin-rich cortical network; and h_1, h_2 are model parameters that control whether the equilibrium phase of the cortex is nematic ($0 < \|\mathbf{p}\| \leq 1$) or isotropic ($\|\mathbf{p}\| = 0$). In a spatially homogeneous state, where $\nabla\mathbf{p}$ vanishes, the elastic energy for the cortex favors stable minima of the bulk energy function: $\frac{h_2}{4}\|\mathbf{p}\|^4 - \frac{h_1}{2}\|\mathbf{p}\|^2$. The stable minimizer of this function is given by the nematic state with order parameter $\|\mathbf{p}\| = \sqrt{\frac{h_1}{h_2}}$ when $h_1 > 0$ and by the isotropic state $\mathbf{p} = \mathbf{0}$, when $h_1 \leq 0$.

The anchoring energy of the nematic cortex with the cell membrane is given by

$$F_{anch} = \int_\Omega \frac{\alpha_1}{2}(\mathbf{p}\cdot\nabla\phi_1)^2 d\mathbf{x}, \tag{5.2.5}$$

where α_1 parametrizes the strength of the anchoring potential, and $\alpha_1 > 0$ promotes tangential anchoring while $\alpha_1 < 0$ promotes normal anchoring of the F-actin cortical network with the membrane.

The surface area s_0S^*, with S^* the surface area initially and s_0 the excess surface ratio, is enforced by an energy penalty for deviation of $S(t)$ (the interior of the $\phi_1 = 1/2$ level set). The energy penalty function is given by

$$F_{SA} \;=\; \frac{1}{2}\lambda_S(S(t) - s_0S^*)^2, \tag{5.2.6}$$

where λ_S weights this energy penalty and $S(t)$ is the surface area at time t calculated from the phase variable ϕ_1 by:

$$S(t) \;=\; \int_\Omega 3\sqrt{2}\left(\frac{\varepsilon}{2}\|\nabla\phi_1\|^2 + \frac{1}{\varepsilon}\phi_1^2(1-\phi_1)^2\right)d\mathbf{x}. \tag{5.2.7}$$

We note that this variational energy model accepts the measured target for S^*, and the membrane morphology images from micrographs are used to fit C_1 in 2D or membrane surface reconstructions in 3D, and then any initial guesses for S follow the energy minimization dynamics toward the target surface area, while C_1 guides the membrane morphology toward that of the experimental micrographs.

The full set of coupled model equations

By postulating the linear momentum balance and incompressibility of the material system, the governing system of equations is

$$\left\{\begin{array}{rcl} \rho(\partial_t \mathbf{v} + \mathbf{v}\cdot\nabla\mathbf{v}) & = & -\nabla p + \nabla\cdot\sigma, \\ \nabla\cdot\mathbf{v} & = & 0, \\ \partial_t\phi_i + \nabla\cdot(\mathbf{v}\phi_i) & = & \nabla\cdot\left(\lambda_i\nabla(\frac{\delta F}{\delta\phi_i} - \frac{\delta F}{\delta\phi_2})\right), \quad i = 1, 3. \\ \partial_t\mathbf{p} + \mathbf{v}\cdot\nabla\mathbf{p} - \mathbf{W}\cdot\mathbf{p} & = & \nu\mathbf{D}\cdot\mathbf{p} + \frac{1}{\lambda_p}\mathbf{h}, \end{array}\right. \tag{5.2.8}$$

where $\mathbf{h} = -\frac{\delta F}{\delta\mathbf{p}}$ is known as the molecular field in the liquid crystal community [34], which represents a torque generated by the Frank-Oseen elastic energy, $\frac{\delta F}{\delta\phi_i}$ is the chemical potential with respect to ϕ_i, σ is the total extra stress, $\mathbf{W}_{\alpha\beta} = \frac{1}{2}(\partial_\beta\mathbf{v}_\alpha - \partial_\alpha\mathbf{v}_\beta)$ is the vorticity tensor, $\mathbf{D}_{\alpha\beta} = \frac{1}{2}(\partial_\beta\mathbf{v}_\alpha + \partial_\alpha\mathbf{v}_\beta)$ is the rate of strain tensor, ν is a geometric parameter for the nematic gel, and λ_p is a rotational relaxation time for the nematic director $\mathbf{p}$. Here the total extra stress tensor consists of three parts:

$$\sigma = \sigma^r + \sigma^d + \sigma^e + \sigma^a, \tag{5.2.9}$$

where σ^r is the elastic stress corresponding to the motion of the nematic director $\mathbf{p}$, σ^d is the viscous stress associated to the solvent in the system, σ^e is the Ericksen stress, the stress associated to the elastic interfacial force due to molecular convection, and σ^a is the active stress. They are given specifically by the following:

$$\begin{array}{rcl} \sigma^r & = & -\frac{\nu}{2}(\mathbf{ph} + \mathbf{hp}) + \frac{1}{2}(\mathbf{ph} - \mathbf{hp}), \\ \sigma^d & = & 2\eta\mathbf{D}, \\ \sigma^e_{\alpha\beta} & = & (f - \sum_{i=1}^3 \phi_i \frac{\delta f}{\delta\phi_i})\delta_{\alpha\beta} - \sum_{i=1}^3 \frac{\partial f}{\partial(\partial_\beta\phi_i)}\partial_\alpha\phi_i - \frac{\partial f}{\partial(\partial_\beta\mathbf{p}_\gamma)}\partial_\alpha\mathbf{p}_\gamma \\ \sigma^a & = & \zeta\phi_2\phi_3\mathbf{pp}. \end{array} \tag{5.2.10}$$

where η is the volume-averaged viscosity, $\eta = \phi_1\eta_1 + (\phi_2 + \phi_3)\eta_2$, with η_1 buffer viscosity and η_2 cell viscosity. The divergence of the Ericksen stress yields the interfacial forces:

$$\nabla\cdot\sigma^e = -(\nabla\mathbf{p})\cdot\mathbf{h} - \sum_{i=1}^{3}\phi_i\nabla\frac{\delta F}{\delta\phi_i}.$$

With the free energy density functional given above, the various chemical potentials are given by

$$\begin{aligned}
\mu_3 &= \frac{\delta F}{\delta \phi_3} = \frac{\delta F_S}{\delta \phi_3} \\
\mu_2 &= \frac{\delta F}{\delta \phi_2} = \frac{\delta F_S}{\delta \phi_2} + \frac{\delta F_{\mathbf{p}}}{\delta \phi_2}, \\
\mu_1 &= \frac{\delta F}{\delta \phi_1} = \frac{\delta F_S}{\delta \phi_1} + \frac{\delta F_B}{\delta \phi_1} + \frac{\delta F_{surf}}{\delta \phi_1} + \frac{\delta F_{anch}}{\delta \phi_1}, \\
\mathbf{h} &= -\frac{\delta F}{\delta \mathbf{p}} = -\frac{\delta F_{\mathbf{p}}}{\delta \mathbf{p}} - \frac{\delta F_{anch}}{\delta \mathbf{p}},
\end{aligned} \tag{5.2.11}$$

where

$$\begin{aligned}
\frac{\delta F_S}{\delta \phi_i} &= 3\sqrt{2}\gamma_{is}\varepsilon\left(-\nabla^2\phi_i + f_s'(\phi_i)\right) + \gamma_{123}\phi_i\Pi_{j=1,j\neq i}^{3}\phi_j, i = 1, 2, 3, \\
\frac{\delta F_B}{\delta \phi_1} &= 3\sqrt{2}\gamma_{1b}\left(\nabla^4\phi_1 - f_b'(\phi_1)\nabla^2\phi_1 - \nabla^2 f_b(\phi_1) + f_b'(\phi_1)f_b(\phi_1)\right), \\
\frac{\delta F_{surf}}{\delta \phi_1} &= 3\sqrt{2}\lambda_S\varepsilon\left(S(t) - S^*\right)\left(-\nabla^2\phi_1 + f_s'(\phi_1)\right). \\
\frac{\delta F_{\mathbf{p}}}{\delta \phi_2} &= \left(\frac{K}{2}(\nabla\mathbf{p})^2 + \frac{h_3}{4}\|\mathbf{p}\|^4 - \frac{h_1}{2}\|\mathbf{p}\|^2\right)\frac{\delta s}{\delta \phi_2}. \\
\frac{\delta F_{anch}}{\delta \phi_1} &= -\alpha_1\nabla\cdot\left((\mathbf{p}\cdot\nabla\phi_1)\mathbf{p}\right), \\
\frac{\delta F_{\mathbf{p}}}{\delta \mathbf{p}} &= \left(-K\nabla\cdot(s\nabla\mathbf{p}) - sh_1\mathbf{p} + sh_3\|\mathbf{p}\|^2\mathbf{p}\right) \\
\frac{\delta F_{anch}}{\delta \mathbf{p}} &= \alpha_1(\mathbf{p}\cdot\nabla\phi_1)\nabla\phi_1,
\end{aligned} \tag{5.2.12}$$

with $f_s(\phi)$ and $f_b(\phi)$ given by

$$f_s(\phi) = \frac{1}{\varepsilon^2}\phi^2(1-\phi)^2, \quad f_b(\phi) = \frac{1}{\varepsilon^2}\phi(\phi-1)(2\phi - 1 + \frac{\varepsilon}{\sqrt{2}}C_1). \tag{5.2.13}$$

Numerical Results

Table of model parameters

Paramters used in this draft are summarized in Table 5.1. Paraters with references for their order-of-magnitude are cited. Otherwise, thoese are model paramters, with values by our best guesses.

Numerical simulations of cell blebing

Here we summarize some of the promising results of the numerical study for cell wrinkling dynamics due to excess arch length or surface. A 3D simulation is

Table 5.1: Dimensional and dimensionless parameters.

Symbol	Description	value	Unit	Reference and Remarks
h	Characteristic length scale	1×10^{-5}	m	[108]
t_0	Characteristic time scale	1	s	[108]
ρ	Cell density	1.1×10^3	kg/m^3	[35]
η_1, η_2, η_3	Averaged viscosity	10.0	$N \cdot s/m^2$	$10^{-3} - 1$ [108] for cytosol,100 [46] for cortex
γ_{is}	Surface tension for the interface	5×10^{-5}	N/m	[89]
γ_{1b}	Bending rigidity of cell membrane	10^{-18}	$N \cdot m$	[102]
ε	Thickness of the interface	5×10^{-7}	m	model parameter
λ_1, λ_3	Motility parameter	10^{-8}	$m^3 \cdot s/kg$	model parameter
λ_p	Time relaxation for the nematic director **p**	1.0×10^6	s	model parameter
s_0	Excess surface area ratio	3.0		experiment measured
λ_S	Lagrange multiplier for excess surface area constraint	2.0×10^5	N/m^3	model parameter
K	elastic strength for cell cortex (Frank elastic cosntants)	10^{-11}	N	[129, 51]
h_1, h_3	Landau-deGennes nematic potential parameters	$2. \times 10^2$	N/m^2	model parameter
α_1	Parallel anchoring strength	10^{-11}	N	assume the same with K
ν	Nematic director tumbling parameter	1.2		rod-like flow aligning regime

provided in Figure 5.7 to demonstrate the capability of our model in predicting the cell wrinkling dynamics both temporally and spatially. The excess volume ratio is 1:3. As Ken's lab could not provide us with a quantitatively clear 3D cell morphology, we have to propose a 3D virtual cell by ourselves. Here in Figure 5.7(a), the targeted cell is shown. The time series of cell morphological change from a sphere to the target cell are provided in Figure 5.7(b-f).

5.3 A HYDRODYNAMIC MODEL FOR CYTOKINESIS OF EUKARYOTIC CELLS

Mathematical formulations of mutli-phase models

In this section, we propose a hydrodynamic model for the cell division process in a phase field formulation. In this model, we treat the cell and the surrounding liquid environment as a fluid mixture in the form of a single fluid with multiple components. The volume fractions of cytoplasm, nucleus and the buffer fluid outside the cell are

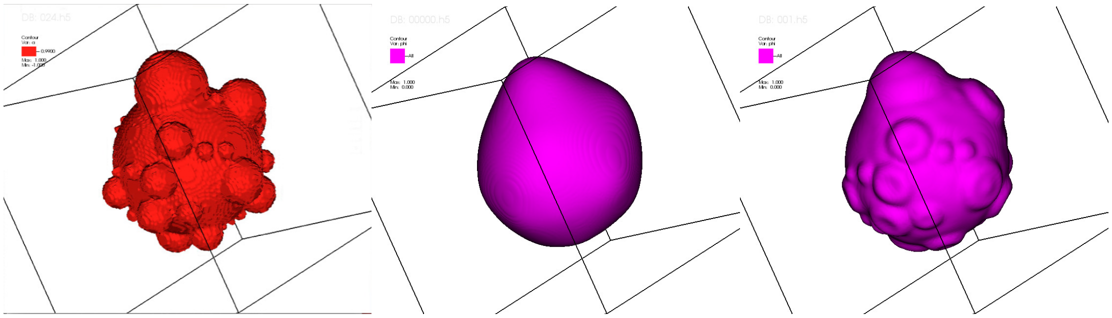

(a) Target (b) $t = 0$ (c) $t = 2$

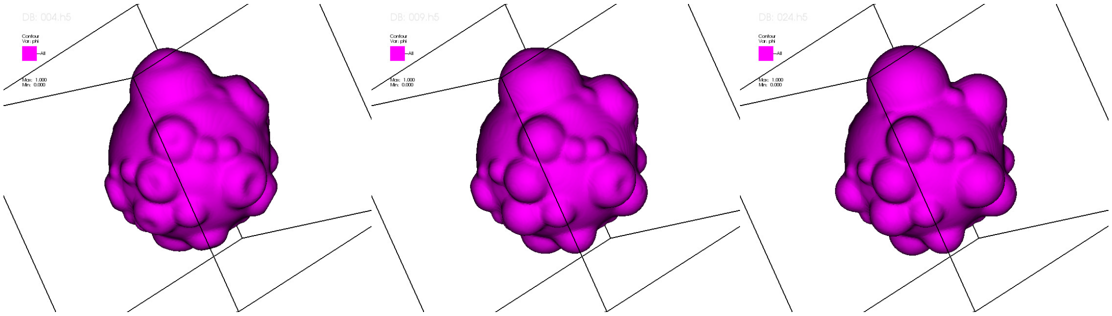

(d) $t = 5$ (e) $t = 10$ (f) $t = 25$

Figure 5.7: Simulation of cell wrinkling targeted at a 3D Cell provided by Alex. (a) Cell generated by plugging some bulge on a spherical cell; (b) Initial profile of the cell; (c-f) cell profile at time $t = 0, 2, 5, 10, 25$ correspondingly.

denoted by ϕ_1, ϕ_2 and ϕ_3, respectively. For incompressible materials, we enforce

$$\phi_1 + \phi_2 + \phi_3 = 1. \tag{5.3.14}$$

Here, we assume the buffer is a viscous fluid, so is the nucleus. Though the cytoplasm can be treated as a viscoelastic fluid, in this paper, we also treat it as a viscous fluid within the time scale of interest for simplicity. The cell membrane (together with the cortical layer) is the level set defined by $\{\phi_1 = \frac{1}{2} = \phi_3\}$ and the membrane of the nucleus is the level set defined by $\{\phi_2 = \frac{1}{2} = \phi_1\}$. Notice that this is a globally multi-phase while locally binary system since there is no contact between nucleus and buffer at any time. The volume-average velocity, density and viscosity for this fluid mixture is defined as

$$\mathbf{v} = \sum_{i=1}^{3} \phi_i \mathbf{v}_i, \quad \rho = \sum_{i=1}^{3} \phi_i \rho_i, \quad \eta = \sum_{i=1}^{3} \phi_i \eta_i, \tag{5.3.15}$$

where $\mathbf{v}_i, \rho_i, \eta_i$ is the effective velocity, density and viscosity for component i, $i = 1, 2, 3$. Figure 5.12 is a schematic cartoon of a 3D cell cross-section with individual components and diffuse interface labeled.

For a given interface defined by the phase variable $\phi = 1/2$, i=2,3, the unit normal of the cell membrane and the nucleus membrane are denoted by $\mathbf{n}_1$, $\mathbf{n}_2$, respectively. The mean curvatures of the cell membrane and nucleus membrane are denoted by κ_1, κ_2, which can be approximated [109] by

$$\mathbf{n}_i = \frac{\nabla \phi_i}{|\nabla \phi_i|}, \quad \kappa_i = \nabla \cdot \mathbf{n}_i \approx \frac{1}{|\nabla \phi_i|} \left(\nabla^2 \phi_i + \frac{2}{\varepsilon^2} \phi_i (1 - \phi_i)(2\phi_i - 1) \right), \quad i = 1, 2, \tag{5.3.16}$$

with ε representing the thickness of the nucleus membrane and cell membrane at steady state. We note that ε is a model parameter which we can adjust.

Thermodynamic free energy

The free energy of this mixture system is proposed as

$$F = \int_\Omega f d\mathbf{x}, \tag{5.3.17}$$

where Ω is the computational domain (in which the cell resides together with the buffer fluid), and f is the free energy density function. There are different choices for the free energy density function of the three phase fluids. Here we adopt a simple one:

$$\begin{aligned} f \quad = \quad & \tfrac{1}{2}\Big(\gamma_{s1} \|\nabla \phi_1\|^2 + \gamma_{s2} \|\nabla \phi_2\|^2 + \gamma_{s3} \|\nabla \phi_3\|^2 \\ & + \gamma_1 \phi_1^2 \phi_2^2 + \gamma_2 \phi_2^2 \phi_3^2 + \gamma_3 \phi_3^2 \phi_1^2 + \gamma_4 \phi_1^2 \phi_2^2 \phi_3^2 \Big). \end{aligned} \tag{5.3.18}$$

An alternative is given by

$$\begin{aligned} f \quad = \quad & \tfrac{1}{2}\Big(\gamma_{s1} \|\nabla \phi_1\|^2 + \gamma_{s2} \|\nabla \phi_2\|^2 + \gamma_{s3} \|\nabla \phi_3\|^2 \\ & + \gamma_1 \phi_1^2 (1 - \phi_1)^2 + \gamma_2 \phi_2^2 (1 - \phi_2)^2 + \gamma_3 \phi_3^2 (1 - \phi_3)^2 + \gamma_4 \phi_1^2 \phi_2^2 \phi_3^2 \Big), \end{aligned} \tag{5.3.19}$$

where γ_{si}, $i = 1, 2, 3$, govern the strength of the conformational entropy between different components, $\gamma_1, \gamma_2, \gamma_3$ control the strength of the bulk/mixing energy for each pair of components, and γ_4 is a Lagrangian multiplier to penalize the coexistence of the distinct phases. Our numerical studies show that these two choices of free energy density functions yield qualitatively the same results. Thus, in our study presented in this paper, we choose the second, i.e. equation (5.3.19). We remark that more features can be added to the model by augmenting the corresponding free energy.

Transport equations for biomass

Given the specific form of the free energy density (5.3.19), we assume that each component in the fluid mixture is convected by the volume-averaged velocity as well as transported via the gradient of osmotic pressure. Then, the transport equations for each biomass component are given as follows

$$\partial_t \phi_i + \nabla \cdot (\mathbf{v}\phi_i) = \nabla \cdot \left(\sum_{j=1}^{3} \alpha_{ij} \nabla \frac{\delta F}{\delta \phi_j} \right) + g_i, \quad i = 1, 2, 3, \tag{5.3.20}$$

where $\frac{\delta F}{\delta \phi}_i$ are the chemical potentials of F with respect to ϕ_i, $i = 1, 2, 3$. Here (α_{ij}), $i = 1, 2, 3$, $j = 1, 2, 3$, is the motility matrix and g_i,$i = 1, 2, 3$, are the reactive terms, respectively. Given specific free energy, saying (5.3.19), the chemical potentials could be derived as

$$\frac{\delta F}{\delta \phi_i} = -\gamma_{si} \nabla^2 \phi_i + \gamma_i \phi_i (1 - \phi_i)(1 - 2\phi_i) + \gamma_4 \phi_i \Pi^3_{j=1, j\neq i} \phi_j^2, \quad i = 1, 2, 3. \tag{5.3.21}$$

Note that the volume fractions add up to 1: $\sum_{i=1}^{3} \phi_i = 1$ for incompressible mixtures, as given by (5.3.15). This along with the Onsager reciprocal principle implies [64, 65]

$$\sum_{j=1}^{3} \alpha_{ij} = 0, \quad \alpha_{ij} = \alpha_{ji}. \tag{5.3.22}$$

The off-diagonal mobility coefficients can be obtained from the diagonal coefficients

$$\alpha_{12} = \frac{1}{2}(\alpha_{33} - \alpha_{11} - \alpha_{22}), \quad \alpha_{13} = \frac{1}{2}(\alpha_{22} - \alpha_{11} - \alpha_{33}), \quad \alpha_{23} = \frac{1}{2}(\alpha_{11} - \alpha_{22} - \alpha_{33}), \tag{5.3.23}$$

where we assume the diagonal motility parameters have the following form

$$\alpha_{ii} = \lambda_i \phi_i (1 - \phi_i), \tag{5.3.24}$$

with λ_i representing the strength of motility parameters for the corresponding component i, i=1,2,3.

By incompressibility condition, it follows that

$$\sum_{i=1}^{3} g_i = 0. \tag{5.3.25}$$

At the onset of cell division, the parent cell normally increases in cytoplasmic and organelle volume (the G1 phase) as well as increases in genetic materials (the G2 phase) right before the replication during the S phase. This process can be modeled by proposing the reactive kinetics for the time rate of change in the volume fractions:

$$g_1 = c_1 H_1(t)\phi_1\phi_3 - c_2 H_2(t)\phi_1\phi_2, \tag{5.3.26}$$

$$g_2 = c_2 H_2(t)\phi_1\phi_2, \tag{5.3.27}$$

$$g_3 = -c_1 H_1(t)\phi_1\phi_3. \tag{5.3.28}$$

Here $H_i(t), i = 1, 2$, are Heviside functions defined by

$$H_1(t) = \begin{cases} 1, & t < t_1, \\ 0, & t \geq t_1, \end{cases} \quad H_2(t) = \begin{cases} 1, & t < t_2, \\ 0, & t \geq t_2, \end{cases} \tag{5.3.29}$$

where t_1 is the critical checkpoint, at which the parent cell has just duplicated its volume, t_2 is the critical checkpoint, at which the nucleus has doubled its volume. Thus, before t_1 the parent cell keeps reproducing its cytoplasm to expand volume. After it doubles its volume, reproduction of cytoplasm ceases and cell proliferation begins. The growth kinetics is assumed to be originated from the interface between the buffer and cytoplasm as well as the nucleus and the cytoplasm.

Although our formulation in equation (5.3.20) is consistent, in real numerical simulations, we don't need to calculate every single phase due to the incompressibility constraint. In our later discussion, we only keep track of the transport of ϕ_2 and ϕ_3, since ϕ_1 can be obtained through the incompressibility condition (5.3.14).

Continuity and momentum equation

In order to close this system, we need to supplement the system with the continuity equation and momentum equation for the fluid mixture. By assuming the average velocity in the fluid mixture solenoidal, we have

$$\begin{aligned} \rho(\partial_t \mathbf{v} + \mathbf{v} \cdot \nabla \mathbf{v}) &= -\nabla p + \nabla \cdot \tau + \mathbf{F}_e, && (5.3.30) \\ \nabla \cdot \mathbf{v} &= 0, && (5.3.31) \end{aligned}$$

where ρ is the volume-averaged density (5.3.15), p is the hydrostatic pressure and τ is the viscoelastic stress tensor and $\mathbf{F}_e$ is the elastic body force yielding the surface tension of the cell membrane and the contractile force due to actin-myosin filaments. The viscoelastic stress tensor is proposed as follows,

$$\tau = 2\eta \mathbf{D} + \tau_e, \quad \mathbf{D} = \frac{1}{2}\Big(\nabla \mathbf{v} + \nabla \mathbf{v}^T\Big) \tag{5.3.32}$$

where the first term $2\eta\mathbf{D}$ sums up the viscous stress from each component with $\mathbf{D}$ the rate of strain tensor, and the second term τ_e is the elastic stress for the cytoplasm. Here η is the volume-averaged viscosity given in (5.3.15). A constitutive equation could be proposed for τ_e relating to the specific structure of the cortex layer. In this paper, however, we set $\tau_e = 0$ for the time scale of our interest and simplicity.

For the elastic body force or the interfacial force $\mathbf{F}_e$, we adopt the surface force yielded by the variation of the free energy. In addition, we propose a proxy force mimicking the cytokinetic ring, a contractible ring responsible for the cytokinesis of the animal cell, which is similar to the one used in [60],

$$\mathbf{F}_e = \sum_{j=1}^{3} \frac{\delta F}{\delta \phi_j} \nabla \phi_j + \kappa_1 f_{d1} \phi_1 \nabla \phi_1 + \kappa_2 f_{d2} \phi_2 \nabla \phi_2, \tag{5.3.33}$$

where the first term is the interfacial force, due to the material change at the interface between each component and the second term is the proxy force mimicking the normal force generated by the cytokinetic ring, consisting of actomyoisn networks immediate within the cell membrane. We note, this proxy force provides the contractible force necessary for dividing the cell. As we alluded to in the introduction, we will leave the model of tracking the spatial distribution of actin-filament networks regulated by myosins in the cytokinetic ring for a future work. Here κ_1, κ_2 are the mean-curvature of the cell membrane and nucleus membrane as given in (5.3.16), and f_{di}, i=1,2 denote the strength of the cytokinetic ring force, which by following the idea in [60] are proposed as follows

$$\begin{aligned} f_{d1} &= H_{d1}(\phi_2, t)\tfrac{\gamma_{d1}}{||\mathbf{x}-c_1|-|\mathbf{x}-c_2||+\varepsilon_d}, \\ f_{d2} &= H_{d2}(\phi_3, t)\tfrac{\gamma_{d2}}{||\mathbf{x}-c_1|-|\mathbf{x}-c_2||+\varepsilon_d}, \end{aligned} \tag{5.3.34}$$

where

$$\begin{aligned} H_{d1}(\phi_2, t) &= \begin{cases} 0, & \text{otherwise}, \\ 1, & \phi_2 = 0 \quad \& \quad t > t_3. \end{cases} \\ H_{d2}(\phi_3, t) &= \begin{cases} 0, & \text{otherwise}, \\ 1, & \phi_3 = 0 \quad \& \quad t_2 < t < t_3. \end{cases} \end{aligned} \tag{5.3.35}$$

are heaviside functions to restrict the force on cell membrane and the nucleus membrane at different stages of the cell division process, respectively, and c_1 and c_2 are the mass centers of the separated nuclei, respectively, i.e.,

$$c_1 = \frac{\int_{\Omega_1} \phi_2(\mathbf{x})\mathbf{x}d\mathbf{x}}{\int_{\Omega_1} \phi_2(\mathbf{x})d\mathbf{x}}, \quad c_2 = \frac{\int_{\Omega_2} \phi_2(\mathbf{x})\mathbf{x}d\mathbf{x}}{\int_{\Omega_2} \phi_2(\mathbf{x})d\mathbf{x}}, \tag{5.3.36}$$

where Ω_1 and Ω_2 are the domains occupied by the two nuclei, $\gamma_{di}, i = 1, 2$ are two parameters characterizing the strength of f_{di}, respectively, and ε_d is a small number employed here to avoid the singularity of f_{di}, where we use 0.01 in the paper. Here, t_2 is the checkpoint for the nucleus to begin separating after the size of the cell has been doubled and t_3 is the critical checkpoint when the nucleus has been divided into two separate nuclei.

Notice that this cytokinetic ring force counters the force due to the one of surface tension along the cytokinetic ring. We did not incorporate this cytokinetic ring force into the thermodynamic free energy since this is a proxy for the active force generated by actin-myosin filament on the cytokinetic ring through the released of the hydrolyzed ATP. In the current context, it is not a potential force.

Dimensionless governing equations in the three phase model

We denote the reference time scale as t_0, reference length scale as h and reference mass density as ρ_0. Then, the variables and parameters are nondimensionalizsed as follows:

$$\begin{aligned} &\tilde{\rho}_i = \tfrac{\rho_i}{\rho_0}, \tilde{\mathbf{x}} = \tfrac{\mathbf{x}}{h}, \tilde{t} = \tfrac{t}{t_0}, \tilde{\mathbf{v}} = \tfrac{\mathbf{v}t_0}{h}, \tilde{\lambda}_i = \tfrac{\lambda_i}{t_0}, \tilde{c}_j = c_j t_0, \\ &\tilde{\gamma_{si}} = \tfrac{\gamma_{si} kT t_0^2}{\rho h^4}, \quad \tilde{\gamma_k} = \tfrac{\gamma_k kT t_0^2}{\rho_0 h^2}, \quad Re_i = \tfrac{\rho_0 h^2}{\eta_i t_0}, \end{aligned} \tag{5.3.37}$$

with $i = 1, 2, 3$, $j = 1, 2$, and $k = 1, 2, 3, 4$. For convenience, we drop those tildes on the symbols. The governing equations in dimensionless form are summarized as

$$\begin{aligned} \rho(\partial_t \mathbf{v} + \mathbf{v} \cdot \nabla \mathbf{v}) &= \nabla \cdot \left(\tfrac{1}{Re} (\nabla \mathbf{v} + \nabla \mathbf{v}^T) \right) - \nabla p + \mathbf{F}_e, \\ \nabla \cdot \mathbf{v} &= 0, \\ \partial_t \phi_i + \nabla \cdot (\mathbf{v} \phi_i) &= \nabla \cdot (\textstyle\sum_{j=1}^3 \alpha_{ij} \nabla \tfrac{\delta F}{\delta \phi_i}) + g_i, \quad i = 1, 2, 3, \end{aligned} \tag{5.3.38}$$

where

$$\begin{aligned} &\mathbf{F}_e = \textstyle\sum_{j=1}^3 \tfrac{\delta F}{\delta \phi_j} \nabla \phi_j + \sum_{i=1}^2 \kappa_i f_{di} \phi_i \nabla \phi_i, \\ &g_1 = c_1 H_1(t) \phi_1 \phi_3 - c_2 H_2(t) \phi_1 \phi_2, \quad g_2 = c_2 H_2(t) \phi_1 \phi_2, \quad g_3 = -c_1 H_1(t) \phi_1 \phi_3, \\ &\tfrac{1}{Re} = \textstyle\sum_{i=1}^3 \phi_i \tfrac{1}{Re_i}, \quad \rho = \sum_{i=1}^3 \phi_i \rho_i. \end{aligned} \tag{5.3.39}$$

Numerical results and discussion

Parameters and initial setup

For convenience, all parameters used in the model are listed in Table 5.2 unless noticed otherwise. These parameters are chosen from the published literature or user-defined based on our best guesses. We note that, although we have formulated the three-phase model by treating the nucleus separately as a new phase for eukaryotic

Table 5.2: Dimensional parameters.

Symbol	Description	value	Unit	Reference
T	Absolute Temperature	303	Kelvin	[130]
k	Boltzmann constant	1.38×10^{-23}	$m^2kg/(s^2K)$	[130]
h	Characteristic length scale	5×10^{-5}	m	[83]
t_0	Characteristic time scale	0.1	s	[83]
ρ	Reference density	1.1×10^3	kgm^{-3}	[35]
η_1	Dynamic viscosity of cytoplasm	1×10^{-2}	$kgm^{-1}s^{-1}$	[44]
η_3	Dynamics viscosity of ECM	5×10^{-3}	$kgm^{-1}s^{-1}$	[44]
η_2	Dynamics viscosity of nucleus	2×10^{-2}	$kgm^{-1}s^{-1}$	
$\gamma_{A,B,C}$	Distortional energy coefficient	2.5×10^7	m^{-1}	
$\gamma_{1,2,3,4}$	Bulk free energy coefficient	1.875×10^{20}	m^{-3}	
$\lambda_{1,2,3}$	Motility parameter for each component	1×10^{-11}	$kg^{-1}m^3s$	
c_1, c_2	Growth rate of cytoplasm and nucleus	5.0	s^{-1}	
γ_{d1}	Stimulating force strength	2.5	m^{-3}	
γ_{d2}	Stimulating force strength	15	m^{-3}	

cells, this model is also well-suited for studying cytoplasmic dynamics and cytokinesis without considering the nucleus. In those cases, we simply set the initial condition of ϕ_2 as zero and assume that c_1 and c_2 are the centers of mass for the cytoplasm distributed on each side of the division plane, respectively. In this two phase model, ϕ_1 represents the volume fraction of the substance inside the cell membrane and ϕ_3 represents the volume fraction of the buffer, i.e. extra cellular matrix (ECM) outside of the cell membrane.

Dynamics of cell growth and cytokinesis

During the cell mitotic process and before cytokinesis ensues, the parent cell doubles its cytoplasmic volume while in the meantime duplicates its genetic substances (DNAs and chromosomes). The cell morphological change during this process can be studied using the current model by simply shutting down the contracting force and switch on the growth dynamics of the cell, which are characterized by the moments known as the checkpoints present in the current model. At the molecular level, the DNAs and chromosomes replicate themselves and then separate into two distinct sets of DNAs and chromosomes. Immediately following, two offspring nuclei form, each of which contains the genetic information inherited from the parent cell. This is a complex process involving the formation of mitotic spindle and its elongation in the axis perpendicular to the cytokinetic ring, which is beyond the scope of our current multiphase model's. In the current model, we focus on cytokinesis after the offspring nuclei are separated. We coarse-grain the nucleus as a viscous bulk fluid inside the cytoplasm. After the two offspring nuclei are separated, the nuclei effectively position the division plane, known as the cleavage plane, after which cytokinesis ensues. When the cleavage plane is placed right in the middle of the long axis of the cell, symmetric cell division can be observed. Otherwise, cytokinesis may result in asymmetric division or failure of cytokinesis. We will discuss the case of asymmetric division later, but will not discuss the failure of cytokinesis since its cause is not fully explored yet even experimentally.

In Figure 5.13, we show a detailed simulation of cytokinesis for eukaryotic cells mentioned above. In particular, the 3D view of the cell growth and division process is portrayed in Figure 5.13(a-e). The volume of the cytoplasm is doubled at the moment shown in Figure 5.13(b), after which we see the formation of the cleavage furrow in Figure 5.13(c), and the abscission that physically cleaves the parent cell into two offspring cells in Figure 5.13(d). In Figure 5.13(e), we observe the offspring cell reshapes into round morphology under the influence of surface tension on its own membrane. To our best knowledge, this is the first numerical simulation in full 3D using a hydrodynamic phase field model. To better visualize the dynamics of nucleus in the cytokinesis process, a series of 2D slices at $x = 0.5$ are plotted in Figure 5.13(f-j). In particular, the cytoplasmic bridge connecting the two offspring cells is observed (shown in Figure 5.13(i)), which agrees quantitatively with the morphogenetic pattern obtained from the experimental observations shown in Figure 5.13(k).

We note that the advantage of the 3D hydrodynamic model is its capability to couple the interior cytoplasmic fluid flow with the exterior fluid flow through the cell membrane and visualize important hydrodynamic quantities such as stress tensors, forces and the hydrostatic pressure throughout the domain during the cellular morphological transformation. In Figure 5.14, the detail of the viscous stress $\eta\mathbf{D}$, volume-averaged velocity $\mathbf{v}$, as well as the hydrostatic pressure p at time $t = 8.5$ are depicted. The stress tensor at $(\mathbf{x}, t)$ is visualized as a 3D ellipsoidal object at $\mathbf{x}$, whose semiaxes signify the length of the three eigenvalues of the second order symmetric tensor, respectively. From Figure 5.14(b), a zoomed view of viscous stress tensor is shown. The stress is highly inhomogeneous at the contractile ring on the division plane (cleavage plane), which correlates well with the velocity field shown in Figure 5.14(f-g), as the cytokinetic ring of the cell is contracting. Besides, the gradient of the hydrostatic pressure is also high at the cleavage plane as well as the interface between the cell nucleus and cytoplasm.

In addition, the distribution of the proxy force and the surface tension force are also shown in Figure 5.15. Seen from Figure 5.15(a), the proxy force is mainly distributed on the cell membrane (the interface between cytoplasm and ECM), with much higher values on the division plane, contracting the cell membrane towards the center of the long axis of the cell. This is shown in the 2D view of proxy force in Figure 5.15(b-c). Same as the proxy force, the surface tension force is also distributed on the interfaces. However, surface tension is more evenly distributed, aiming to smooth out the interface. These two forces oppose to each other on the interface. It is the competition between the surface tension force and the proxy force on the division plane that ultimately contributes to the success of cytokinesis.

Asymmetric cell cytokinesis

The positioning of the contractile ring (or cytokinetic ring) located on the division plane is dictated by the mitotic spindle and other intracellular processes. It can affect the morphology of the offspring cells significantly. If the contractile ring is positioned not in a symmetric manner, then asymmetric cell division, or cell polarization could be observed. Asymmetric cell division, which includes cell polarization and cytokinesis is essential for generating cell diversity during development.

Here, we conducted two case studies, where we only concentrate on the cell membrane dynamics by setting $\phi_2 = 0$. Note in this case, c_1 and c_2 in the model are chosen as mass centers of the half cell divided by the cleavage plane. For the first numerical study, we choose the contractile ring on the plane at $x = 0.9$ with $L_x = 2.0$ for the whole domain. An asymmetric cell division is simulated shown in Figure 5.16. The asymmetric cell division in the intermediate stage resembles qualitatively to the budding yeast polarization.

Another case of asymmetric cell division is due to the fact that the concentration of actin-myosin filament is distributed heterogeneously during cytokinesis. As a simple experiment, we set γ_{d1}, the contractile strength as a function of space, to mimic this inhomogeneous contractile force due to the heterogeneous distribution of actin-myosin filaments on the division plane. In this context, we set $\tilde{\gamma}_{d1} = \gamma_{d1} y$, i.e. the strength of the contractile force is higher on upper membrane of the cell. As a result, a plane-cell type asymmetric cell division can be observed, shown in Figure 5.17. The cleave furrow is observed in Figure 5.17(h), which agrees qualitatively with the cleavage in the jellyfish aequorea.

Conclusion

In this section, we use a multi-phase field model to study cytokinesis of an eukaryotic cell during its mitotic process. Several interesting phenomena such as dynamics and morphological patterns of symmetric or asymmetric cell division in cytokinesis are numerically simulated with the model. These morphological patterns agree qualitatively with experimental observations. This simplified model is thus proven to be an effective tool for studying cytokinesis during the cell division process.

Evidently, this simplified model needs significant improvement in order to make it capable to simulate the complex biological and chemical processes in addition to the mechanical process during the real cell mitotic process. Nevertheless, it marks our first attempt in developing a full 3D hydrodynamic model for cell division in a hydrodynamically consistent way. Within the framework for modeling cell dynamics that the model has provided, we can further superimpose additional features to it or add additional cellular components/structures to it. In our future work, we will incorporate the actomyosin microstructure to the cell cortical layer and derive the contractile force on the cytokinetic ring based on their density and orientation distribution instead of using the proxy force. In addition, the viscoelastic properties of cytoplasm, the chromosome spindle, as well as its elongation on facilitating cytokinesis could be added incrementally as well.

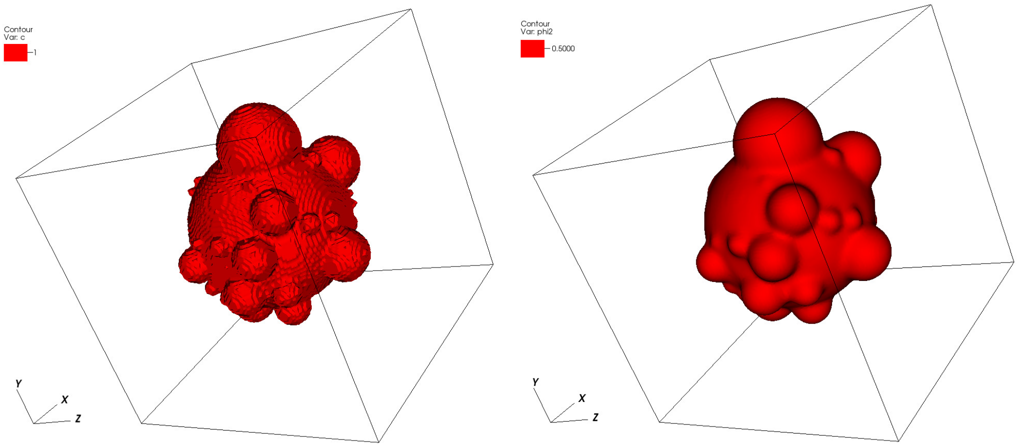

(a) Target (b) Steady state cell morphology

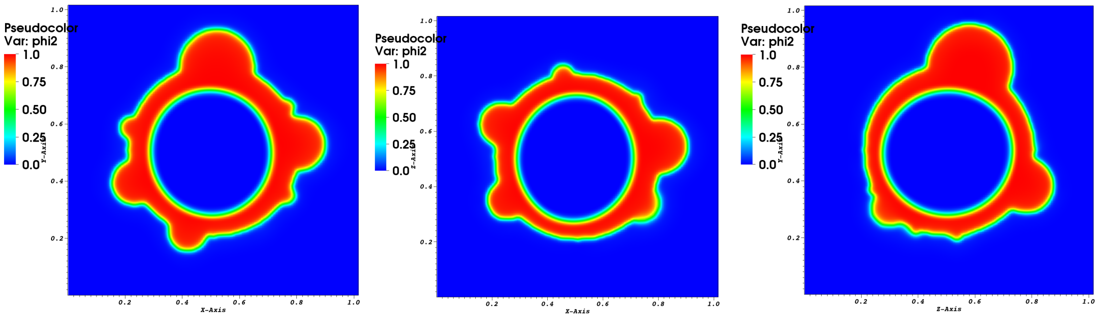

(c) cortex 2D slice at $z = 0.5$ (d) cortex 2D slice at $y = 0.5$ (e) cortex 2D slice at $x = 0.5$

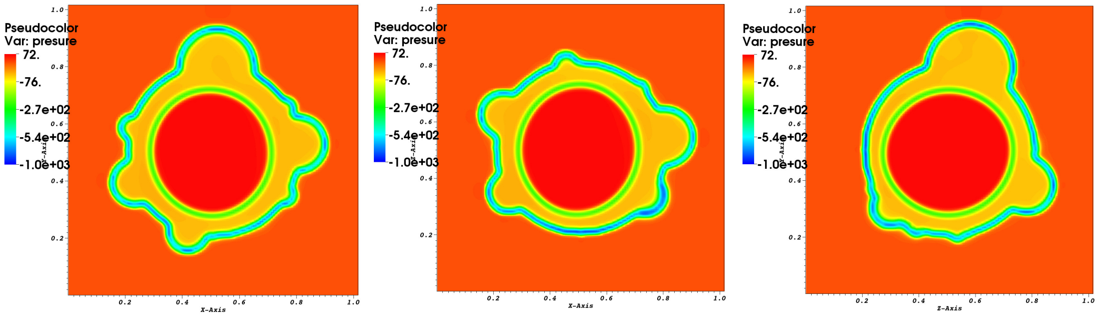

(f) 2D slice of p at $z = 0.5$ (g) 2D slice of p at $y = 0.5$ (h) 2D slice of p at $x = 0.5$

Figure 5.8: Simulation of cell blebbing. (a) targeted cell morphology generated by Alex; (b) stead state cell morphology predicted by our model; (c-e) 2D slice views of the cytosol at $z = 0.5$, $y = 0.5$ and $x = 0.5$, respectively; (f-h) 2D slice view of the pressure at $z = 0.5$, $y = 0.5$ and $x = 0.5$, respectively. The unit for pressure is Pa.

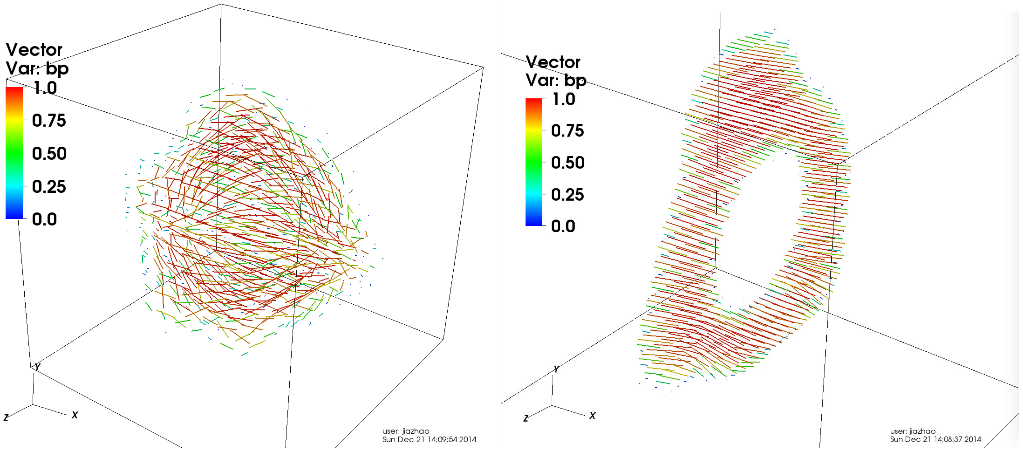

(a) 3D view of Cortex Arrangement (b) 2D slice at $x = 0.5$

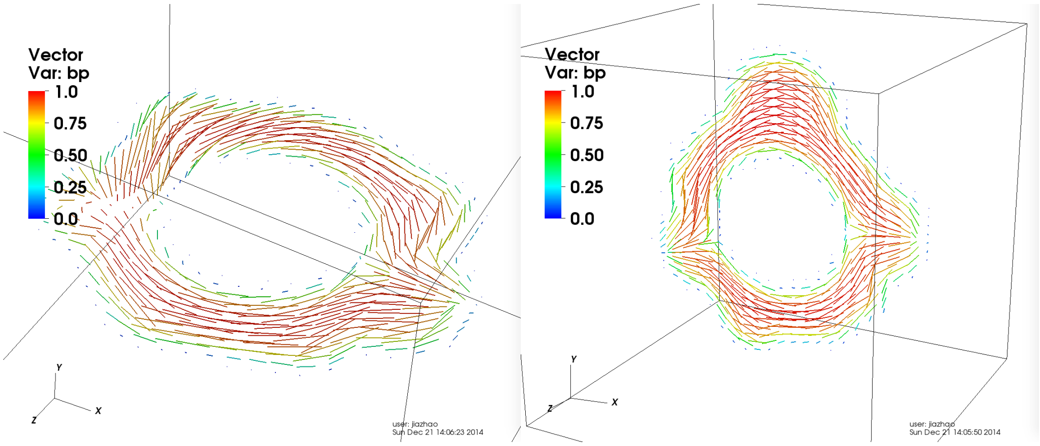

(c) 2D slice at $y = 0.5$ (d) 2D slice at $z = 0.5$

Figure 5.9: Arrangement of filaments in cortex for the steady state cell morphology. (a) 3D view of the cortex arrangement; (b-e) 2D slice views of the cortex at $x = 0.5$, $y = 0.5$, $z = 0.5$, respectively.

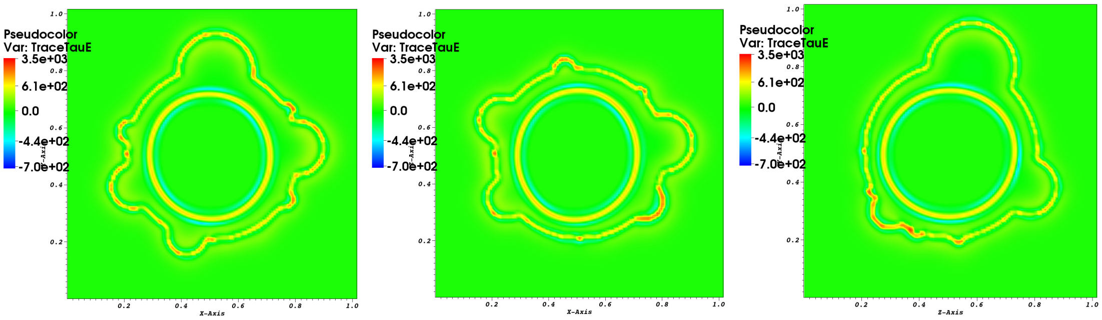

(a) first invariant at $z = 0.5$ (b) first invariant at $y = 0.5$ (c) first invariant at $x = 0.5$

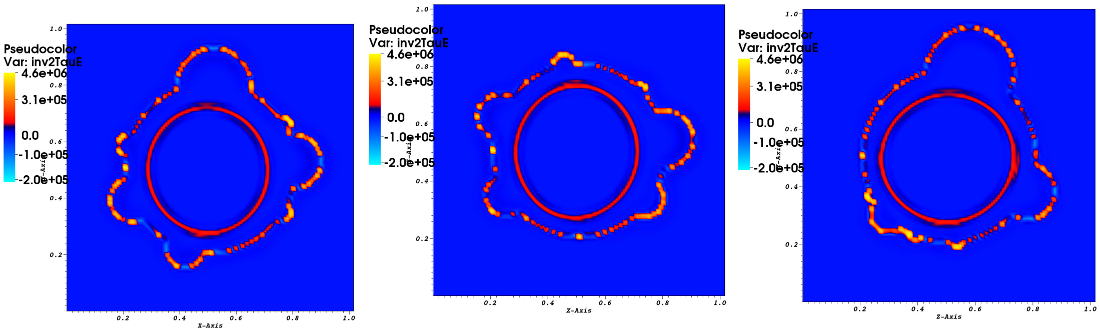

(d) second invariant at $z = 0.5$ (e) second invariant at $y = 0.5$ (f) second invariant at $x = 0.5$

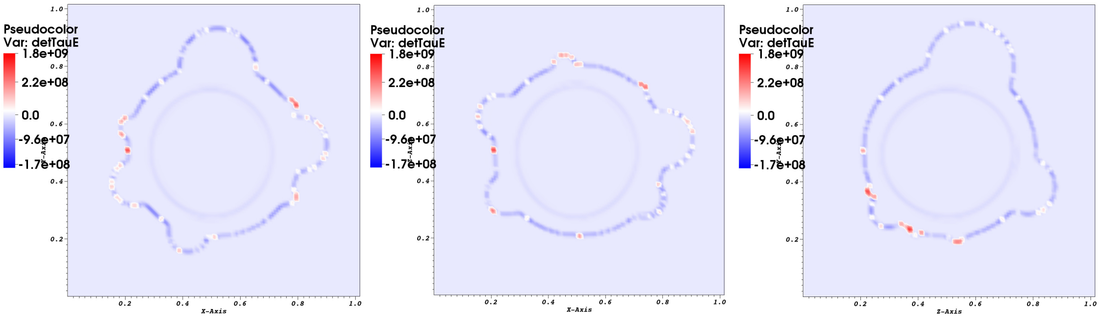

(g) third invariant at $z = 0.5$ (h) third invariant at $y = 0.5$ (i) third invariant at $x = 0.5$

Figure 5.10: Three invariants for stress tensor τ^e. (a-c) 2D slices of the first invariant; (d-f) 2D slices of the second invariant; (g-i) 2D slices of the third invariant. The unit for first invariant is Pa, second invariant is Pa^2, third invariant is Pa^3.

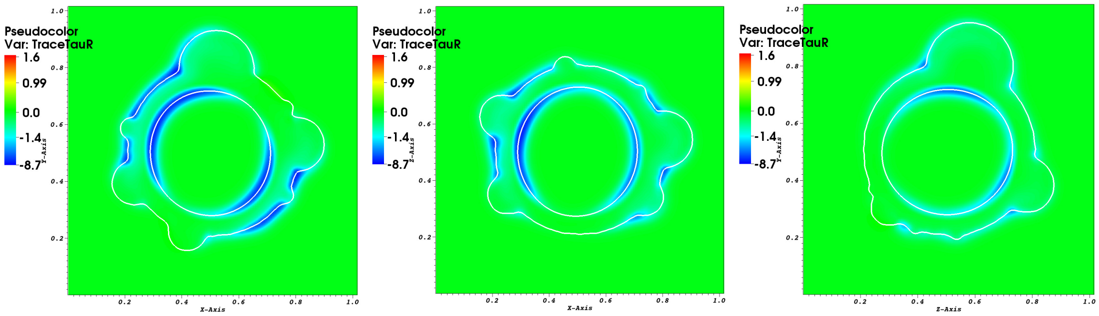

(a) first invariant at $z = 0.5$ (b) first invariant at $y = 0.5$ (c) first invariant at $x = 0.5$

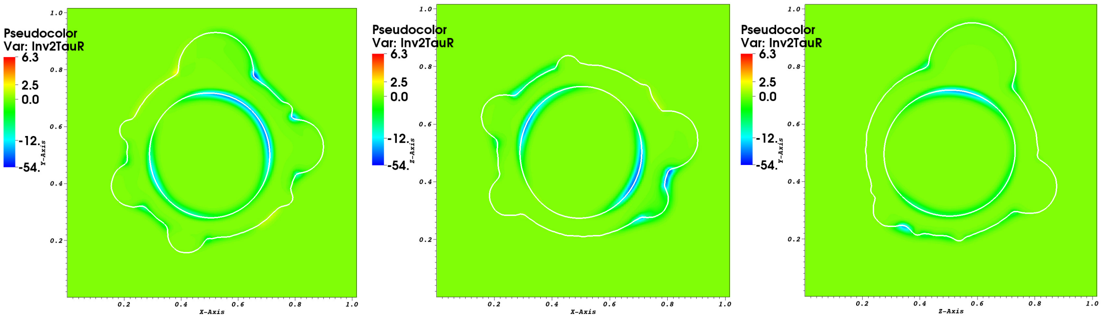

(d) second invariant at $z = 0.5$ (e) second invariant at $y = 0.5$ (f) second invariant at $x = 0.5$

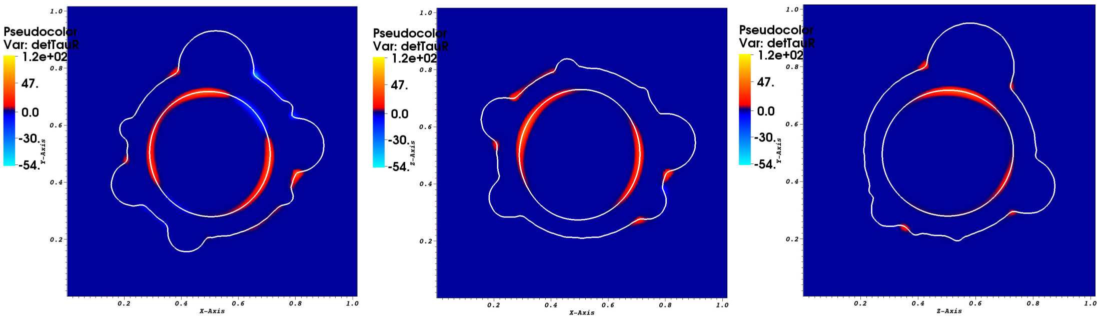

(g) third invariant at $z = 0.5$ (h) third invariant at $y = 0.5$ (i) third invariant at $x = 0.5$

Figure 5.11: Three invariants for stress tensor τ^r. (a) the cell morphology; (b) the first invariant of τ^r; (c) the second invariant of τ^r; (d) the third invariant of τ^r.The unit for first invariant is Pa, second invariant is Pa^2, third invariant is Pa^3.

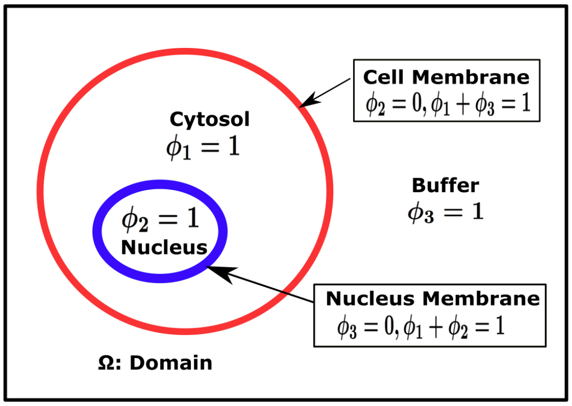

Figure 5.12: A schematic cartoon for the phase-field cell model. Ω represents the computational domain. Here ϕ_1, ϕ_2, ϕ_3 represent the volume fractions of cytosol, nucleus, and cell buffer, respectively. The nucleus membrane is traced by $\phi_1 = \phi_2 = \frac{1}{2}$ and the cell membrane is traced by $\phi_1 = \phi_3 = \frac{1}{2}$.

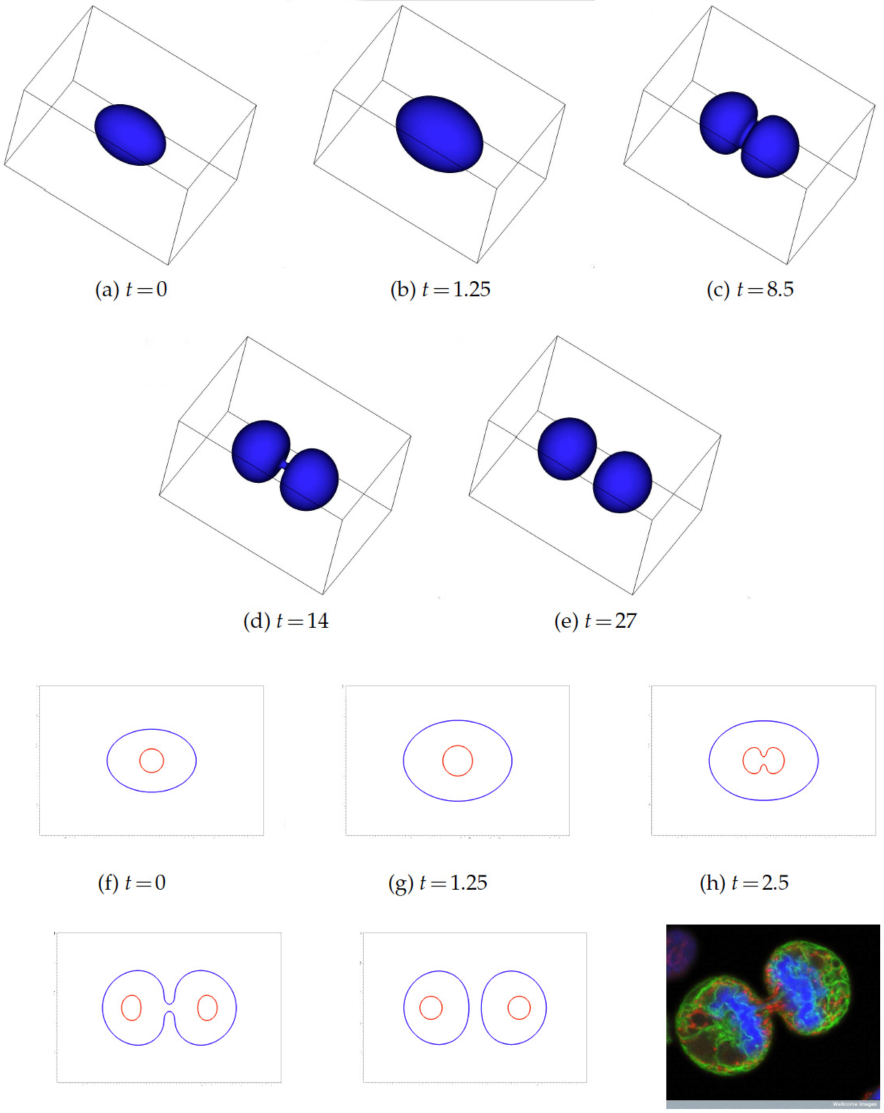
(a) $t=0$ (b) $t=1.25$ (c) $t=8.5$

(d) $t=14$ (e) $t=27$

(f) $t=0$ (g) $t=1.25$ (h) $t=2.5$

(i) $t=15$ (j) $t=26.5$ (k)

Figure 5.13: Cell growth and cytokinesis. This figure shows a parent cell duplicates its nucleus and cytoplasm, then splits into two identical offspring cells. (a)-(e) 3D Numerical simulations of the cell division process at different stages; (f-j) 2D slices at $x = 0.5$ for the cell division process; (k) a dividing melanoma cell just before it divides into two offspring cells completely (Courtesy of Welcome Images).

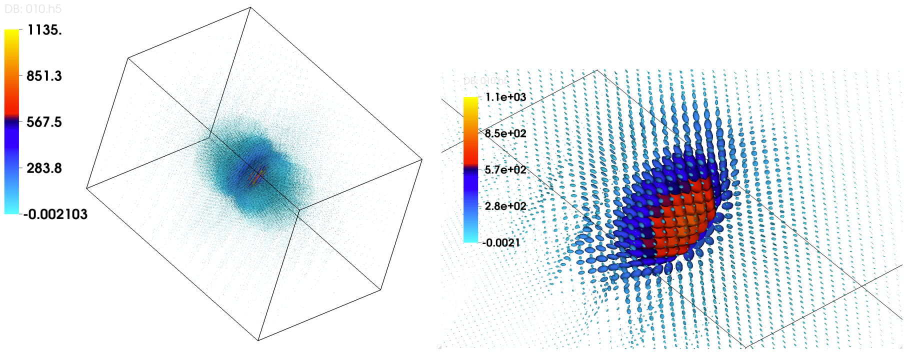

(a) $\eta\mathbf{D}$ (b) Zoom view of $\eta\mathbf{D}$

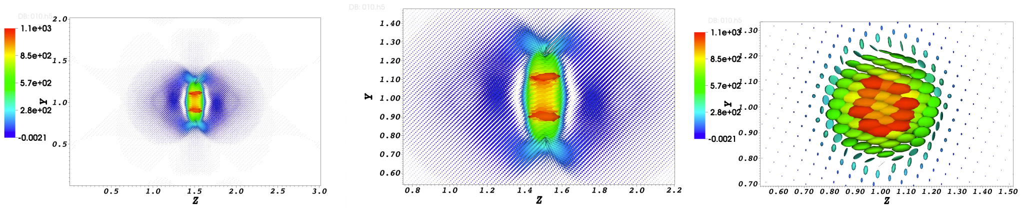

(c) $\eta\mathbf{D}$ at $x = 0.75$ (d) Zoom view of $\eta\mathbf{D}$ at $x = 0.75$ (e) $\eta\mathbf{D}$ at $z = 0.5$

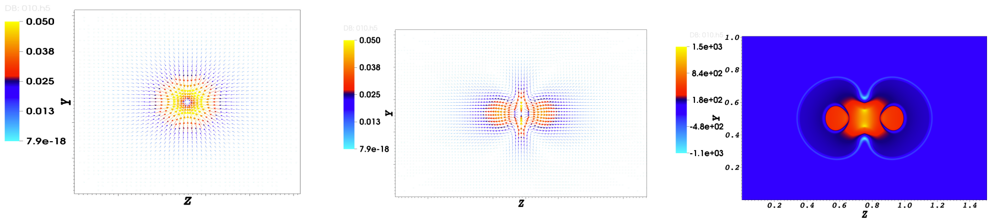

(f) $\mathbf{v}$ at $x = 0.75$ (g) $\mathbf{v}$ at $z = 0.5$ (h) p at $x = 0.75$

Figure 5.14: Hydrodynamic variables of cell cytokinesis at $t = 8.5$. This figure shows the hydrodynamic variables, including viscous stress tensor $\beta\mathbf{D}$, volume-averaged velocity $\mathbf{v}$ and the hydrostatic pressure p distribution at time $t = 8.5$ for the simulation shown in Figure 5.13. (a) 3D view of the stress tensor as ellipsoids; (b) a zoomed view of the stress tensor; (c-e) 2D slices of the stress tensor field; (f-g) 2D slices of the velocity filed; (h) a 2D slice of the pressure field.

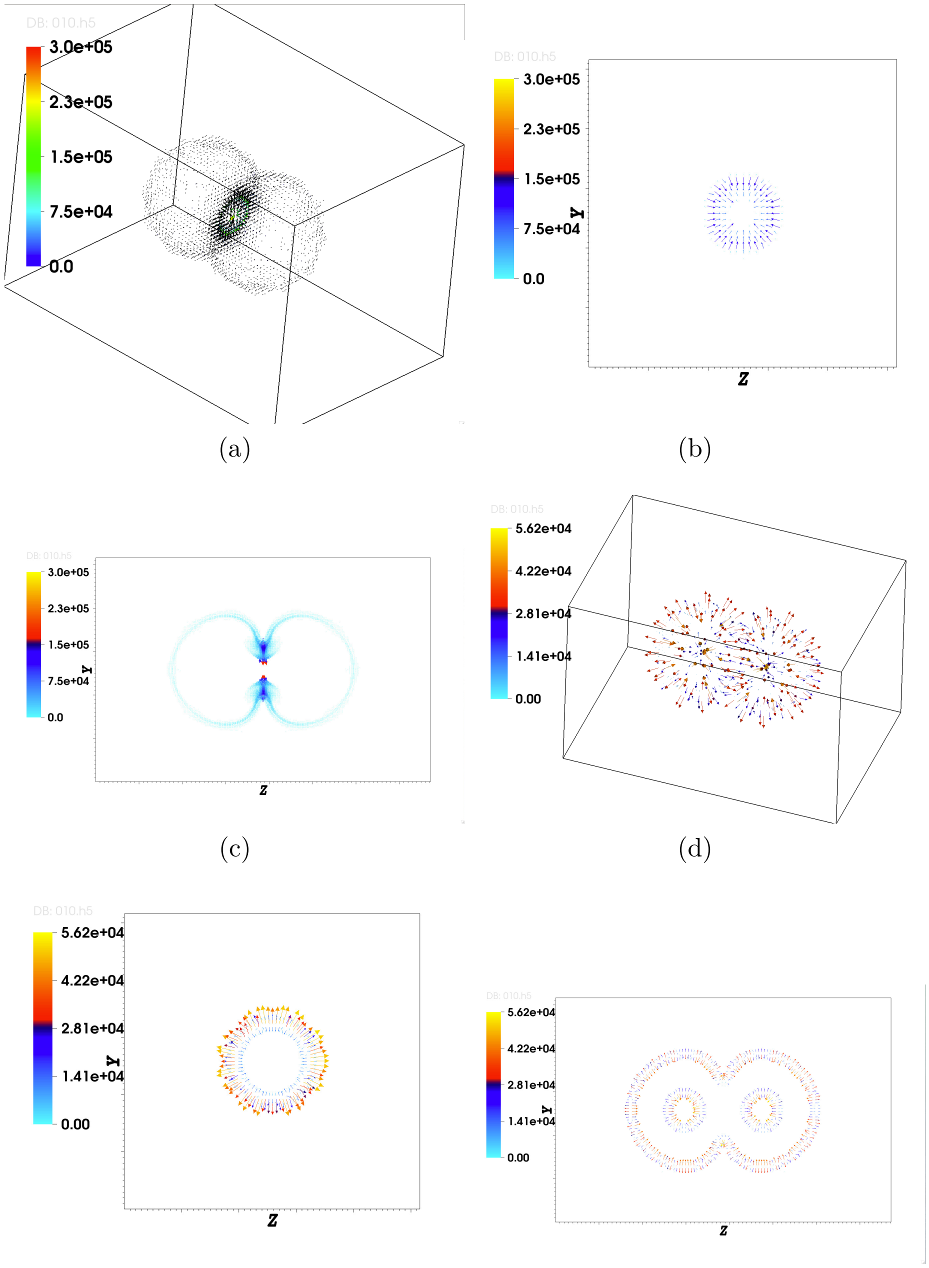

(a) (b) (c) (d) (e) (f)

Figure 5.15: Visualization of the proxy force and the surface tension force. This figure shows the proxy force and surface tension force at time $t = 8.5$ of the simulation shown in Figure 5.13.(a) 3D view of the proxy force; (b) a 2D slice of proxy force at $x = 0.5$; (c) a 2D slice of proxy force at $z = 0.5$; (d) 3D view of the surface tension force; (e) a 2D slice of the surface tension force at $x = 0.5$; (f) a 2D slice of the surface tension force at $z = 0.5$. The proxy force opposes to the surface tension force at the cytokinetic ring.

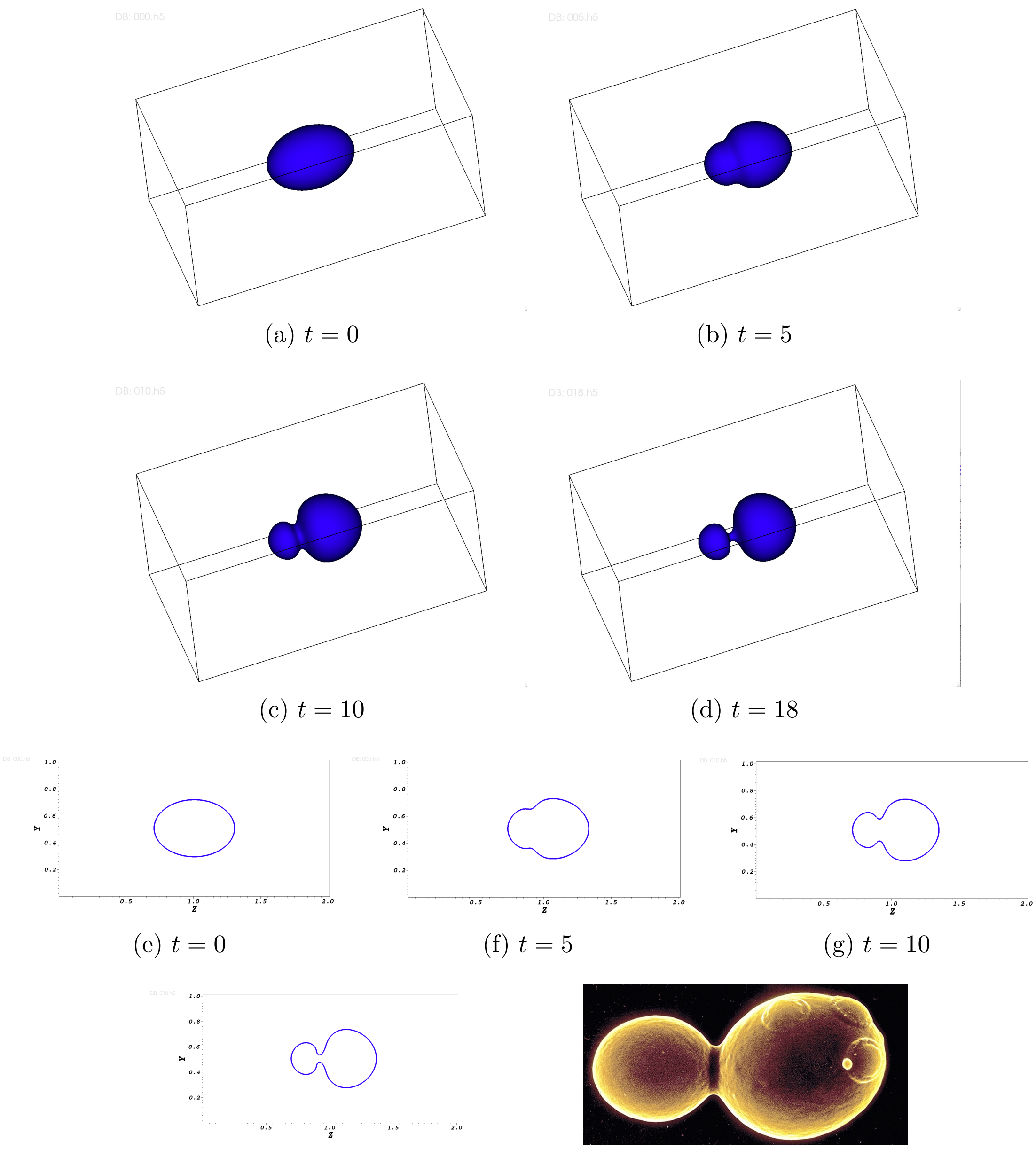

(a) $t = 0$ (b) $t = 5$

(c) $t = 10$ (d) $t = 18$

(e) $t = 0$ (f) $t = 5$ (g) $t = 10$

(h) $t = 18$ (i)

Figure 5.16: Asymmetric cell division due to the asymmetric positioning of cleavage plane. This figure shows an asymmetric cell cytokinesis process in which the division plane is positioned in an asymmetric fashion along the long axis of the cell. (a)-(d) 3D Numerically simulated cell division process at different time; (e-h) 2D slices ($z = 0.5$) of cell division process at different time; (f)a budding yeast. This asymmetric cell division resembles the yeast cell budding process (found on ppdictionary.com).

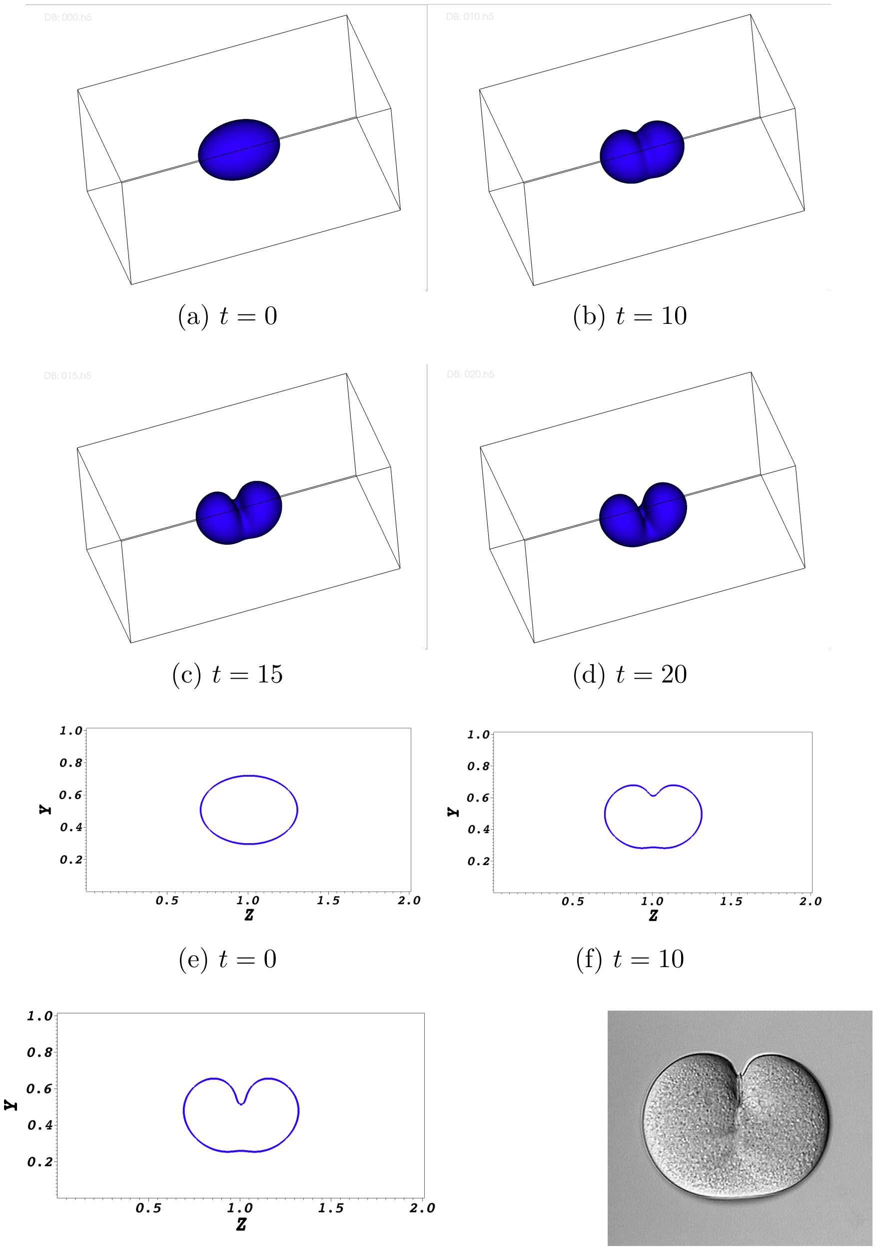

(a) $t = 0$ (b) $t = 10$

(c) $t = 15$ (d) $t = 20$

(e) $t = 0$ (f) $t = 10$

(g) $t = 15$ (h)

Figure 5.17: Asymmetric cleavage furrow formation due to inhomogeneous actomyosin distribution. This figure shows the asymmetric cleavage furrow formation due to the inhomogenous contractile force along the cytokinetic ring induced by heterogenous actomyosin distribution on the contractile plane. (a-d) 3D view of the asymmetric cell division at different time; (e-g) 2D slices ($z = 0.5$) of the asymmetric cell division at different time; (h) cleavage furrow in the jellyfish Aequorea (found on celldynamics.org).

CHAPTER 6

CONCLUSION

In this thesis, we have developed a general framework for deriving thermodynamically consistent hydrodynamic models, following the generalized Onsager's principle [79, 80]. This modeling approach is effective and systematical, as we have shown that many widely-used hydrodynamic models are actually special cases of the general model.

As the hydrodynamic models are usually high-order, nonlinear and always coupled, new efficient and stable numerical schemes are needed. Guided by the continuous energy dissipation law, we propose linearly, energy-stable, semi-discrete schemes for several particular cases of the general hydrodynamic model [139, 143, 141, 140]. Then, the space is discretized by central-differences and the discrete scheme is implemented using CUDA on GPUs for high-performance computing.

Using the general modeling framework, we have proposed several hydrodynamic models to investigate cellular dynamics, in particular, (i) antimicrobial persistence in biofilms; (ii) animal cells cytokinesis. By treating the biofilm as a complex fluid mixture, we have developed a modeling framework and computational tool to study biofilm dynamics and functions using both kinetic and continuum approaches. The bacteria in biofilms have been categorized into various types either by their persistence to antimicrobial agents or by their reactions to quorum sensing molecules. Using these models and the accompanying computational tools, we have studied dynamics of 3D heterogeneous biofilm formation under hydrodynamic stress, investigated the pros and cons of quorum sensing mechanism in hydrodynamic environment [136], explored the mechanism of antimicrobial persistence [137], looked into optimal dosing strategies, and examined the cell motility on the development of biofilm morphology. As an integral part of the study, we have also validated our model of biofilm persistence to antimicrobial treatment against the experimental results obtained in Dr. Ya Shen's laboratory [100]. Using the validated model, we then probe the scenario of biofilm relapse after the antimicrobial treatment [142]. These studies have demonstrated that our models are effective for analyzing the mechanism of biofilm formation and functions.

In a similar manner, we treat the animal cell together with its buffer outside of the cell membrane as a viscoelastic fluid mixture. Using the general modeling approach mentioned above, we have developed a modeling framework for simulating the space-time evolution of cell morphology change: bleb-like protrusions [144], mitotic cell rounding from a flat configuration on the substrate [138], cell motility and cell cytokinesis [135, 134]. The simulation results from the hydrodynamic models have shown some qualitative agreement with experiment observations.

Bibliography

[1] Erik Alpkvist et al. “Three-dimensional biofilm model with individual cells and continuum EPS matrix”. In: *Biotechnology and Bioengineering* 94.5 (2006), pp. 961–979.

[2] Stephanie M. Amato, Mehmet A. Orman, and Mark P. Brynildsen. “Metabolic control of persister formation in Escherichia coli”. In: *Molecular Cell* 50.4 (May 2013), pp. 475–487.

[3] Nathalie Q. Balaban et al. “Bacterial persistence as a phenotypic switch”. In: *Science* 305.5690 (2004), pp. 1622–1625.

[4] Florent Baty and Marie-Laure Delignette-Muller. “Estimating the bacterial lag time: which model, which precision?” In: *International Journal of Food Microbiology* 91 (2004), pp. 261–277.

[5] Kenneth W. Bayles. “The biological role of death and lysis in biofilm development”. In: *Nature Reviews Microbiology* 5.9 (Sept. 2007), pp. 721–726.

[6] K. Berndl et al. “Shape transformations of giant vesicles: extreme sensitivity to bilayer asymmetry”. In: *Europhysics Letters* 13.7 (1990), pp. 659–664.

[7] Steve P. Bernier et al. “Starvation together with the SOS response mediates high biofilm-specific tolerance to the fluoroquinolone ofloxacin”. In: *PLoS Genetics* 9.1 (2013).

[8] Matthew L. Blow, Sumesh P. Thampi, and Julia M. Yeomans. “Biphasic Lyotropic active nematics”. In: *Physical Review Letters* 113 (2014), p. 248303.

[9] Giorgia Borriello et al. “Arginine or nitrate enhances antibiotic susceptibility of pseudomonas aeruginosa in biofilms”. In: *Antimicrobial Agents and Chemotherapy* 50.1 (2006), pp. 382–384.

[10] Franck Boyer and Sebastian Minjeaud. “Numerical schemes for a three component Cahn-Hilliard model”. In: *ESAIM. Mathematical Modelling and Numerical Analysis* 45.4 (2011), pp. 697–738.

[11] Michael R. W. Brown, Phillip J. Collier, and Peter Gilbert. “Influence of growth rate on susceptibility to antimicrobial agents: modification of the cell envelope and batch and continuous culture studies”. In: *Antimicrobial Agents and Chemotherapy* 34.9 (1990), pp. 1623–1628.

[12] J. W. Cahn and J. E. Hilliard. “Free energy of a nonuniform system. I. Interfacial free energy.” In: *J. Chem. Phys.* 28 (1958), pp. 258–267.

[13] John W. Cahn. “Free Energy of a Nonuniform System. II. Thermodynamic Basis”. In: *Journal of Chemical Physics* 30.5 (1959).

[14] John W. Cahn and John E. Hilliard. “Free Energy of a Nonuniform System. I. Interfatial Free Energy”. In: *Journal of Chemical Physics* 28.2 (1958).

[15] Julie C. Canman et al. “Determining the position of the cell division plane”. In: *Nature* 424 (2003), pp. 1074–1078.

[16] Gerardo Cárcamo-Oyarce et al. “Quorum sensing triggers the stochastic escape of individual cells from Pseudomonas putida biofilms”. In: *Nat Commun* 6 (2015), p. 5945.

[17] David L. Chopp et al. “The dependence of quorum sensing on the depth of a growing biofilm”. In: *Bulletin of Mathematical Biology* 65 (2003), pp. 1053–1079.

[18] N. G. Cogan et al. “Optimal control strategies for disinfection of bacterial populations with persister and susceptible dynamics”. In: *Antimicrobial Agents and Chemotherapy* 56.9 (2012), pp. 4816–4826.

[19] N.G. Cogan. “Effects of persister formation on bacterial response to dosing”. In: *Journal of Theoretical Biology* 238 (3 2006), pp. 694–703.

[20] N. Condette, C. Melcher, and E. Suli. “Spectral approximation of pattern-forming nonlinear evolution equations with double-well potentials of quadratic growth”. In: *Math. Comp.* 80 (2011), pp. 205–223.

[21] Elena Deligianni et al. “Pseudomonas aeruginosa Cystic Fibrosis isolates of similar RAPD genotype exhibit diversity in biofilm forming ability in vitro”. In: *BMC Microbiology* 10.38 (2010).

[22] Masao Doi. “Onsager’s variational principle in soft matter”. In: *Journal of Physics: Condensed Matter* 23 (2011), p. 284118.

[23] Q. Du, M. Li, and C. Liu. “Analysis of a phase field Navier-Stokes vesicle-fluid interaction model”. In: *Dis. Conti. Dyn. Sys.-B* 8(3) (2007), pp. 539–556.

[24] Q. Du, C. Liu, and X. Wang. “Simulating the Deformation of Vesicle Membranes under Elastic Bending Energy in Three Dimensions”. In: *J. Comp. Phys.* 212 (2005), pp. 757–777.

[25] Bob Eisenberg, YunKyong Hyon, and Chun Liu. “Energy variational analysis of ions in water and channels: field theory for primitive models of complex ionic fluids”. In: *Journal of Chemical Physics* 133 (2010), p. 104104.

[26] J. L. Ericksen. “Conservation laws for liquid crystals”. In: *Trans. Soc. Rheol.* 5 (1961), pp. 23–34.

[27] James J. Feng et al. “An energetic variational formulation with phase field methods for interfacial dynamics of complex fluids advantages and challenges”. In: *The IMA Volumes in Mathematics and its Applications* 141 (2005), pp. 1–26.

[28] A. Fick. “Poggendorff’s Annalen.” In: *Journal of the american mathematics society* (1855), pp. 59–86.

[29] J. A. Fozard et al. “Inhibition of quorum sensing in a computational biofilm simulation”. In: *BioSystems* 109 (2012), pp. 105–114.

[30] Mallory R Frederick et al. “A mathematical model of quorum sensing in patchy biofilm communities with slow background flow”. In: *Canadian Applied Mathematics Quarterly* 18.3 (2010), pp. 267–298.

[31] Mallory R Frederick et al. “A mathematical model of quorum sensing regulated EPS production in biofilm communities”. In: *Theoretical Biology and Medical Modelling* (2011).

[32] Cristina Garcia-Aljaro et al. “Quorum-sensing regulates biofilm formation in virio schophthalmi”. In: *BMC Microbiology* 12 (2012), p. 287.

[33] William M. Gelbart and Avinoam Ben-Shaul. “The new science of complex fludis”. In: *Journal of Physical chemistry* 100.13 (1996), pp. 13169–13189.

[34] P. G. de Gennes and J. Prost. *The Physics of Liquid Crystals*. Oxford University Press, 1993.

[35] William H. Grover et al. “Measuring single-cell density”. In: *PNAS* 108.27 (2011), pp. 10992–10996.

[36] J. L. Guermond, P. Minev, and J. Shen. “An Overview of Projection methods for incompressible flows”. In: *Comput. Methods Appl. Mech. Engrg.* 195 (2006), pp. 6011–6045.

[37] Yashodhan Hatwalne et al. “Rheology of active-particle suspensions”. In: *Physical Review Letters* 92.11 (2004).

[38] Frank Hauber et al. “Thermodynamically consistent models for two component vesicles”. In: *International Journal of Biomathematics and Biostatistics* 2.1 (2013), pp. 19–48.

[39] R. Hinson and W. Kocher. “Model for Effective Diffusivities in Aerobic Biofilms”. In: *Journal of Environmental Engineering* 122.11 (1996), pp. 1023–1030.

[40] S. M. Hunt, M. A. Hamilton, and P.S. Stewart. “A 3D model of antimicrobial action on biofilms”. In: *Water Science and Technology* 52.7 (2005), pp. 143–148.

[41] Yunkyong Hyon, Do Young Kwak, and Chun Liu. “Energetic variational approach in complex fluids: maximum dissipation principle”. In: *Discrete and Continuous Dynamical Systems. Series A* 26.4 (2010), pp. 1291–1304.

[42] B. Jerome. “Surface effects and anchoring in liquid crystals”. In: *Rep. Prog. Phys.* 54 (1991), p. 391.

[43] Frank Julicher and Reinhard Lipowsky. “Shape transformations of vesicles with intramembrane domains”. In: *Physical Review E* 53.3 (1996), pp. 2670–2683.

[44] Tomasz Kalwarczyk et al. “Comparative analysis of viscosity of complex liquids and cytoplasm of mammalian cells at the nanoscale”. In: *Nano Letters* 11.5 (2011), pp. 2157–2163.

[45] Tomoko Kamasaki, Masako Osumi, and Issei Mabuchi. “Three-dimensional arrangement of F-actin in the contractile ring of fission yeast”. In: *The Journal of Cell Biology* 178.5 (2007), pp. 765–771.

[46] Helene Karcher et al. “A three dimensional viscoelastic model for cell deformation with experimental verification”. In: *Biophysical Journal* 85 (2003), pp. 3336–3349.

[47] James P. Keener, Sarthok Sircar, and Aaron L Fogelson. “Kinetics of swelling gels”. In: *SIAM Journal of Applied Mathematics* 71.3 (2011), pp. 854–875.

[48] Iris Keren et al. “Persister cells and tolerance to antimicrobials”. In: *FEMS Microbiology Letters* 230 (2004), pp. 13–18.

[49] Daniel Kessler, Ricardo H. Nochetto, and Alfred Schmidt. “A posteriori error control for the Allen-Cahn problem: circumventing Gronwall’s inequality”. In:

M2AN. Mathematical Modelling and Numerical Analysis 38.1 (2004), pp. 129–142.

[50] Isaac Klapper and Jack Dockery. “Mathematical description of microbial biofilms”. In: *SIAM Review* 52.2 (2010), pp. 221–265.

[51] Bartlomiej Klus et al. “All optical measurement of elastic constants in nematic liquid crystals”. In: *Optics Express* 22.24 (2014), pp. 20357–30266.

[52] P. B. Sunil Kumar, Gerhard Gompper, and Reinhard Lipowsky. “Budding dynamics of multicomponent membranes”. In: *Physical Review Letters* 86.17 (2001), pp. 3911–3914.

[53] Patricia Kunda et al. “Moesin controls cortical rigidity cell rounding and spindle morphogenesis during mitosis”. In: *Current Biology* 18 (2008), pp. 91–101.

[54] Patrick De Leenheer and N. G. Cogan. “Failure of antibiotic treatment in microbial populations”. In: *Journal of Mathematical Biology* 59.4 (2009), pp. 563–579.

[55] F. M. Leslie. “Some constitutive equations for anisotropic fluids”. In: *Q. Jl. Mech. Appl. Math.* 19 (1966), pp. 357–370.

[56] F. M. Leslie. “Some constitutive equations for liquid crystals”. In: *Arch. Rational Mech. Anal.* 28 (1968), pp. 265–283.

[57] Zbigniew Lewandowski and Haluk Beyenal. *Fundamentals of Biofilm Research*. 2nd. CRC Press, 2013.

[58] Kim Lewis. “Persister Cells”. In: *Annual Review of Microbiology* 64.1 (2010), pp. 357–372.

[59] Kim Lewis. “Persister cells dormancy and infectious disease”. In: *Nature Reviews Microbiology* 5 (2007), pp. 48–56.

[60] Yibao Li, Ana Yun, and Junseok Kim. “An immersed boundary method for simulating a single axisymmetric cell growth and division”. In: *Journal of Mathematical Biology* 65 (2012), pp. 653–675.

[61] F. H. Lin. “Mathematics theory of liquid crystals”. In: *Applied Mathematics At The Turn Of Century* (1995).

[62] F. H. Lin. “On nematic liquid crystals with variable degree of orientation”. In: *Communications on Pure and Applied Mathematics* 44 (1991), pp. 453–468.

[63] Fanghua Lin and Changyou Wang. “Recent developments of analysis for hydrodynamic flow of nematic liquid crystals”. In: *Philosophical Transactions of the Royal Society of London Series A* 372 (2014), p. 20130361.

[64] Brandon Lindley, Qi Wang, and Tianyu Zhang. “A multicomponent model for biofilm-drug interaction”. In: *Discrete and Continuous Dynamical Systems Series B* 15 (2 2011), pp. 417–456.

[65] Brandon Lindley, Qi Wang, and Tianyu Zhang. “Multicomponent hydrodynamic model for heterogeneous biofilms: Two-dimensional numerical simulations of growth and interaction with flows”. In: *Physical Review E* 85 (3 2012), p. 031908.

[66] Reinhard Lipowsky. “Spontaneous tubulation of membranes and vesicles reveals membrane tension generated by spontaneous curvature”. In: *Faraday Discussions* 161 (2012), pp. 305–331.

[67] C. Liu and N.J. Walkington. “An Eulerian description of fluids containing visco-hyperelastic particles”. In: *Arch. Rat. Mech. Anal.* 159 (2001), pp. 229–252.

[68] Chun Liu and Jie Shen. “A phase field model for the mixture of two incompressible fluids and its approximation by a Fourier-spectral method”. In: *Physica D* 179.3-4 (2003), pp. 211–228.

[69] John S. Lowengrub, Andreas Ratz, and Axel Voigt. “Phase field modeling of the dynamics of multicomponent vesicles spinodal decomposition coarsening budding and fission”. In: *Physical Review E* 79.3 (2009).

[70] Amy Shaub Maddox and Keith Burridge. “RhoA is required for cortical retraction and rigidity during mitotic cell rounding”. In: *The Journal of Cell Biology* 160.2 (2003), pp. 255–265.

[71] Melanine M. Marketon et al. “Quorum sensing controls exopolysaccharide production in sinorhizobium melioti”. In: *Journal of Bacteriology* 185.1 (2003), pp. 325–331.

[72] Meltem Golgeli Matur et al. “An approximative approach for single cell spatial modeling of quorum sensing”. In: *Journal of Computational Biology* 22.3 (2015), pp. 227–235.

[73] Ann L. Miller. “The contractile ring”. In: *Current Biology* 21.24 (2011), pp. 976–978.

[74] Sebastian Minjeaud. “An unconditionally stable uncoupled scheme for a triphasic Cahnilliard Navier Stokes model”. In: *Numerical Methods for Partial Differential Equations* 29.2 (2013), pp. 584–618.

[75] Alex Mogilner et al. “Modeling Mitosis”. In: *Trends in Microbiology* 16.2 (2006), pp. 88–96.

[76] Don Monroe. “Looking for chinks in the armor of bacterial biofilms”. In: *PLoS Biology* 5.11 (2007), e307.

[77] Carey D. Nadell et al. “The evolution of quorum sensing in bacterial biofilms”. In: *PLoS Biology* 6.1 (2008), pp. 0171–0179.

[78] Erich A. Nigg. “Mitotic kinases as regulators of cell division and its checkpoints”. In: *Nature Reviews Molecular Cell Biology* 2 (2001), pp. 21–32.

[79] Lars Onsager. “Reciprocal relations in irreversible processes I”. In: *Physical Review* 37 (1931), pp. 405–426.

[80] Lars Onsager. “Reciprocal relations in irreversible processes. II”. In: *Physical Review* 38 (1931), pp. 2265–2279.

[81] Judith Perez-Velazquez et al. “A mathematical model to investigate quorum sensing regulation and its heterogeneity in Pseudomonas syringae on leaves”. In: *Ecological Complexity* 21 (2015), pp. 128–141.

[82] C. S. Peskin. “The immersed boundary method”. In: *Acta Numerica* 11 (2002), pp. 1–39.

[83] Christopher C. Poirier et al. “Deconvolution of the cellular force-generating subsystems that govern cytokinesis furrow ingression”. In: *PLOS Computational Biology* 8.4 (2012).

[84] Keith Poole. “Bacterial stress responses as determinants of antimicrobial resistance”. In: *Journal of Antimicrobial Chemotherapy* 20.5 (2012), pp. 227–234.

[85] Tiezheng Qian, Xiaoping Wang, and Ping Sheng. “A variational approach to moving contact line hydrodynamics”. In: *Journal of Fluid Mechanics* 564 (2006), pp. 336–360.

[86] Beatriz Quinones, Glenn Dulla, and Steven E. Lindow. “Quorum sensing regulates exopolysaccharide production motility and virulence in Pseudomonas syringae”. In: *Molecular Plant Microbe Interactions* 18.7 (2005), pp. 682–693.

[87] Elizabeth M. Rechl, Janet C. Effler, and Douglas N. Robinson. “The stress and strain of cytokinesis”. In: *Trends in Microbiology* 15.4 (2005), pp. 200–206.

[88] Mark E. Roberts and Philip S. Stewart. “Modeling protection from antimicrobial agents in biofilms through the formation of persister cells”. In: *Microbiology* 151 (2005), pp. 75–80.

[89] Guillaume Salbreux, Guillaume T. Charras, and Ewa Paluch. “Actin cortex mechanics and cellular morphogenesis”. In: *Trends in Cell Biology* 22.10 (2012), pp. 536–545.

[90] Jose A. Sanclement et al. “Bacterial biofilms in surgical specimens of patients with crhonic rhinosinusitis”. In: *Laryngoscope* 115.4 (Apr. 2005), pp. 578–582.

[91] Udo Seifert. “Configurations of fluid membranes and vesicles”. In: *Advances in Physics* 46.1 (1997), pp. 13–137.

[92] Udo Seifert, Karin Berndl, and Reinhard Lipowsky. “Shape transformations of vesicles phase diagram for spontaneous curvature and bilayer coupling models”. In: *Physical Review A* 44.2 (1991), pp. 1182–1202.

[93] J. Shen and X. Yang. “A phase-field model and its numerical approximation for two-phase incompressible flows with different densities and viscositites”. In: *SIAM J. Sci. Comput.* 32 (2010), pp. 1159–1179.

[94] J. Shen and X. Yang. “Energy stable schemes for Cahn-Hilliard phase-field model of two-phase incompressible flows”. In: *Chinese Ann. Math. series B* 31 (2010), pp. 743–758.

[95] J. Shen and X. Yang. “Numerical Approximations of Allen-Cahn and Cahn-Hilliard Equations”. In: *Discrete and Continuous Dynamical Systems. Series A* 28 (2010), pp. 1669–1691.

[96] J. Shen et al. “Second-order convex splitting schemes for gradient flows with Ehrlich-Schwoebel type energy: application to thin film epitaxy”. In: *in press, SIAM J. Numer. Anal* (2011).

[97] Jie Shen and Xiaofeng Yang. “Energy stable schemes for Cahn-Hilliard phase field model of two phase incompressible flows”. In: *Chinese Annals of Mathematics Series B* 31.5 (2010), pp. 743–758.

[98] Jie Shen and Xiaofeng Yang. “Numerical approximation of Allen-Cahn and Cahn-Hilliard equations”. In: *Discrete and Continuous Dynamical Systems Series B* 28.4 (2010), pp. 1669–1691.

[99] Ya Shen, Sonja Stojic, and Markus Haapasalo. “Antimicrobial Efficacy of Chlorhexidine against Bacteria in Biofilms at Different Stages of Development”. In: *Journal of Endodontics* 37.5 (2011), pp. 657–661.

[100] Ya Shen et al. “Development and experimental validation of a model for oral multispecies biofilm recovery after chlorhexidine treatment”. In: *submitted* (2014).

[101] Zhiya Sheng and Yang Liu. “Effects of silver nanoparticles on wastewater biofilms”. In: *Water Research* 45 (2011), pp. 6039–6050.

[102] Rudolf Simson et al. “Membrane bending modulus and adhesion energy of wild-type and mutant cells of Dictyostelium lacking talin or cortexillins”. In: *Biophysical Journal* 74 (1998), pp. 514–522.

[103] Stefanie Sonner, Messoud A. Efendiev, and Hermann J. Eberl. “On the well-posedness of a mathematical model of quorum-sensing in patchy biofilm communities”. In: *Mathematical Methods in the Applied Sciences* 34 (13 2011), pp. 1667–1684.

[104] Martin Philip Stewart. “The mechanics of Motiotic Cell Rounding”. In: *Ph.D. Thesis* (2012).

[105] Martin Philip Stewart et al. “Hydrostaic pressue and the actomyosin cortex drive mitotic cell rounding”. In: *Nature Research Letter* 469 (2011), pp. 226–231.

[106] P.A. Stewart et al. “An improved sharp interface method for viscoelastic and viscous two phase flows”. In: *Journal of Scientific Computing* 35 (2007).

[107] Philip S. Stewart. “Diffusion in biofilms”. In: *Journal of Bacteriology* 185.5 (2003), pp. 1485–1491.

[108] Wanda Strychalski and Robert D. Guy. “A computational model of bleb formation”. In: *Mathematical Medicine and Biology* 30 (2013), pp. 115–130.

[109] Y. Sun and C. Beckermann. “Sharp interface tracking using the phase-field equation”. In: *Journal of Computational Physics* 220 (2007), pp. 626–653.

[110] Jessica Ann Thompson et al. “Manipulation of the quorum sensing signal AI-2 affects the antibiotic-treated gut microbiota”. In: *Cell Reports* 10 (2015), pp. 1–11.

[111] Benjamin Vaughan, Bryan Smith, and David Chopp. “The influence of fluid flow on modeling quorum sensing in bacterial biofilms”. In: *Bulletin of Mathematical Biology* 72.5 (2010), pp. 1143–1165.

[112] Cuong Vuong et al. “Quorum-Sensing Control of Biofilm Factors in Staphylococcus epidermidis”. In: *Journal of Infectious Diseases* 188.5 (2003), pp. 706–718.

[113] Qi Wang and Tianyu Zhang. “Kinetic theories for biofilms”. In: *Discrete and Continuous Dynamical Systems Series B* 17.3 (2012), pp. 1027–1059.

[114] Qi Wang and Tianyu Zhang. “Review of mathematical models for biofilms”. In: *Solid State Communications* 150.21 (2010), pp. 1009–1022.

[115] Xiaoqiang Wang and Qiang Du. “Modelling and simulations of multi component lipid membranes and open membranes via diffuse interface approaches”. In: *Journal of Mathematical Biology* 56 (2008), pp. 347–371.

[116] Christopher M. Waters and Bonnie L. Basseler. “Quorum sensing: cell-to-cell communication in bacteria”. In: *Annual Review of Cell and Developmental Biology* 21.1 (2005), pp. 319–346.

[117] James N. Wilking et al. “Biofilms as complex fluids”. In: *MRS Bulletin* 36.5 (2011), pp. 385–391.

[118] S. M. Wise, C. Wang, and J. S. Lowengrub. “An energy-stable and convergent finite-difference scheme for the phase field crystal equation”. In: *SIAM J. Numer. Anal.* 47.3 (2009), pp. 2269–2288.

[119] S. M. Wise et al. “Efficient phase-field simulation of quantum dot formation in a strained heteroepitaxial film”. In: *Superlattices and Microstructures* 36 (2004), pp. 293–304.

[120] Shixin Xu, Ping Sheng, and Chun Liu. “An energetic variational approach for ion transport”. In: *Communications in Mathematical Sciences* 12.4 (2013), pp. 779–789.

[121] X. Yang et al. “Numerical simulations of jet pinching-off and drop formation using an energetic variational phase-field method”. In: *Journal of Computational Physics* 218.1 (2006), pp. 417–428.

[122] X. Yang et al. “Shear cell rupture of nematic liquid crystal droplets in viscous fluids”. In: *Journal of Non-Newtonian Fluid Mechanics* 166 (2011), pp. 487–499.

[123] Xiaofeng Yang. “Error analysis of stabilized semi-implicit method of Allen-Cahn Equation”. In: *Discrete and Continuous Dynamical Systems Series B* 11 (2009), pp. 1057–1070.

[124] Xiaofeng Yang et al. “Modeling and simulations of drop pinch-off from liquid crystal filaments and the leaky liquid crystal faucet immsersed in viscous fluids”. In: *Journal of Computational Physics* 236 (2013), pp. 1–14.

[125] Xiaogang Yang, M. Gregory Forest, and Qi Wang. “Near equilibrium dynamics and one-dimensional spatial—temporal structures of polar active liquid crystals”. In: *Chinese Physics B* 23.11 (2014).

[126] Xiaogang Yang and Qi Wang. “Capillary instability of axisymmetric, active liquid crystal jets”. In: *Soft Matter* 10.35 (2014), pp. 6758–6776.

[127] Jennifer Young and Sorin Mitran. “A numerical model of cellular blebbing: a volume-conserving fluid-structure interaction model of the entire cell”. In: *Journal of Biomechanics* 43 (2010), pp. 210–220.

[128] P. Yue et al. “A diffuse-interface method for simulating two-phase flows of complex fluids”. In: *J. Fluid Mech* 515 (2004), pp. 293–317.

[129] A. V. Zakharov, M. N. Tsvetkova, and V. G. Korsakov. “Elastic properties of liquid crystals”. In: *Physics of the Solid State* 44.9 (2002), pp. 1795–1801.

[130] Tianyu Zhang, Nick G. Cogan, and Qi Wang. “Phase-field models for biofilms I. theory and simulations”. In: *SIAM Journal of Applied Mathematics* 69 (2008), pp. 641–669.

[131] Tianyu Zhang, Nick G. Cogan, and Qi Wang. “Phase-field models for biofilms II. 2-d numerical simulations of biofilm-flow interaction”. In: *Communication in Computational Physics* 4.1 (2008), pp. 72–101.

[132] Hongkai Zhao et al. “A variational level-set approach to multiphase motion”. In: *J. Comput. Phys.* 127 (1996), pp. 179–185.

[133] Jia Zhao. “Mathematical sspects of modeling complex fluids: a note towards modeling sucess”. In: *Unpublished notes* (2015).

[134] Jia Zhao and Qi Wang. “3D hydrodyamic model of animal cytokinesis induced by contractile ring”. In: *submitted* (2015).

[135] Jia Zhao and Qi Wang. “A 3D hydrodynamic model for cytokinesis of eukaryotic cells”. In: *accepted by Communications in Computational Physics* (2015).

[136] Jia Zhao and Qi Wang. “A three dimensional hydrodynamic model for biofilm formation and function coupled with quorum sensing”. In: *submitted* (2014).

[137] Jia Zhao and Qi Wang. “A three dimensional hydrodynamic model of heterogeneous biofimls for antimicrobial persistence”. In: *submitted* (2014).

[138] Jia Zhao and Qi Wang. “A three dimensional viscoelastic hydrodynamic model for cell rounding”. In: *in preparation* (2015).

[139] Jia Zhao and Qi Wang. “decoupled energy stable schemes for vesicle hydrodynamic models”. In: *to be submitted* (2015).

[140] Jia Zhao and Qi Wang. “On energy stable schemes for a Q tensor hydrodynamic model of liquid crystals”. In: *to be submitted* (2015).

[141] Jia Zhao, Xiaofeng Yang, and Qi Wang. “Energy stable numerical schemes for a hydrodynamic model of nematic liquid crystals”. In: *submitted* (2015).

[142] Jia Zhao et al. “A 3D numerical study of antimicrobial persistence in heterogeneous multi-species biofilms”. In: *submitted* (2015).

[143] Jia Zhao et al. “A decoupled energy stable scheme for a hydrodynamic phase field model of mixtures of nematic liquid crystals and viscous fluids”. In: *submitted* (2015).

[144] Jia Zhao et al. “Modeling the excess cell membrane stored in a complex morphology of bleb-like protrusions”. In: *to be submitted* (2015).

[145] Chunfeng Zhou, Pengtao Yue, and James J. Feng. “Dynamic simulation of droplet interaction and self-assembly in a nematic liquid crystal”. In: *Langmuir* 24 (2008), pp. 3099–3110.

[146] Chunfeng Zhou, Pengtao Yue, and James J. Feng. “The rise of Newtonian drops in a nematic liquid crystal”. In: *Journal of Fluid Mechanics* 593 (2007), pp. 385–404.